Metal-Metal Bonding in Poly-Metallic Systems

Mohammed AL-Nafee

Linacre College

University of Oxford

A thesis submitted for the degree of

Doctor of Philosophy

July 2019

To my wife, Amal.

Acknowledgements

I would like to express my sincere gratitude to my supervisor, Professor John McGrady, for giving me the opportunity to be a part of his research group over past four years and for guiding me through all those years with numerous of help and supports.

A special thanks to Dr. Vaida Arcisauskaite for her generous help and advice during my first two years.

I would like to acknowledge our collaborators, Professor Graham Heath, Dr. Aliosn Edwards, and Dr. Nicholas Perkins for providing us with the experimental data.

I would like to thank the past and present members of the McGrady group, the Paton group, and the Duarte group. The groups have always been helpful and great to work with.

I would like to thank the Higher Committiee For Education Development in Iraq (HCED) for financial support.

Declaration of Authorship

I declare that the work presented in this thesis, Metal-Metal Bonding in Poly-Metallic Systems, is the original work of the author, except where references have been made to the published work of others. No part of the work in this thesis has previously been submitted for any other degree.

Mohammed AL-Nafee

Abstract

This thesis focuses on the nature of metal-metal bonding in poly-metallic systems. The electronic structures of examples of this class are studied using both density functional theory (DFT), time-dependent density functional theory (TD-DFT), periodic density functional theory and also the complete active space self-consistent-field (CASSCF) methodology. The thesis starts with a broad introduction to the chemistry of metal-metal bonded systems in chapter 1, where the focus is on the historical development of our understanding of the metal-metal bond from both experimental and theoretical perspectives. Potential applications of metal-metal bonded species are also covered. In chapter 2, a brief introduction of theoretical techniques used in this thesis is presented, covering Hartree-Fock theory, multi-configurational approaches and density functional theory, along with a discussion of basis sets. The first of the main results chapters, chapter 3, covers the electronic structure of face-shared trimetallic systems, $[(PEt_3)_3Ru(MCl_6)Ru(PEt_3)_3]^{z+}$, where M= Ru, Rh and Ir. Our aim here is to provide a framework for interpreting the available structural and spectroscopic evidence, and use this insight to establish how metal-metal interactions change as a function of the identity of the metal ions and also their oxidation states. Our results suggest that the switch from Ru to Rh/Ir in the central position induces a marked shift from a delocalized regime to one where unpaired electrons on the outer Ru centers only interact weakly via super exchange. The nature of the metal-metal bonding

of face-shared tetra-metallic systems, $[(PEt_3)_3Ru(Ru_2Cl_9)Ru(PEt_3)_3]^{1+}$, is the subject of chapter 4. Here we make the comparison with 'naked' $[Ru_2Cl_9]^{3-}$, and show that whilst reduction processes are localized on the Ru_2Cl_9 core, oxidation takes place at the external Ru centres, leading to metal-metal bonding that extends across the entire Ru_4 chain. In Chapter 5, the electronic structure of $(Cp^*RuCl)_2(\mu{-}Cl)_2$ system is discussed. This system is unique in so much as two molecules with very different Ru-Ru bond lengths co-exist in the solid-state. We have used periodic density functional theory to confirm that the crystallographic state is indeed the lowest energy one, but that relatively minor perturbations to the environment can drive transition to states where both Ru-Ru bonds are either long or short.

Contents

1 General Introduction: Metal-Metal Bonding in Transition Metal Systems **1**

1.1 Introduction 1

1.2 Metal-Metal bonding: Theoretical Approaches 13

1.3 Metal-Metal Bonding in Catalysis 19

1.4 This Thesis 22

1.5 Concluding Remarks 26

2 Elements of Theory: Configuration Interaction, Density Functional Theory, and Plane-Wave Method **27**

2.1 Fundamental Concepts of Quantum Chemistry 27

2.2 Hartree-Fock Theory 30

2.3 Electron Correlation and Post-HF Methods 35

2.4 Density Functional Theory 39

2.4.1 The Hohenberg-Kohn Theorems 40

2.4.2 The Kohn-Sham (KS) Method 41

2.4.3 The Exchange-Correlation Functionals 44

2.5 Basis Sets 48

2.6 Quantum Chemistry in Periodic Systems 50

3 Metal-Metal Bonding in Face-Shared Trinuclear Metal Chains: The Effect of the Identity of the Central Metal Ion and Oxidation State 55

3.1 Introduction 55

3.2 Computational Methodologies 59

3.3 Results and Discussion 60

3.3.1 Electronic Structure: the DFT Picture 64

3.3.2 Multi-Configurational SCF (CASSCF) Approach to the Electronic Structure 79

3.4 Conclusion 83

4 Metal-Metal Bonding in Face-Shared Tetranuclear Metal Chains: The Effect of the Oxidation States 84

4.1 Introduction 84

4.2 Computational Methodologies 87

4.3 Results and Discussion 88

4.3.1 The Electronic Structure at DFT Level 91

4.3.2 Multi-Configurational SCF (CASSCF) Approach to the Electronic Structure 103

4.4 Conclusion 108

5 Metal-Metal Bonding in $(Cp^*RuCl)_2(\mu-Cl)_2$: A Case of Bond-Stretch Isomerism? 110

5.1 Introduction 110

5.2 Computational Methodologies 113

5.3 Results and Discussion 114

5.3.1 The Electronic Structure at the Molecular DFT Level 114

5.3.2 Multi-Configurational SCF (CASSCF) Approach to the Electronic Structure 116

5.3.3 Solid-State Electronic Structure: the Plane-Wave Approach . . 119
5.4 Conclusion 124

References **126**

List of Figures

1.1 Structure of (a) the triangular anion in $Cs_3Re_3Cl_{12}$, (b) Re_3I_9 showing that one of Re atoms is coordinatively unsaturated, and (c) the $[Re_2Cl_8]^{2-}$ anion. 2

1.2 Schematic molecular orbital arrays for D_{4h} molecules such as $[Re_2Cl_8]^{2-}$. 4

1.3 Photoelectron spectrum of $[Re_2Cl_8]^{2-}$. Adapted with permission from reference[24]. Copyright ©2000, American Chemical Society. 6

1.4 Structure of chromium molecules with quintuple bond, (a) Ar′CrCrAr′, (b) (μ-η^2-$^{H}L^{iPr}$)$_2$Cr$_2$, and (c) $Cr_2(Ar^{Xyl}NC(H)NAr^{Xyl})_3$. 9

1.5 Possible of complexes with quintuple bond with corresponding molecular orbital diagrams, on left type I and II and on right type III molecules. 10

1.6 Schematic representation of molecular orbital arrays of the trinuclear metal string complexes. 12

1.7 General classification of metal-metal bonds in catalysis. 20

1.8 The electronic structure of the high electrophilic carbene intermediate. 21

1.9 Molecular orbital arrays of face-shared octahedral molecules such as $[Ru_2Cl_9]^{3-}$. 23

2.1 Schematic representation of CASSCF wavefunction. 38

2.2 Comparison between STO and GTO. 49

2.3 Schematic drawing of a 3s-derived Bloch function of a one-dimensional crystal of sodium atoms. 53

3.1 The structure of tri-metallic system, $[Ru_3Cl_{12}]$ (a) system along with $[Ru_3Cl_6(p-cymene)_2]$ (b) and $(PEt_3)_3Ru[MX_6]Ru(PEt_3)_3$ (c) systems of our interest, where M = Ru (1), Rh (2), and Ir (3). Hydrogen atoms was omitted for clarity. 56

3.2 Molecular orbital array for $[Cl_3Ru(RuCl_6)RuCl_3]^{4-}$ (D_{3d} symmetry). . 57

3.3 Optimized geometry (BLYP), Kohn-Sham orbital manifold and UV-Vis spectra of $[RuCl_6]^{3-}$ (left) and 1^+ (right). The energy scale corresponds to the orbitals of 1^+. The experimental spectrum is shown in blue and the TD-DFT-M06-L in dashed red. 66

3.4 Optimized geometry (BLYP), Kohn-Sham orbital manifold and UV-Vis spectra of $[IrCl_6]^{2-}$ (left) and 3^{2+} (right). The energy scale corresponds to the orbitals of 3^{2+}. The experimental spectrum is shown in blue and the TD-DFT-M06-L in dashed red. 69

3.5 Magic pentagon diagram. 71

3.6 Optimized geometry (BLYP), Kohn-Sham orbital manifold and UV-Vis spectra of $[IrCl_6]^{3-}$ (left) and 3^+ (right). The energy scale corresponds to the orbitals of 3^+. The experimental spectrum is shown in blue and the TD-DFT-M06-L in dashed red. 73

3.7 Optimized geometry (BLYP), Kohn-Sham orbital manifold and UV-Vis spectra of $[RuCl_6]^{2-}$ (left) and 1^{2+} (right). The energy scale corresponds to the orbitals of 1^{2+}. The experimental spectrum is shown in blue and the TD-DFT-M06-L in dashed red. 75

3.8 Optimized geometry (B3LYP), Kohn-Sham orbital manifold and UV-Vis spectra of $[Ru_2Cl_3(PH_3)_6]^{3-}$ (left) and 3^{3+} (right). The energy scale corresponds to the orbitals of 3^{3+}. The experimental spectrum is shown in blue and the TD-DFT-M06-L in dashed red. 78

3.9 The manifold of configurations for the 1^{2+}, 2^{3+} and 3^{3+} (16-electron) systems. 80
3.10 Active space natural orbitals of 1^{2+} and 2^{3+} complexes. 81

4.1 The structure of di-metallic, $[Ru_2Cl_9]^{3-}$ (a) along with 4^+. Hydrogen atoms were omitted for clarity. 84
4.2 Molecular orbital array for $[(PEt_3)_3Ru[Ru_2Cl_9]Ru(PEt_3)_3]^+$ (D_{3h} symmetry). 86
4.3 Optimized geometry (BLYP), Kohn-Sham orbital manifold and UV-Vis spectra of $[Ru_2Cl_9]^{3-}$ (left) and 4^+ (right). The energy scale corresponds to the orbitals of 4^+. The experimental spectrum is shown in blue, the TD-DFT-M06-L in dashed red and TD-DFT-B3LYP in solid red. 92
4.4 Optimized geometry (BLYP), Kohn-Sham orbital manifold and UV-Vis spectra of $[Ru_2Cl_9]^{4-}$ (left) and 4^0 (right). The energy scale corresponds to the orbitals of 4^0. The experimental spectrum is shown in blue, the TD-DFT-M06-L in dashed red. 95
4.5 Optimized geometry (B3LYP), Kohn-Sham orbital manifold and UV-Vis spectra of $[Ru_2Cl_9]^{2-}$ (left) and 4^{2+} (right). The energy scale corresponds to the orbitals of 4^{2+}. The experimental spectrum is shown in blue, the $^4A_1''$-TD-DFT in dashed red, the unsymmetrical-$^2E_1'$-TD-DFT in solid red and $^2E_1'$-TD-DFT black. 99
4.6 Optimized geometry (B3LYP), Kohn-Sham orbital manifold and UV-Vis spectra of $[Ru_2Cl_9]^-$ (left) and 4^{3+} (right). The energy scale corresponds to the orbitals of 4^{3+}. The experimental spectrum is shown in blue, the $^1A_1'$-TD-DFT in dashed red, the $^5A_1''$-TD-DFT in solid red and BS-$^1A_1'$-TD-DFT black. 102
4.7 The manifold of configurations for the 4^+ (22-electron) system. 104

4.8 Active space natural orbitals of 4^{+} molecule with it is occupations of $^{1}A_{1}'$ ground state. 105
4.9 Active space natural orbitals of 4^{2+} molecule with it is occupations of $^{4}A_{1}''$ ground state. 107
4.10 Active space natural orbitals of 4^{3+} molecule with it is occupations of the closed-shell $^{1}A_{1}'$ state on both $^{1}A_{1}'$ and $^{5}A_{1}''$ geometries. The occupations of quintet geometry between the parenthesis. 108

5.1 X-ray structure of $(Cp^{*}RuCl)_{2}(\mu{-}Cl)_{2}$ system taken from reference 247-249. 111
5.2 Kohn-Sham molecular orbital of molecule A (left) and molecule B (right) computed by BLYP functional. 115
5.3 Potential energy surface at three different configurations optimized by BLYP (left) and B3LYP (right) functionals. 116
5.4 Active space orbitals of molecule A (averaged over the nine lowest singlets) and the orbital occupations in the lowest singlet state. . . . 117
5.5 Active space orbitals of molecule B (averaged over the nine lowest singlets) and the orbital occupations in the lowest singlet state. . . . 118
5.6 Potential energy surface at CASPT2 level. 120
5.7 DOS of molecule A (left) and B (right), projected onto the Ru 4d orbitals, for the ferromagnetic configuration. 122

Chapter 1

General Introduction: Metal-Metal Bonding in Transition Metal Systems

1.1 Introduction

The history of molecular multiple bonds began as long ago as 1844 when Peligor reported for the first time a bright blue aqueous solution of chromium (II) ions. There is little doubt that this compound was $Cr_2(O_2CCH_3)_4(H_2O)_2$, although the empirical formula was reported as $CrC_4H_4O_5$ due to the uncertainties in the atomic weight of hydrogen prevalent at the time.[1,2] The full significance of this molecule only became apparent over 100 years later, in 1962-1963, when Cotton studied the structure of $CsReCl_4$. This compound had been reported in literature as a low-spin tetrahedral species, a plausible suggestion given that large ligand-field splittings in a heavy third-row transition metal atom which would favour a closed-shell e^4t^0 configuration, consistent with the observed diamagnetic properties.[3] At that time, before the advent of modern computers, establishing the structure of a molecule was a great challenge because the intensity data were collected on photographic film rather than on electronic area detectors used nowadays. Nevertheless, Cotton and co-workers were able to establish that, in fact, the structure of $CsReCl_4$ does not contain tetrahedral $[ReCl_4]^-$ fragments, but instead three rhenium atoms in close

proximity with bond lengths of 2.50 Å.[4,5] The structure has three rhenium atoms in a triangular arrangement, each rhenium atom bonded to three terminal chlorine atoms. In addition, the rhenium atoms are bridged by one chlorine as shown in Figure 1.1. The Re-Re distance was found to be 0.26 Å shorter than that in rhenium metal (2.76 Å), an unprecedented result that suggests the presence of metal-metal double bonds. The triangular arrangement of the three rhenium atoms was also found in the neutral compound $Re_3Cl_9(PEt_2Ph)_3$[6] and in $ReBr_3$,[7,8] and also the iodide analogue ReI_3 has also been synthesized but the structure is quite different from the chloride and bromide analogues, in so much as it has one unsaturated rhenium atom as shown in Figure 1.1. This leads to different Re-Re bond lengths, two long (Re-Re = 2.507 Å) associated with the seven-coordinate rhenium atoms, and one short (Re-Re = 2.44 Å) corresponding to to the six-coordinate rhenium atom.[9]

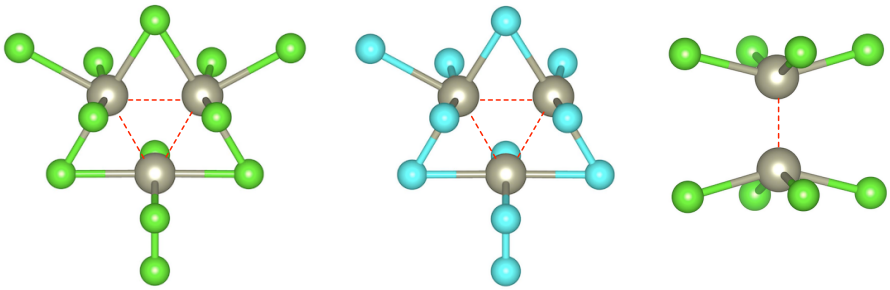

Figure 1.1: Structure of (a) the triangular anion in $Cs_3Re_3Cl_{12}$, (b) Re_3I_9 showing that one of Re atoms is coordinatively unsaturated, and (c) the $[Re_2Cl_8]^{2-}$ anion.

In 1964, Cotton and co-workers also reported the synthesis and characterization of the landmark $[Re_2Cl_8]^{2-}$ molecule (Figure 1.1), featuring a metal-metal quadruple bond and a metal-metal distance of only 2.27 Å.[10] The structure of this molecule has being described as two rhenium atoms lying within a square prism defined by eight chlorine atoms. The chlorine atoms have an eclipsed arrangement rather than staggered, suggesting that there must be strong bonds that overcome the large steric repulsions between chloride ions. To a good approximation, the s, p_x, p_y, $d_{x^2-y^2}$

orbitals on each rhenium atom are used to form the four Re-Cl bonds, leaving the remaining metal-based orbitals to form the metal-metal bonds. The d_{z^2} orbitals on each rhenium atoms overlap to form σ bond, while d_{xz} and d_{yz} form two fairly strong π bonds. These three bonding molecular orbitals are populated by six of eight rhenium d orbitals. The remaining Re d orbital, d_{xy}, overlaps to form δ bonding and antibonding orbitals in the eclipsed arrangement. This conformation therefore immediately explains the diamagnetic properties of the $[Re_2Cl_8]^{2-}$ molecule, and the formal bond order of 4.0 (the bond order is defined as number of electrons in bonding orbitals minus the electrons in antibonding orbitals divided by 2) is consistent with the very short bond. This electronic structure description is represented schematically in the molecular orbital array shown in Figure 1.2. In the staggered configuration, the δ bond would be completely lost due to the zero d_{xy}-d_{xy} overlap and so the adoption of the eclipsed structure indicates that the δ bond overcomes the increased Cl-Cl repulsions which can be estimated to be only a few kilocalories per mole. The structure of $Re_2Cl_6P_2$ was also reported as eclipsed with quadruple metal-metal bonds,[11,12] and other transition metals were subsequently shown to form closely-related compounds. For example, a technetium halide complex, $(NH_4)_3Tc_2Cl_8$, reported by Mellish and coworkers in 1963[13] was subsequently shown by Cotton and Bratton[14] to have an anion isostructural with $[Re_2Cl_8]^{2-}$. Importantly, the 3- charge on the anion in $(NH_4)_3Tc_2Cl_8$ is consistent with the observed paramagnetism. In 1965, the structure of dimolybdenum tetraacetate was reported in which the two Mo atoms are bonded with a separation of only 2.11 Å.[15] This extremely short metal-metal bond indicted that the quadruple bonds between d^4 ions of the second- and third-row transition metals are quite general, and since then an enormous amount of time and effort has been expended to determine the validity of the molecular orbitals diagram in Figure 1.2 and also the ordering of these orbitals in other bimetallic systems having real or idealized D_{4h} symmetry. There are now many molecules with similar bimetallic structures, in-

cluding metals of the second- and third-row transition metal series, with bond orders ranging from 0.5 to 4.0, and they have been characterized using a range of physical techniques including crystallographic but also a variety spectroscopic techniques, electrochemistry, magnetic susceptibility, as well as the theoretical studies that will be applied in this thesis.[16]

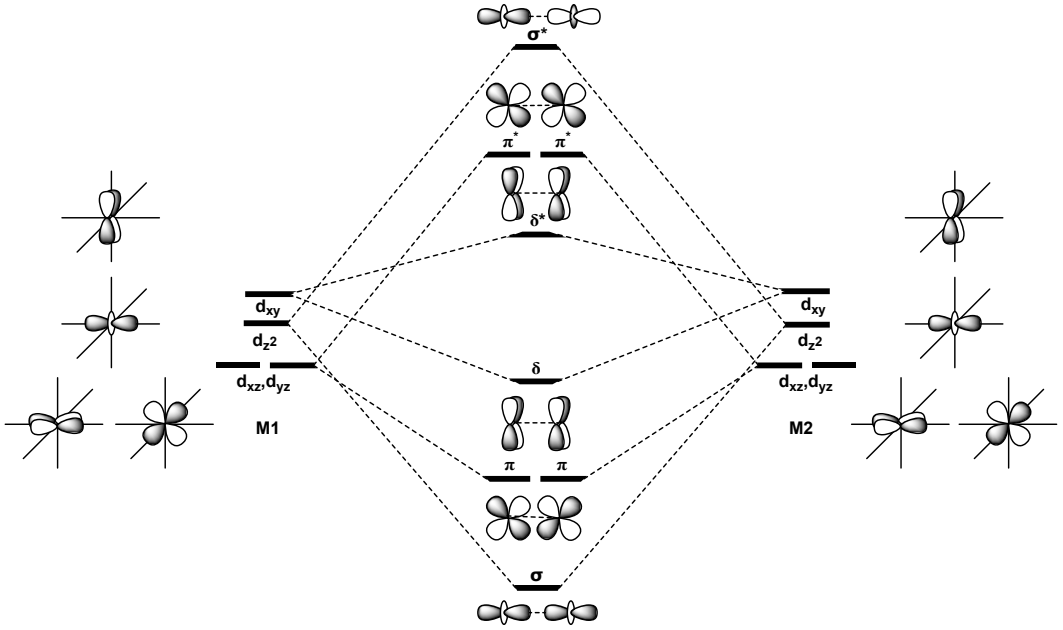

Figure 1.2: Schematic molecular orbital arrays for D_{4h} molecules such as $[Re_2Cl_8]^{2-}$.

Bimetallic Systems: the δ Bond and the Validation of MO Diagram

As anticipated above, only the eclipsed conformation of $[Re_2Cl_8]^{2-}$ supports the formation of the δ bond because the alternative staggered isomer leads to zero overlap between the two d_{xy} orbitals on each rhenium center.[17] The rotation about the metal-metal bond varies 0 (eclipsed) to 45° (staggered) therefore corresponds to a formal decrease in bond order from 4 to 3, and we might, therefore, anticipate that increasing rotation angles should be reflected in a lengthening of the metal-metal distance. The relationship between metal-metal bond length and bond order is, however, not straightforward to establish because it depends on many other factors including the charge on the metals and the multiconfigurational nature of the metal-metal bond, as

has been described in detail elsewhere.[16] The relationship between torsion angle and bond length was tested by designing a series of dimolybdenum systems with halide and phosphine ligands, $Mo_2X_4(P)_n$ where X is Cl, Br and n = 4 if the ligand is a mono-phosphine or 2 if it is a di-phosphine. Cotton and co-workers[18] have carefully analysed the structure of ten such compounds, tracing the metal-metal bond length as a function twist angle about the Mo-Mo bond. Nine of these compounds have the $Mo_2X_4(PP)_2$ (X = Cl, Br) formula while the other is a closely-related $Mo_2Br_4(AsP)_2$ system, the (PP) and (AsP) represent bridging di-phosphine and arsino-phosphine ligands. They found a Mo-Mo bond distance of 2.192 Å at a mean torsion angle of 45° (zero δ overlap) in contrast to a rather shorter value of 2.138(1) Å at a mean twist angle of 0°.[19] The results of this analysis were further refined using eleven additional complexes with relatively minor steric and electronic differences among the bridging ligands,[20] from which it was established that the Mo-Mo distance changes from 2.128 Å to 2.225 Å across a range of torsion angles from 0° to 45°.

Photoelectron spectroscopy (PES) provides the most direct information about valence electrons in molecules. In summary, a photon with energy ($h\nu$) greater than or equal to the binding energy of the electron will cause that electron to be ejected. The kinetic energy ($E_k(e^-)$) of the ejected electron can be measured and the ionization energy (IE) is given by IE = $h\nu$ - $E_k(e^-)$. Early work in this field was done mainly by Hillier and Lichtenberger, who examined a number of quadruple-bonded systems such as $[M_2X_8]^{4-}$, $M_2(carboxylate)_4$, $M_2(formamidinate)_4$, and $M_2(methylhydroxpyridinate)_4$, M = Cr, Mo, and W.[21–23] A particularly significant experiment was performed on the $[Re_2Cl_8]^{2-}$ molecule,[24] the photoelectron spectrum of which is shown in Figure 1.3. The spectrum shows a clear separation between the molecular orbitals that mediate the metal-metal bonds and those involved in metal-ligand bonding. The δ, π, and σ metal-metal bonding orbitals have low binding energies and give rise to three well-resolved bands below 3 eV. The metal-ligand

bonding orbitals give rise to peaks at higher binding energies. This experimental spectrum therefore provides a direct link between experiment and the proposed molecular orbital diagram of $[Re_2Cl_8]^{2-}$ in Figure 1.2.

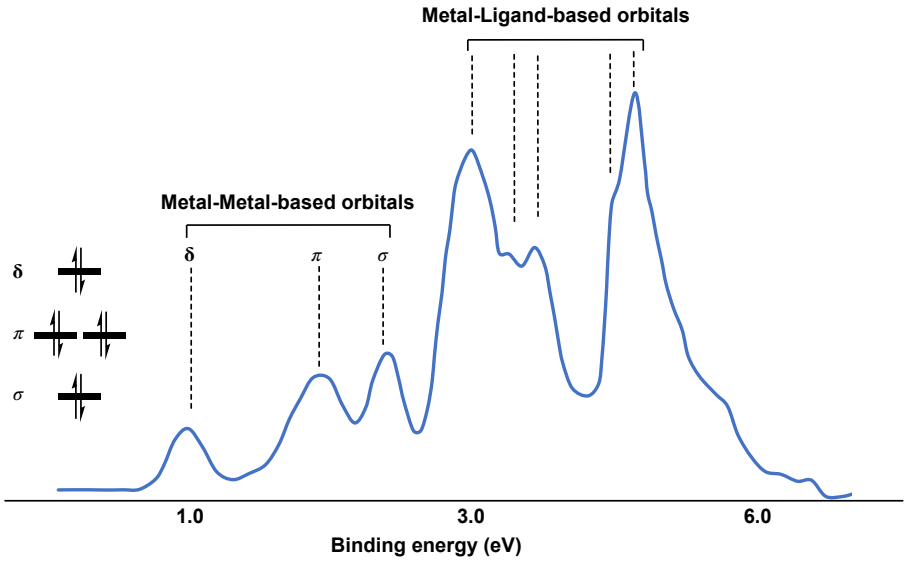

Figure 1.3: Photoelectron spectrum of $[Re_2Cl_8]^{2-}$. Adapted with permission from reference[24]. Copyright ©2000, American Chemical Society.

The relative weakness of the δ bond means that fractional bond orders, where the bonding or antibonding components are partially filled, are relatively common. For example, $(NH_4)_3Tc_2Cl_8$[13] and $Re_2Cl_5(CH_3SC_2H_4SCH_3)_2$, reported in 1968,[25] have a $[M_2]^{5+}$ core with a $\sigma^2\pi^4\delta^2\delta^{*1}$ configuration and formal bond order of 3.5. Similarly $[Mo_2(TiBP)_4]^+$, with a $[Mo_2]^{5+}$ core, has a $\sigma^2\pi^4\delta^1$ configuration and also a bond order of 3.5.[26] In fact, the series of rhenium complexes $Re_2Cl_4(dppm)_2$, $Re_2Cl_5(dppm)_2$, and $Re_2Cl_6(dppm)_2$, where dppm is 1,1-bis(diphenylphosphino)-methane, constitute a continuous series with bond orders between 3.0 to 3.5 to 4.0:[27,28] the paramagnetic compound $Re_2Cl_5(dppm)_2$ ($[Re_2]^{5+}$) is the direct analogue of $Re_2Cl_5(CH_3SC_2H_4SCH_3)_2$, with a $\sigma^2\pi^4\delta^2\delta^{*1}$ configuration. A range of guanidinate compounds having $[Re_2]^{7+}$ and $[Re_2]^{8+}$ cores also support bond orders of 3.5 and 3.0, respectively,[29–32] and formal bond orders of 3.5 are known for $[Cr_2]^{5+}$, $[Re_2]^{7+}$ and $[Tc_2]^{5+}$ cores ($\sigma^2\pi^4\delta^1$)[33–35] and $[Os_2]^{7+}$ ($\sigma^2\pi^4\delta^2\delta^{*1}$). More electron-rich compounds have lower fractional bond orders,

including the 15-electron $[Pt_2]^{5+}$ and $[Pd_2]^{5+}$ cores (bond order = 0.5),[36] 13-electron $[Ir_2]^{5+}$ and $[Rh_2]^{5+}$ (bond order = 1.5),[37,38] and 11-electron $[Re_2]^{5+}$ (bond order = 2.5).[39]

All of the above configurations could be anticipated based on addition or removal of electrons from the molecular diagram in Figure 1.2. However, the differences in energies of the s, p and d components are very small, and the order can be changed by subtle modification to the ligands. For example, 11-electron $[Ru_2]^{5+}$ cores might be expected to have a doublet $\sigma^2\pi^4\delta^2\delta^{*2}\pi^{*1}$ electronic configuration and a formal bond order of 2.5. However in many cases, the ground state proves to be a quartet with three unpaired electrons, $\sigma^2\pi^4\delta^2\pi^{*2}\delta^{*1}$, one in each of the antibonding orbitals.[40] These differences result from a small energy difference or near-degeneracy between the δ^* and π^* orbitals which can sometimes even go as far as an inversion of ordering. The influence of zero-field splitting often makes it difficult to establish the precise configuration using EPR spectroscopy,[41] and as a result the electronic configuration of $[Ru_2]^{5+}$ species has historically been referred to as $\sigma^2\pi^4\delta^2(\delta^*\pi^*)^3$ where the bracket implies that the three electrons in the frontier orbitals are distributed in some unspecified fashion between the δ^* and π^* orbitals.

Metal-Metal bonding: Beyond the Quadruple Bond

Since the recognition of the first quadruple bond in $[Re_2Cl_8]^{2-}$, a huge number of complexes with quadruple bond has been synthesized and characterized. However, the interest in molecules with chemical bond order higher than four has remained, and indeed sextuple bonds have been proposed, albeit in gas-phase naked dimers of Cr, Mo, and W. Unfortunately, these species cannot be isolated and structurally characterized, but the molecular orbital diagram of such species features two σ, a doubly degenerate π, and a double degenerate δ orbital.[42–46] As far back as 1979, Hoffman and co-workers proposed that molecules with the M_2L_6 structure and an eclipsed D_{3h} symmetry could possibly support a metal-metal quintuple bond.[47] To achieve such

a situation, a few design principles must be considered. Each metal ion must have a d^5 high spin electronic configuration, and therefore a relatively small ligand field. The choice of ligands is therefore crucial in the formation of stable quintuply bonded species. The number of ligands also must be reduced to a minimum to reduce the participation of metal d orbitals in formation the metal-ligand σ-bond. A final point is that π-donor and -acceptor ligands should be avoided because metal-ligand π-bonding decreases the overlap between the two metal centers.[48] These conditions effectively limit the search to group six of the periodic table (Cr, Mo, and W), which are well-known for their strong metal-metal formation with highest (Mo and W) and second highest (Cr) melting point. Indeed this group has been the source of the majority of known metal-metal triply and quadruply bonded species.[16] In 2001, Weinhold and Landis suggested that the most plausible dinuclear geometry with a quintuple bond should be a trans-bent structure with C_{2h} symmetry,[49] and, in 2005, Power and co-workers isolated the Ar′CrCrAr′ molecule, where Ar′ is 2,6-(2,6-i$Pr_2C_6H_3$)C_6H_3.[50] The structure of Ar′CrCrAr′ molecule is shown in Figure 1.4: the two chromium centers and two *ipso* carbon atoms of the flanking phenyl rings are co-planar and do indeed adopt a *trans*-bent confirmation with a C_{2h} local symmetry. The Cr-Cr bond length of 1.8351(4) Å is consistent with a quintuple Cr-Cr bond. The bulky ligand may, of course, play a role in imposing a short Cr-Cr distance, so Power and co-workers synthesized Ar′CrCrAr′ molecules with different substituents on the central phenyl ring (Figure 1.4), $SiMe_3$, OMe, or F. The metal-metal bond length of these three analogues are 1.8077(7) Å, 1.8160(5) Å, and 1.831(2) Å for $SiMe_3$, OMe, or F, respectively.[51,52] The small changes in the metal-metal bond length in these molecule are within the window usually ascribed to crystal-packing, which implies that the short metal-metal bond in Ar′CrCrAr′ is due to bonding interactions between two chromium centers rather than the steric effects of the ligands. The weak temperature independent paramagnetism of Ar′CrCrAr′ is consistent with strongly coupling between the d^5

electronic configurations of the two metal centers. This hypothesis is supported by DFT calculations which showed that the natural bond order of Ar′CrCrAr′ is 3.43.[50]

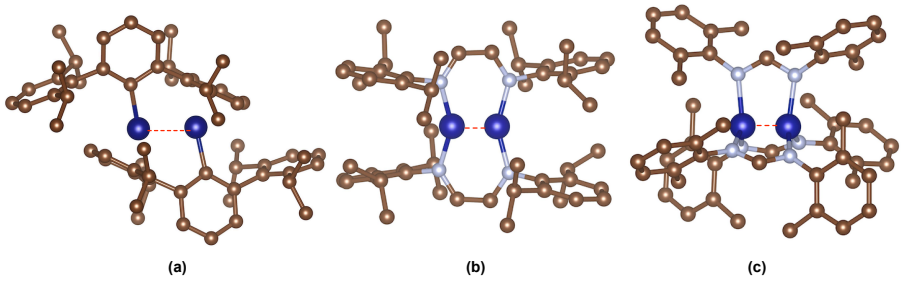

Figure 1.4: Structure of chromium molecules with quintuple bond, (a) Ar′CrCrAr′, (b) (μ-η^2-$^{H}L^{iPr}$)$_2$Cr$_2$, and (c) Cr$_2$(Ar^{Xyl}NC(H)NAr^{Xyl})$_3$.

Power's landmark achievement has encouraged scientists to develop the chemistry of the quintuple bond, and several molecules with quintuple bond of group six have since been characterized. All feature bulky ligands and very short metal-metal bond distance.[53–62] Based on structure characterization and theoretical calculations three possible geometries of quintuple bonded species were proposed as shown in Figure 1.5, type I, type II, and type III. The type II geometry is the most common, while there are just three known compounds with the type III paddlewheel structure.[62–64]

The chemistry of the Cr-Cr molecules is not limited to the use of the bulky terphenyl ligands, and two derivatives of the diimine framework have been important in the developments by Kreisel and co-workers.[53] The two chromium centers of the (μ-η^2-$^{H}L^{iPr}$)$_2$Cr$_2$ molecule are bonded to two nitrogen atoms of the ligand as shown in Figure 1.4(b), where $^{H}L^{iPr}$ is N,N'-bis(2,6-diisopropylphenyl)-1,4-diazadiene. The geometry about each metal centre is trigonal planar, with each chromium center coordinated to two nitrogen atoms of the bridging diazadienes ligands and also to the other chromium center. This complex also has a very short metal-metal bond (1.8028(9) Å), shorter than that in Ar′CrCrAr′ molecule by about 0.03 Å. Furthermore, this molecule has an almost planar arrangement around the chromium centers due to the nature of the N$_2$CrCrN$_2$ core. Noor and co-workers reported a similar

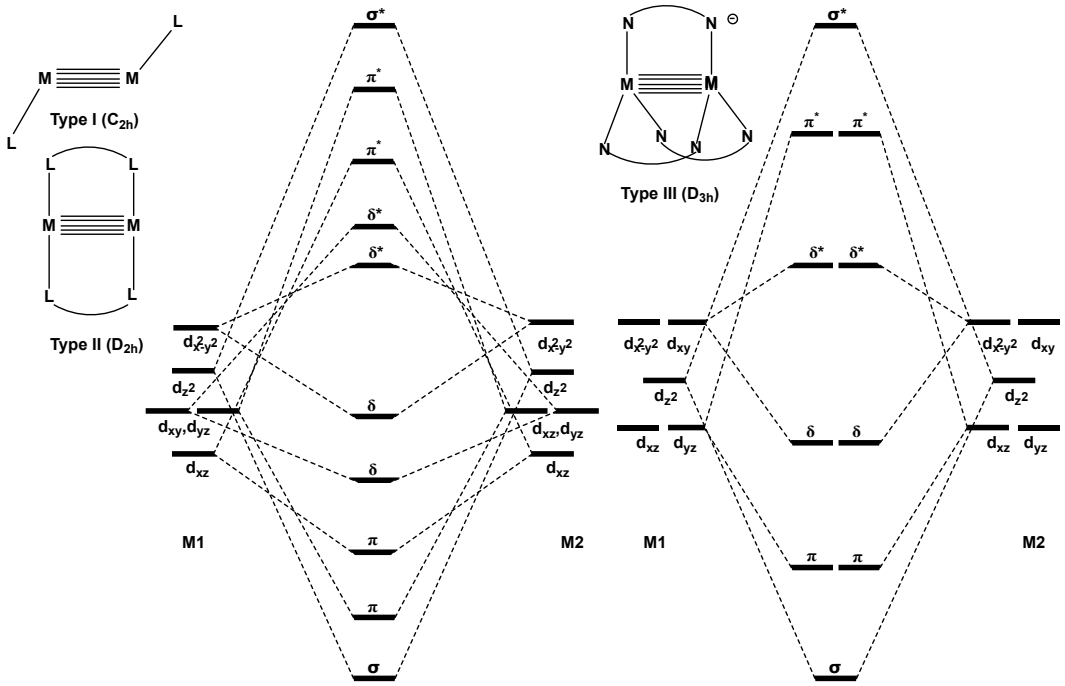

Figure 1.5: Possible of complexes with quintuple bond with corresponding molecular orbital diagrams, on left type I and II and on right type III molecules.

complex with an even shorter Cr-Cr distance of 1.749(2) Å.[56] The quintuple Cr-Cr bond is not restricted to planar or almost planar geometries, as in the previous two cases. Tsai and co-workers[63] have synthesized a molecule containing three diimine ligands forming a cage that hosted the Cr-Cr bond as shown in Figure 1.4(c), where the Cr-Cr bond length is 1.8169(7) Å. This molecule is paramagnetic, but reduction gave a diamagnetic analogue with a Cr-Cr bond length of 1.7397(9) Å, the shortest metal-metal bond known to date.

Metal-Metal Bonding in Polynuclear Species

Extended metal atom chains (EMACS) were first reported in 1968 when the trinuclear nickel complex, $Ni_3(dpa)_4Cl_2$ ($dpa^- =$ dipyridylamido) was synthesized by Robinson and Hurley.[65] However, the structure of this molecule remained unknown until 1991 when Hathaway and co-workers showed that it is based on a linear chain of three metal atoms surrounded by a quadruple helix of ligands.[66–68] The nickel complex and

its copper analogue inspired Peng and co-workers to explore a wide range of trinuclear transition metal complexes with the formula of $M_3(dpa)_4Cl_2$ with many different metal centers.[69–72] The dpa^- ligand of all these complexes has amido and pyridyl groups which can efficiently stabilize the linear metal chains. Therefore, by increasing the length of the supporting ligands, one can synthesise oligonuclear complexes with long linear metal chains. Pentanuclear $[M_5(tpda)_4Cl_2]$ with M of Ni, Co, Cr, and Ru,[73–78] heptanuclear $[M_7(teptra)_4Cl_2]$ with M of Ni and Cr,[79,80] and nonanuclear $[M_9(peptea)_4Cl_2]$ with M of Ni and Cr have now all been synthesised using this design principle.[81,82] A schematic molecular orbital array for a trinuclear metal complexes is shown in Figure 1.6, where the 12 molecular orbitals come from linear combinations of four orbitals on each metal center. The array features three orbitals with σ-symmetry (σ, σ^{nb}, and σ^*) resulting from overlap of the d_{z^2} orbitals, three double degenerate orbitals with π-symmetry (π, π^{nb}, and π^*) from the overlap between d_{xz} and d_{yz} and three with δ-symmetry (δ, δ^{nb}, and δ^*) from overlap between d_{xy}. We note here that the order of these orbitals might change in response to changes in the coordination of different type of axial ligands. Cotton and co-workers have shown, based on this picture, that the 24-electrons in the $Ni_3(dpa)_4Cl_2$ complex[83] fill all the bonding, non-bonding, and anti-bonding orbitals, giving a formal bond order of zero. 21-electron $Co_3(dpa)_4Cl_2$ in contrast, has an empty π orbital, giving formal bond order of one distributed over two Co-Co contacts.[84,85]

DFT calculations have been critical to the development of our understanding of the bonding in these multinuclear systems, initially by Bénard and co-workers who described the electronic configurations and magnetism of a number of trinuclear metal molecules.[86] The electronic structure of $Co_3(dpa)_4Cl_2$ has been reinvestigated by McGrady and co-workers who established the origin of spin-state polymorphism in this molecule.[85] The electronic structure of trinuclear complexes of second row transition metals such as $Ru_3(dpa)_4X_2$, X = Cl or CN, have also been investigated at the

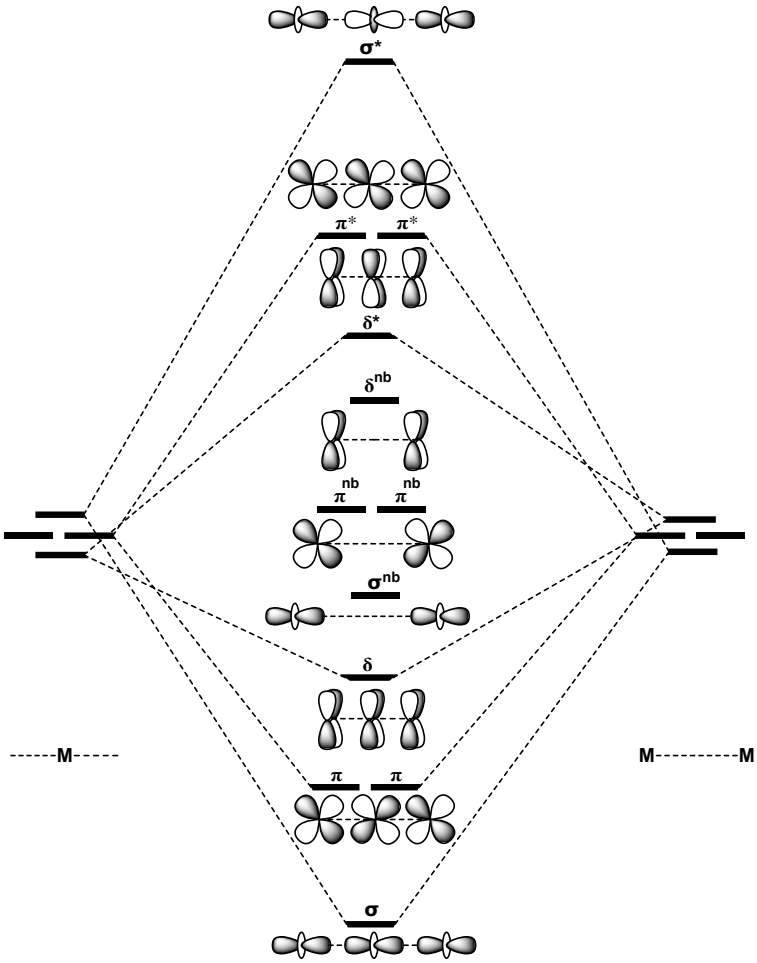

Figure 1.6: Schematic representation of molecular orbital arrays of the trinuclear metal string complexes.

DFT level.[87] These molecules show unusual metal-metal bonding that is dependent on the identity of the axial ligands. $Ru_3(dpa)_4Cl_2$, with a weak axial ligand has an $\sigma^2\pi^4\delta^2(\pi^{nb}\delta^{nb})^6\delta^{*2}\sigma^{nb2}$ electronic configuration that generates one metal-metal σ bond and two metal-metal π bonds. In contrast $Ru_3(dpa)_4CN_2$, with a strong field axial ligand, gives a $\sigma^2\pi^4\delta^2(\pi^{nb}\delta^{nb})^6\delta^{*1}\pi^{*3}$ electronic configuration with one metal-metal σ bond, half a π bond and half a δ bond. These results highlight the importance of the axial ligands in determinate the nature of the metal-metal bonding. Spectroscopy has also played an important role in establishing the nature of the bonding in these systems. For example, IR and surface-enhanced Raman spectroscopy.[88–90]

The nature of the metal-metal bonding in longer metal chains is more difficult

to establish, but it seems clear that the $[Cr_9(u_9{-}N_9{-}mpz)_4(NCS)_2]$ where N_9-mpz is N_2,N_6-bis-[6[(pyridine-2-ylamido)-pyridin-2-yl]pyrazine-2,6-diamido) has four localized metal-metal quadruple bonds with a single isolated Cr(II) centre.[82]

Heteronuclear metal string complexes are similarly challenging, but Peng, Berry and coworkers have reported several complexes which feature symmetric or asymmetric metal arrangements.[91–100] In addition to the symmetric heteronuclear metal complexes (M_a-M_b-M_a), there are unsymmetric types (M_a-M_a-M_b and M_a-M_b-M_c), for example, $[CrCrFe(dpa)_4Cl_2]$ and $[MoWCr(dpa)_4Cl_2]$.[95,97] The $[CoPdCo(dpa)_4Cl_2]$ system reported by Peng and co-workers shows strong antiferromagnetic coupling interactions between the three metal centers which contrasts dramatically to the spin-crossover behavior displayed by the all-cobalt complex.[91] The $[CuPdCu(dpa)_4Cl_2]$ and $[CuPtCu(dpa)_4Cl_2]$ molecules show much weaker superexchange interactions between the two terminal copper atoms. The replacement of the central diamagnetic Cu(III) of all-copper molecules by Pd(II) and Pt(II) leads to decrease the superexchange interactions between the terminal Cu(II) centers.

1.2 Metal-Metal bonding: Theoretical Approaches

The accurate treatment of multireference systems to capture the effects of electron correlation remains one of outstanding challenges in quantum chemistry. The details of the theoretical methods used in this thesis will be discussed in chapter 2, but here I present an overview of approaches to electronic structure that have been applied in the context of metal-metal bonded systems. Generally, multireference systems are those that cannot be accurately described by a single electronic configuration. The electronic correlation energy is defined as the difference between the exact energy and the Hartree-Fock energy using same basis set limit,[101] and the error arising from the use of a single Slater determinant is often called static or non-dynamical correlation.[102–104] Systems containing metal-metal bonds, particularly multiple bonds, are

very often multiconfigurational in nature, and an accurate description must therefore consider static electron correlation.

Kohn-Sham density functional theory (KS-DFT)[105] has emerged over the past two decades as the most popular method for dealing with large systems, particularly those that contain transition metals. However, this method is inherently single determinant in nature, and the accuracy of the available exchange-correlation functionals is open to debate.[106–108] The prediction of ground spin states is a case in point, with hybrid functionals tending to over-stabilize high-spin states, whereas generalized gradient approximation (GGA) functionals favor low-spin states.[109,110] An alternative approach is multiconfiguration self-consistent field (MCSCF) theory, which in practical terms means the complete active space self-consistent field (CASSCF) method which will be described in detail in chapter 2.[111] The static electron correlation can be accurately accounted for with these methods, and dynamic correlation can then be added by using multireference perturbation theory within the complete active space second-order perturbation theory (CASPT2) approach.[112] The main challenge in using the CASSCF methodology is the choice of the active space because the number of the Slater determinants increases rapidly with number of the active orbitals. As a result calculations with CAS(16,16), which indicates 16 electrons in 16 orbitals, represent the current limit of feasibility, and this imposes limitations on the chemical problems that can be addressed with this methods. However, this limitation can be overcome by introducing some constraints on the active space, for example, using restricted active space (RASSCF)[113] or generalized active space (GASSCF) protocols.[114] In studies of metal-metal bonding, the proper active space should include the metal-metal bonding and anti-bonding orbitals and, ideally, the necessary metal-ligand orbitals. Within the CASSCF methodology the effective bond order is defined as the sum of the occupation numbers of the bonding orbitals minus the sum of the occupation number of anti-bonding orbitals divided by two.[115,116] Unlike the single

determinant methods where the occupation numbers are restricted to integer values, the occupation numbers from a CASSCF wavefunction can be fractions between zero and two. In this sense, the occupation numbers can capture all points between the strongly bonded limit and the dissociation limit, where occupation numbers of the bonding and antibonding orbitals are 0.5.

Metal-Metal Bonding in $[Re_2Cl_8]^{2-}$

$[Re_2Cl_8]^{2-}$ has been a testing ground for many theoretical techniques. As mentioned above, the crystal structure shows a very short Re-Re distance of 2.24 Å, and qualitative molecular orbital arguments suggest the presence of a quadruple bond with a $\sigma^2\pi^4\delta^2$ ground state configuration. A full description of the metal-metal bonding, however, requires a quantum chemical method that goes beyond a single-determinant description like the Hartree-Fock model. In 2003, Roos and Gagliardi studied the electronic structure of $[Re_2Cl_8]^{2-}$ using the CASSCF/PT2 methodology. These calculations adopted a CAS(12,12) active space that includes the eight metal-based orbitals in Figure 1.2 and the eight electrons in them, and also the four metal-ligand orbitals (two bonding, two antibonding) with four electrons. The CASSCF calculations show that the ground state occupations of the δ and δ^* orbitals are 1.54 and 0.46, respectively, very different from the classical values of 2.0 and 0.0 for formally doubly occupied and unoccupied molecular orbitals, respectively. For the σ-manifold the natural orbital populations are 1.92 and 0.08 for σ and σ^*, respectively, reflecting the greater overlap of the σ orbitals. The natural orbital populations of π-symmetry are intermediate, with values of 3.74 and 0.26 for the bonding and antibonding orbitals, respectively. These occupations give a total Re-Re bond order of 3.20, much smaller than classical value of 4.0. The metal-ligand orbitals remain almost fully occupied in the wavefunction with bonding and antibonding occupations of 1.98 and 0.02, respectively. In 2006, Sakaki and co-workers[117] reinvestigated the electronic structure of $[Re_2Cl_8]^{2-}$ at the CASSCF level using a CAS(8,8) that includes just the bonding

and antibonding combinations of the metal-based orbitals as shown in Figure 1.2 and the eight electrons distributed among them. The σ and π components of the ground state wavefunction have the same occupations as the Ross and Gagliardi calculations, however, the occupations of the δ component are slightly different, 1.52 and 0.48 of δ and δ^* orbitals, respectively, giving bond order of 3.18. In fact, the weights of the main configurations, $\sigma^2\pi^4\delta^2$ and $\sigma^2\pi^4\delta^{*2}$, are 67% and 18%, similar to those reported by Benard and co-workers.[118] The $[Re_2Br_8]^{2-}$ analogue studied by Czerwinski and co-workers shows similar characteristics, with an effective Re-Re bond order of 3.32 and a contribution of 69% from the lead configuration to the wavefunction.[119] These results confirm the presence of a weak δ bond, and the importance of a multiconfigurational method. A different perspective on the strength of the δ bond in $[Re_2Cl_8]^{2-}$ comes from the work of Ohnishi and co-workers,[120] who calculated the energy difference between the $^1A_{1g}$ ground state and the $^3A_{2u}$ excited state, which lies 12 kcal/mol^{-1} higher in energy. The occupations of the δ and δ^* orbitals in the ground state are 1.52 and 0.48, respectively, but in the excited state they have almost equal populations of 1.01 and 0.99.

Metal-Metal Bonding: Cr_2, Mo_2, and W_2

The Cr_2 molecule has been used as a benchmark test for many theoretical methods, and has been variously reported to have a hextuple bond,[121–124] a single bond,[125] or no bond at all.[121] A bond length of 1.679 Å was reported by Bondybey and co-workers using laser-induced fluorescence spectroscopic experiment, but the reported dissociation energy of 1.53±0.06 eV is rather low.[121,126] The s^1d^5 electronic configuration leads to a formal bond order of six, but the very different contributions of the σ, π, and δ components to the overall bond strength mean that this simple picture may be misleading. CASPT2 calculations have been reported including in the active space six bonding orbitals, 4sσ, 3dσ, 3dπ, and 3dδ, along with the corresponding anti-bonding orbitals.[127,128] The 4s orbitals form a σ-bond with effective bond order of 0.90 while

the 3dσ-orbital pair form a bond with an effective bond order of 0.77. Each of the two components of the 3dπ bond have an effective bond order of 0.81 while each of the 3dδ orbitals have an effective bond order of 0.58. The total effective bond order of the Cr_2 molecule is therefore 4.45, rather closer to the quadruple bond than a truly hextuple or quintuple bond. Because the δ bond is very weak, these components of the bond are perhaps better considered as antiferromagnetically coupled 3dδ atomic orbitals rather than true bonds. Roos[127] has explored the potential energy surface for the Cr_2 molecule, and concluded that the minimum has a Cr-Cr distance of 1.66 Å and a bond energy of 1.65 eV, in excellent agreement with Bondybey's experimental estimates of 1.68 Å and 1.53 eV, respectively. The mismatch in size between the 4s and 3d orbitals means that the 4s-4s and 3d-3d components cannot be simultaneously optimized.

Within single determinant methods such as DFT, the weakness of the δ bond and, to a lesser extent, the π bond typically lead to symmetry breaking, wherein electrons of opposite spin localize on different metal centers. A study on the Cr_2 dimer by Bauschlicher at the BPW91 level shows net spin densities of ± 2.7 at opposite chromium centers, reflecting the tendency of the electrons within the δ and π components to be localized.[129] The potential energy surface of Cr_2 molecule has a minimum at the equilibrium separation of 1.68 Å as a result of the overlap between the 3d orbitals on two metal centers and a plateau is present in the region of 2.5 Å due to the overlap between the more diffuse 4s orbitals as shown by Casey and Leopold using negative ion photoelectron spectroscopy.[130] DFT calculations using different exchange-correlation functionals were used to study the electronic structure of chromium dimer. Bauschlicher's results show that the exchange-correlation functionals cannot reproduce the correct shape of the potential energy curve: only the BLYP functional is able to locate the first minimum, whereas hybrid functionals like B3LYP fail to capture the plateau region above 2.5 Å.[131]

The difference in size between the (n+1)s and nd orbitals in the second and third rows of the transition metals diminishes because relativistic effects play an important role in heavy transition metals. These relativistic effects tend to make the σ- and π-type orbitals more contracted, while those with higher angular momentum are expanded. Therefore, the bond in Mo_2 and W_2 dimers should be stronger compared to Cr_2, and indeed relativistic multi-configurational methods predict a bond energy of 4.41 eV for Mo_2 compared to an experimental value of 4.48 eV and 5.37 eV for the W_2 dimer compared to an experimental estimate of 5±1 eV.[115] The bond length was computed to be 1.95 Å for Mo_2 compared to 1.94 Å of the experimental value and 2.01 Å for W_2. The effective bond orders for Mo_2 and W_2 are 5.17 and 5.19, respectively, much closer to idealised bond order of 6.0 than the value computed for the Cr_2 dimer.

Metal-Metal Bonding: the Quintuple Bond

The synthesis and characterization of different types of dichromium structures (type I, II and II) with quintuple bonds has been addressed above, and their discovery has inspired a number of computational studies. The main difference between the quintuply bonded R-CrCr-R molecules and the naked Cr_2 dimer is that the 4s orbitals of the chromium centers are used to form metal-ligand bonds, leaving only five 3d electrons to support the quintuple interaction between the two metal centers, as shown in Figure 1.5. CASPT2 calculations on Ar′CrCrAr′ using an active space including all the bonding and antibonding orbitals in Figure 1.5 were done on a simplified model where the Ar′ ligands were replaced by phenyl rings: PhCrCrPh.[132] The structure of the PhCrCrPh mode optimized at CASPT2 level results in two different structures lying within 1 kcal mol^{-1} of each other. The first is a trans-bent isomer with a Cr-Cr bond length of 1.75 Å and Cr-C distances of 2.02 Å compared to 1.83 Å and 2.15 Å from X-ray, respectively. The underestimation of the Cr-C bond compared to the experimental value is probably due to use the simplified model of Ar′CrCrAr′ which

does not have the addition weak agostic-type interactions that are apparent in the crystal structure. The CASSCF wavefunction for PhCrCrPh is dominated by the lead $\sigma^2\pi^4\delta^4$ configuration, which has a weight of 45%. The doubly excited configuration $\sigma^2\pi^4\delta^2\delta^{*2}$ has a weight of 9%, highlighting again the weakness of the δ bond. The effective bond order of 3.52 is much smaller than the formal bond order of 5.0 from single determinant methodology. If the complete ligand is included in the model, the effective bond order is reduced further to 3.43.[115] The alternative PhCrCrPh structure has a linear arrangement with a short Cr-Cr bond length of 1.678 Å and a slightly longer Cr-C bond distance of 2.04 Å.

Calculations on a model of the $(\mu\text{-}\eta^2\text{-}^{H}\mathrm{L}^{iPr})_2\mathrm{Cr}_2$ system where the terphenyl moieties are removed from the ligands were performed by Gagliardi and co-workers.[133] The CASSCF wavefunction is dominated by the $\sigma^2\pi^4\delta^4$ configuration with total weight of 60%, with all other configurations contributing less than 5%. The effective bond order was found to be 3.43 made up of the following occupation numbers of the metal-metal bonding and antibonding orbitals of $\sigma(1.81)$, $\sigma^*(0.17)$, $\pi(1.81)$, $\pi^*(0.18)$, $\pi(1.80)$, $\pi^*(0.19)$, $\delta(1.70)$, $\delta^*(0.29)$, $\delta(0.75)$, $\delta^*(0.19)$. The same methodology has also been applied to molecules with ArMMAr and $\mathrm{M}_2(\mathrm{dpa})_4$ formulas where M is Cr, Mo, and W and Ar and dpa are 2,6-$(\mathrm{C}_6\mathrm{H}_5)_2$-$\mathrm{C}_6\mathrm{H}_3$ and 2,2'-dipyridylamide, respectively.[134] The effective bond order values and weights of the dominating configurations show that the magnitude of the metal-metal bond order increases in the order Cr<Mo∼W, similar to that found in PhMMPh and for the naked diatomic moleclues.[115,132]

1.3 Metal-Metal Bonding in Catalysis

Extensive reviews of the potential role of metal-metal bonding in catalysis have been presented by Uyeda and co-workers,[135,136] Berry,[137] and Mashima and co-workers.[138] Our understanding of the role of metal-metal bonding in catalysis is still very much

in its infancy,[135,139–141] but there is evidence to suggest that metal-metal bonds confer unique properties on catalysts that may be unachievable using a single transition metal. Catalysts with metal-metal bonding can be broadly classified into two categories (Figure 1.7): the first includes catalysts where one of the metal centers is active while the other plays an important electronic supporting role (single-site reactivity). In this case, the catalytic intermediates are often similar to those with single nuclear catalysts. However, the dinuclear structure of the catalyst gives opportunities to verify the catalyst activity by changing the strength of the metal-metal interactions between the two metal centers. Examples of this class are the Rh_2-based catalysts for carbene and nitrene transfer reactions.[142] In the second category, both metal centers bind to the substrates and mediate organometallic transformation (multi-site reactivity). Examples of this type of catalysts are more rare because the lack of suitable ligand framework that supports low-coordinate metal-metal bonds. Perhaps the best-known example is the $Co_2(CO)_8$-mediated Pauson-Khand reaction,[143,144] initiated by a dinuclear oxidative coupling of an alkene and alkyne to yield a dicobaltacyclic intermediate.

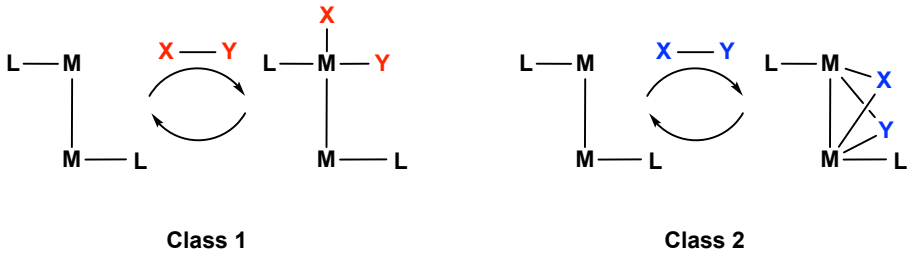

Figure 1.7: General classification of metal-metal bonds in catalysis.

The most important catalysts containing metal-metal bonds utilized in carbene and nitrene transfer reactions are the dirhodium paddlewheel complexes. This catalyst was discovered by Teyssie and co-workers[145,146] in the decomposition of ethyl diazoacetate by $Rh_2(OAc)_4$. Since then, dirhodium complexes have been used in a

wide range of applications in organic synthesis due to the high level of efficiency compared to mononuclear catalysts.[147,148] The carbene transfer reactions are thought to occur through Rh-CR_2 intermediates, where the carbene coordinates to one Rh center while the other center acting as an apical metallo-ligand. The dirhodium carbenes generated from diazoacetates and other acceptor groups are very electrophilic and target electron-rich bonds such as C-H and π-systems.

The electronic structure of model of carbene were recently proposed by Berry,[149] as shown in Figure 1.8. The Rh_2 carbene was described as a three-center two-electron interaction, where the fully occupied π^* orbital of the Rh-Rh bond overlaps with the unoccupied p-orbital of the carbene to generate an unoccupied molecule orbital polarized toward carbon. The Rh-CR_2 bond order is often described as a formal double bond, although calculated bond orders are significantly lower than two because of the delocalization of the π-system.[142]

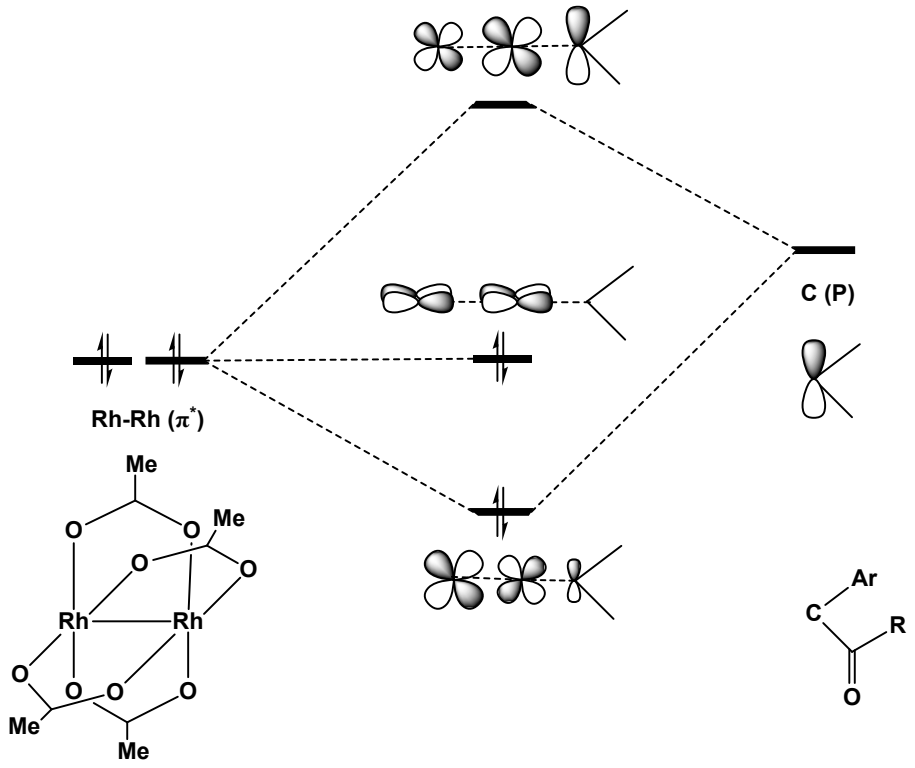

Figure 1.8: The electronic structure of the high electrophilic carbene intermediate.

The rhodium carbene intermediate complex was first observed and spectroscopically characterized in 2013 by Berry and co-workers,[150] and the crystal structure of this important intermediate was characterized in 2016 by Fürstner and co-workers.[151] These studies support the importance of the three-centre Rh-Rh-C π-orbital that is responsible for the high degree of electrophilicity of the dirhodium carbene. Davies and Berry show that the UV-Vis spectrum of the carbene complex features a band at 720 nm, characteristic of the $\pi \rightarrow \pi^*$ transition.[150]

1.4 This Thesis

In this thesis I focus largely on a different class of polymetallic molecules. A detailed introduction to the specific molecules of interest will be given in each chapter of this thesis, where I will be focusing on trimetallic systems and tetrametallic molecules as well as systems in the solid state. Nevertheless, in this section, I introduce a brief summary of the qualitative features of bonding that underpin the work in subsequent chapters. Summerville and Hoffmann investigated D_{3h}-symmetric face-sharing $[M_2(\mu{-}X)_3L_6]$ compounds using extended Hückel theory,[152] and their schematic molecular orbital diagram is shown in Figure 1.9. There three t_{2g} orbitals on each approximately octahedral metal are directed between the bridging ligands, and so can contribute to the metal-metal bond. The d_{z^2} orbitals one each metal interact to form σ and σ^* orbitals while the remaining two double degenerate t_{2g} orbitals on each metal have $2/3\delta{+}1/3\pi$ in character (at least in a perfect face-shared bioctahedron) and interact to form doubly degenerate δ_π and δ_π^* orbitals. The e_g-based orbitals on each metal center combine to form bonding and antibonding molecular orbitals with π_δ symmetry. Unlike the molecules without bridging ligands in Figure 1.2 where there is a clear separation between the π and δ manifolds, the presence of the bridging ligands mixes these two manifolds as shown in Figure 1.9.

The electronic structure of $[Ru_2Cl_9]^{3-}$ was the first to be investigated using the SCF-Xα-SW methodology, confirming the orbital ordering proposed by Hoffmann.[153] These orbitals are populated by ten electrons, leaving the σ^* orbital empty, giving bond order of one with a short Ru-Ru separation of 2.725 Å determined by X-ray crystallography. The electrochemistry of this compound gives access to three other oxidation states that are 4-, 2-, and 1-, where neither the structure nor the nature of metal-metal bonding are known but the UV-Vis spectra are reported. The electronic structure of the $[Ru_2Cl_9]^{z-}$ across a range of oxidation states will be investigated in chapter 4.

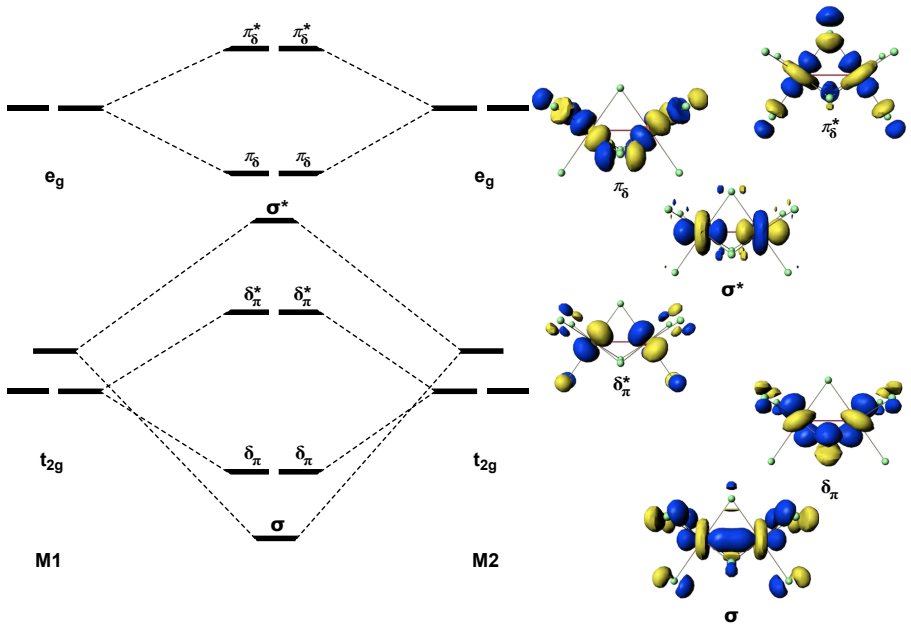

Figure 1.9: Molecular orbital arrays of face-shared octahedral molecules such as $[Ru_2Cl_9]^{3-}$.

Face-shared octahedral systems, $[M_2X_9]^{z-}$ with X = F, Cl, Br and I are known for most of the transition metals, and have been studied extensively using broken-symmetry density functional theory by Stranger and co-workers.[154–160] Unlike full symmetry method that force the electrons to delocalize, the broken-symmetry method admits both localized and delocalized of electrons situations, and so allows for the investigation of the opposing forces that influence the degree of metal-metal inter-

action. There are two factors influencing the formation of metal-metal bonds: the overlap between the metal-based orbitals which favours the delocalized scenario and hence strong covalent bonds, and single-ion exchange energy, which tends to localize the electrons and hence favour exchange coupling. For example, the metal-based orbital overlap in $[W_2Cl_9]^{3-}$ is strongest and the single-ion exchange is weakest, and the three metal electrons are strongly coupled. In contrast, the metal-based orbital overlap in $[Cr_2Cl_9]^{3-}$ is weak due to the less diffuse 3d-orbitals in first row transition metal, and the single-ion exchange energy is large for the same reasons, so the three electrons on each Cr center remain localized and there is no metal-metal bonding present. $[Mo_2Cl_9]^{3-}$ represents an intermediate situation where the σ-electrons are delocalized but the δ_π-electrons are localized, and the resultant flat potential energy surface is strongly influenced by the identity of the counter cation.

Metal-metal interactions across different oxidation states have been the target of only a few investigations. X-ray crystallography can, in principle, be used to gain useful information about metal-metal interactions at two different oxidation states through metal-metal separation, but it is relatively uncommon to isolate a molecule in two distinct oxidation states. One example is the crystal structure of $[W_2Cl_9]^{3-/2-/1-}$ has been characterized, where the W-W bond length increases from $\sim$2.45 Å to 2.540(1) Å and then 2.696(3) Å with successive oxidation due to the loss of weakly δ_π bonding electrons, however, the overall contraction of the W 5d orbitals may also have an impact.[161,162] For $[Re_2Cl_9]^{z-}$, z = 1 and 2, X-ray and SCF-Xα-SW theory have been used to study the metal-metal bonding, the results showing that the Re-Re bond is much stronger in the 2- state despite a reduction in formal bond order from 3.0 to 2.5 (2.704(1) Å vs 2.473(4) Å).[163] $[Re_2Cl_9]^{1-}$ has a well-developed σ-bond but the electrons in the δ_π orbital are localized and contribute little to the bond strength. In the 1-electron reduced state the formal δ_π bond order is reduced by 0.5, but this is more than compensated for by the radial expansion of the 5d-orbitals

which generate a much stronger σ-bond.[72]

The multi-configurational nature of the ground state and hence the strength of the metal-metal interactions in $[Re_2Cl_9]^{2-/-}$ were investigated by Sakaki and co-workers using complete active space self-consistent field method (CASSCF).[130] In this molecule there are six available orbitals to contribute in the formation of Re-Re bonds, two with σ-symmetry (σ and σ^*) and four with δ_π-symmetry (δ_π and δ_π^*). These six orbitals are populated with seven and six electrons in $[Re_2Cl_9]^{2-}$ and $[Re_2Cl_9]^{-}$, respectively. The Re-Re bonding in $[Re_2Cl_9]^{2-}$ was investigated at DFT and BS-DFT levels of theory. The results show that the ground state is a doublet with a bond order of 2.5 but a second quartet state (S=3/2) with a bond order of 1.5, lies very close in energy. CAS(7,6) calculations confirm the multiconfigurational nature of the ground state, with occupations of 1.87 and 0.13 for σ and σ^* orbitals, respectively, and 3.47 and 1.53 for δ_π and δ_π^*, respectively. The occupations of δ_π and δ_π^* orbitals differ substantially from formal values of 4 and 1, respectively suggested by DFT ($\sigma^2\delta_\pi^4\delta_\pi^{*1}$). In fact, the $\sigma^2\delta_\pi^4\delta_\pi^{*1}$ configuration makes up only 72% of the total wavefunction, and the Re-Re bond order is only 1.84 compared to the formal value of 2.5. The oxidation of $[Re_2Cl_9]^{2-}$ removes one electron, leading to a compression of the energy levels of the molecular orbital diagram of $[Re_2Cl_9]^{-}$. Therefore, we can expect that the wavefunction of the oxidized form is much more multiconfigurational than $[Re_2Cl_9]^{2-}$ itself. CAS(6,6) calculations indicate that ground state has $^1A_1'$ symmetry with natural orbital populations of 1.62 and 0.38 of σ and σ^*, respectively. Occupations of 2.18 and 1.82 for δ_π and δ_π^* orbitals, respectively, indicate that the contribution of the δ_π component to the net bond strength is negligible, and indeed the $\sigma^2\delta_\pi^4$ configuration makes up just 18% of the total CASSCF wavefunction of the $^1A_1'$ ground state. The Re-Re bond order of $[Re_2Cl_9]^{-}$ system is only around 0.80, much smaller than the formal bond order of 3.0.

1.5 Concluding Remarks

This introductory chapter tries to cover the story of the metal-metal bond and its applications, from both an experimental and theoretical perspective. The nature of the metal-metal bonding in all the species discussed can be understood, at least at a superficial level, using molecular orbital theory. The strengths and weaknesses of single determinant (DFT) and multiconfigurational (CASSCF) methods have been introduced, along with the potential uses of metal-metal bonds in catalysis. If we wish to characterize the metal-metal bonding in, for example, catalytic cycles, we must inevitably do so using *in-situ* spectroscopic tools rather than X-ray crystallography, which has been the workhorse technique for the field over the past 50 years. Equally, if we wish to establish how metal-metal bonding varies as a function of oxidation state, we must do so indirectly by interpreting the spectroscopic signatures of the intrinsically highly reactive redox-generated species. For example, the spectroscopic signatures of $[Ru_2Cl_9]^{z-}$ and $[Os_2Cl_9]^{z-}$ are known across a range of oxidation states (z = 1-4) and these spectra offer a wealth of information, if they can be interpreted fully. chapters 3 and 4 of this thesis are largely devoted to the goal of extracting information about metal-metal bonding from UV/visible spectra of electro-generated species.

Chapter 2

Elements of Theory: Configuration Interaction, Density Functional Theory, and Plane-Wave Method

In the previous chapter, we have seen how the description of the electronic structure of systems with transition metals, specifically the description of the nature of the metal-metal interactions, crucially depends on the applied quantum chemical methodology. For that purpose, in this chapter, we will briefly introduce the quantum chemical methods that are used to understand the electronic structure of the systems of interest. However, we will start from the basics of the Hartree-Fock method then more advanced methods will be considered that are single determinant (DFT) and multi-configurational (CASSCF) methods for molecular systems. The plane-wave techniques used for periodic systems will also be introduced.

2.1 Fundamental Concepts of Quantum Chemistry

The fundamental concept of quantum chemistry is to search for a solution to the nonrelativistic time-independent Schrödinger equation[164] in order to gain deep understanding to the electronic structure of atoms and molecules and thus understand their physical and chemical properties. The compact form of the nonrelativistic time-

independent Schrödinger equation is:

$$\hat{H}\psi = E\psi \tag{2.1}$$

where E is the total energy of the system under study which is an eigenvalue of the time-independent Hamiltonian $\hat{H}$ operator and ψ is the wavefunction. The wavefunction itself has no physical meaning, however, the square modulus of the wavefunction $|\psi|^2$ is interpreted as a probability density, the probability of finding a particle in a volume of space. The Schrödinger equation is an eigenvalue equation, the solution of this equation gives a complete set of orthogonal eigenfunctions ψ with corresponding eigenvalues E. The lowest energy wavefunction contains all possible information about the properties of a system in the ground state. The Hamiltonian operator for a system consisting of N-electrons is defined as:

$$\hat{H} = -\frac{\hbar^2}{2}\sum_{\alpha}\frac{1}{m_\alpha}\nabla_\alpha^2 - \frac{\hbar^2}{2m_e}\sum_{i}\nabla_i^2 + \sum_{\alpha}\sum_{\beta>\alpha}\frac{Z_\alpha Z_\beta e^2}{4\pi\varepsilon_o r_{\alpha\beta}} - \sum_{\alpha}\sum_{i}\frac{Z_\alpha e^2}{4\pi\varepsilon_o r_{i\alpha}} + \sum_{j}\sum_{i>j}\frac{e^2}{4\pi\varepsilon_o r_{ij}} \tag{2.2}$$

where α and β stand for the two nuclei and i and j stand for the two electrons. The first term in the above equation is the kinetic energy of the nuclei. The second term is the kinetic energy of the electrons. The third term is the potential energy of the repulsion between α and β nuclei with atomic number Z_α and Z_β, respectively, at distance $r_{\alpha\beta}$. The fourth term is the potential energy of attraction between the electrons and the nuclei at $r_{i\alpha}$. The last term is the potential energy of the repulsions between the electrons at r_{ij}. The Hamiltonian operator can be written in a compact form as:

$$\hat{H} = \hat{T}_n + \hat{T}_e + \hat{V}_{nn} + \hat{V}_{ne} + \hat{V}_{ee} \tag{2.3}$$

The electronic structure of any systems can, in principle, be determined by solving this nonrelativistic time-independent Schrödinger equation. However, because the correlated motion of particles, the exact wavefunction for many-particle systems remains inaccessible. Furthermore, the Hamiltonian operator for many-particle systems

contains pairwise attraction and repulsion terms, implying that no particle is moving independently of all of the others. Approximate solution of the Schrödinger equation with reasonable accuracy and cost need to be developed to tackle these problems.

An important simplification of the Hamiltonian operator is provided by the so-called Born-Oppenheimer approximation.[165] The Born-Oppenheimer approximation states that since the nuclei are much heavier than electrons, to a very good approximation the nuclei in a molecule are stationary with respect to electrons. Therefore, the Schrödinger equation can be separated into electronic and nuclear parts. Within the Born-Oppenheimer approximation, the kinetic energy of the nuclei $\hat{T}_n$ can be neglected and the repulsion between the nuclei $\hat{V}_{nn}$ can be considered to be constant.[166] The remaining terms of the Hamiltonian operator make up the electronic Hamiltonian ($\hat{H}_e$) and then the Schrödinger equation for electronic motion is:

$$\hat{H}_e \psi_e(r; R) = E_e \psi_e(r; R) \tag{2.4}$$

ψ_e is the electronic wavefunction which depends on the electronic coordinates r and has a parametric dependence on the nuclear coordinates R. The kinetic energy of the nuclei, $\hat{T}_n$, is ignored and the potential energy between nuclei, $\hat{V}_{nn}$, is constant for a given nuclear configuration. Thus, the electronic Hamiltonian operator $\hat{H}_e$ contains only the kinetic and potential energy terms of electrons.

$$\hat{H}_e = \hat{T}_e + \hat{V}_{ne} + \hat{V}_{ee} \tag{2.5}$$

The energy of a wavefunction can be calculated as an expectation value of Hamiltonian operator using the variational theorem.[166] According to the variational principle, the expectation value for the energy calculated with a trial wavefunction ψ' must be equal to or greater than the true ground state energy.

$$E' = \frac{\langle \psi' | \hat{H} | \psi' \rangle}{\langle \psi' | \psi' \rangle} \geq E_0 = \langle \hat{H} \rangle = \frac{\langle \psi_0 | \hat{H} | \psi_0 \rangle}{\langle \psi_0 | \psi_0 \rangle} \tag{2.6}$$

2.2 Hartree-Fock Theory

Hartree-Fock theory[167,168] provides a good starting point for many sophisticated theoretical methods which use better approximations to the electronic Schrödinger equation. For this reason, in this section, we will introduce Hartree-Fock theory at the basic level. The Hartree-Fock approximation seeks an approximate solution to electronic Schrödinger equation by assuming that the wavefunction can be written as a single Slater determinant. The Slater determinant is constricted from one spin-orbital per electron and the energy can be calculated by using the variational theorem to minimize the energy with orbital coefficients to get the best wavefunction. The Electron-electron repulsions in Hartree-Fock theory are treated in an average way, each electron is considered to be moving independently in a mean field created by other electrons.

A Slater determinant is an expression that describes the many-electron wavefunction in such a way it satisfies the anti-symmetry requirement of the wavefunction. According to the Pauli exclusion principle, the sign of the wavefunction must change upon exchange of two electrons $\psi(x_1, x_2) = -\psi(x_2, x_1)$. The Hartree product wavefunction of two electrons system has the form:

$$\psi_{HP}(x_1, x_2) = \chi_1(x_1)\chi_2(x_2) \tag{2.7}$$

This expression does not satisfy the anti-symmetry property of the wavefunction. However, this problem can be overcome by using the linear combination of two Hartree products.

$$\psi(x_1, x_2) = \frac{1}{\sqrt{2}}[\chi_1(x_1)\chi_2(x_2) - \chi_1(x_2)\chi_2(x_1)] \tag{2.8}$$

In determinant form:

$$\psi(x_1, x_2) = \frac{1}{\sqrt{2}} \begin{vmatrix} \chi_1(x_1) & \chi_2(x_1) \\ \chi_1(x_2) & \chi_2(x_2) \end{vmatrix} \tag{2.9}$$

This wavefunction now satisfies the anti-symmetry property and the electrons are no longer distinguishable. Furthermore, the wavefunction goes to zero if two electrons occupy the same orbitals at the same time. The general form of the Slater determinant[169] of an N-electron system is:

$$\psi(x_1, x_2, ..., x_N) = \frac{1}{\sqrt{N!}} \begin{vmatrix} \chi_1(x_1) & \chi_2(x_1) & \dots & \chi_N(x_1) \\ \chi_1(x_2) & \chi_2(x_2) & \dots & \chi_N(x_2) \\ \vdots & \vdots & \ddots & \vdots \\ \chi_1(x_N) & \chi_2(x_N) & \dots & \chi_N(x_N) \end{vmatrix} \tag{2.10}$$

The Hamiltonian operator simply consists of a one-electron operator and two-electron operator. The one-electron operator and the energy associated with this operator are:

$$h(i) = -\frac{1}{2}\nabla_i^2 - \sum_A \frac{Z_A}{r_{iA}} \quad \text{and} \quad E = \sum_i \langle i|h|i\rangle \tag{2.11}$$

The two-electron operator and it is corresponding energy are:

$$v(i,j) = \frac{1}{r_{ij}} \quad \text{and} \quad E = \frac{1}{2}\sum_{ij} [ii|jj] - [ij|ji] \tag{2.12}$$

Therefore, the total Hartree-Fock energy is the sum of one-electron and two-electron energies.

$$E_{HF} = \sum_i \langle i|h|i\rangle + \frac{1}{2}\sum_{ij} [ii|jj] - [ij|ji] \tag{2.13}$$

where $\langle i|h|i\rangle$ is the one-electron integral and has the form:

$$\langle i|h|i\rangle = \int \chi_i^*(x_1) h(r_1) \chi_i(x_1) dx_1 \tag{2.14}$$

and the two-electron integrals (in Chemist's notation) are called the Coulomb and exchange integrals as shown below, respectively.

$$[ii|jj] = \iint \chi_i^*(x_1)\chi_i(x_1)\frac{1}{r12}\chi_j^*(x_2)\chi_j(x_2) dx_1 dx_2 \tag{2.15}$$

$$[ij|ji] = \iint \chi_i^*(x_1)\chi_j(x_1)\frac{1}{r12}\chi_j^*(x_2)\chi_i(x_2) dx_1 dx_2 \tag{2.16}$$

The Coulomb integral has a classical analogue which is the electrostatic repulsion between two points charge. However, the exchange integral has no classical analogue

and therefore it is purely quantum mechanical property. Its effect is to reduce the repulsion between electrons of the same spin.

The Hartree-Fock equation has a similar form to the Schrödinger equation, however, it has Fock operator, $f(x_1)$, instead of the Hamiltonian operator.

$$f(x_1)\chi_i(x_1) = \epsilon_i\chi_i(x_1) \tag{2.17}$$

$f(x_1)$ has the form:

$$f(x_1) = h(x_1) + \sum_j 2J_j(x_1) - K_j(x_i) \tag{2.18}$$

The $J_j(x_1)$ term in this equation is the Coulomb interaction of an electron in spin-orbital χ_i with the average charge distribution of the other electrons, for this reason Hartree-Fock theory is often refereed to as a mean field theory. The mathematical formula of the Coulomb operator is:

$$J_j(x_1) = \int dx_2 |\chi_j(x_2)|^2 r_{12}^{-1} \tag{2.19}$$

and it gives the average local potential at point x_1 due to the charge distribution from the electron in orbital χ_j. The $K_j(x_1)$ term is the exchange term, and this arises from the anti-symmetry requirement of the wavefunction and has no classical analogue. The mathematical form of the exchange term which operates on an arbitrary spin-orbital χ_i is:

$$K_j(x_1)\chi_i(x_1) = \Big[\int dx_2 \chi_j^*(x_2) r_{12}^{-1} \chi_i(x_2)\Big]\chi_i(x_1) \tag{2.20}$$

The molecular orbitals used in Slater determinant can be generated by using the linear combination of atomic orbital (LCAO) approach.[170,171] By including the orbitals in LCAO fashion, we arrive at the Hartree-Fock-Roothaan equations.[172] According to the LCAO approach, the wavefunction for each spin-orbital can be defined as:

$$\chi_i = \sum_{\mu=1}^{K} C_{\mu i}\phi_\mu \tag{2.21}$$

Substituting this term in to the Hartree-Fock equation (2.17) leads to:

$$f(x_1)\sum_{\mu} C_{\mu i}\phi_{\mu}(x_1) = \epsilon_i \sum_{\mu} C_{\mu i}\phi_{\mu}(x_1) \tag{2.22}$$

By multiplying by $\phi_v^*(x_1)$ we get:

$$\sum_{\mu} C_{\mu i} \int dx_1 \phi_v^*(x_1) f(x_1)\phi_{\mu}(x_1) = \epsilon_i \sum_{\mu} C_{\mu i} \int dx_1 \phi_v^*(x_1)\phi_{\mu}(x_1) \tag{2.23}$$

In the matrix element notation, we have:

$$S_{v\mu} = \int dx_1 \phi_v^*(x_1)\phi_{\mu}(x_1) \tag{2.24}$$

$$F_{v\mu} = \int dx_1 \phi_v^*(x_1) f(x_1)\phi_{\mu}(x_1) \tag{2.25}$$

Then, the Hartree-Fock-Roothaan equations can be written as:

$$\sum_{\mu} F_{v\mu}C_{\mu i} = \epsilon_i \sum_{\mu} S_{v\mu}C_{\mu i} \tag{2.26}$$

Even more simply as matrices

$$FC = SC\epsilon \tag{2.27}$$

F is a Fock matrix, S is an overlap matrix, ϵ is a diagonal matrix which includes the energy of the orbitals, and C is the coefficient matrix.

$$\epsilon = \begin{vmatrix} \epsilon_1 & 0 & 0 & 0 & 0 \\ 0 & \epsilon_2 & 0 & 0 & 0 \\ 0 & 0 & \epsilon_3 & 0 & 0 \\ & & & \ddots & \\ 0 & 0 & 0 & 0 & \epsilon_k \end{vmatrix} \tag{2.28}$$

$$C = \begin{vmatrix} c_{11} & c_{12} & c_{13} & \dots & c_{1k} \\ c_{21} & c_{22} & c_{23} & \dots & c_{2k} \\ c_{31} & c_{32} & c_{33} & \dots & c_{3k} \\ \vdots & \vdots & \vdots & \ddots & \vdots \\ c_{k1} & c_{k2} & c_{k3} & \dots & c_{kk} \end{vmatrix} \tag{2.29}$$

Each column in the C matrix represents the coefficient of the spin-orbital in $\chi_i = \sum_{\mu}^{K} C_i\phi_{\mu}$ while each row represents the coefficient of the basis function in the same

equation. Because F depends on the orbitals, the process must be done iteratively through so-called self-consistent-field (SCF) process.

We have introduced the form of the integrals that are required in the self-consistent-field (SCF) procedure.[166] These integrals are the one-electron integral, two-electron integral, and the overlap integral. However, in order to start the self-consistent-field procedure we need to introduce one more term which is the density matrix. The electron density has the form:

$$\rho(r) = 2\sum_{i}^{\frac{N}{2}} |\chi_i(r)|^2 \tag{2.30}$$

Substituting 2.21 equation in this equation gives:

$$\rho(r) = \sum_{\mu v}^{K} 2\sum_{i}^{\frac{N}{2}} C_{\mu i}^{*} C_{vi} \phi_{\mu}^{*}(r)\phi_v(r) \tag{2.31}$$

$2\sum_{i}^{\frac{N}{2}} C_{\mu i}^{*} C_{vi}$ is the density matrix ($P_{\mu v}$). The Fock matrix consists of the core Hamiltonian matrix ($H_{\mu v}^{core} = \langle \mu | h_i(r_1) | v \rangle$) and two-electron term ($G_{\mu v} = [\mu v | \sigma \lambda] - \frac{1}{2}[\mu \lambda | \sigma v]$) of the Fock matrix.

$$F_{\mu v} = \langle \mu | h_i(r_1) | v \rangle + \sum_{\lambda \sigma}^{K} P_{\mu v} \Big\{ \mu v | \sigma \lambda] - \frac{1}{2}[\mu \lambda | \sigma v] \Big\} \tag{2.32}$$

The number of cycles in the SCF procedure to arrive at the final results depends on the initial guess of the density matrix. The self-consistent-field procedure is as follows:

1. Specify the molecular coordinate, basis set, charge, and multiplicity.
2. Calculate the overlap, one-electron, and two-electron integrals.
3. Diagonalize the overlap matrix.
4. Obtain guess of the density matrix $P^{(0)}$.
5. Calculate the Fock matrix F according to 2.32.

6. Diagonalize the Fock matrix F to calculate the coefficient matrix C.

7. From C form a new density matrix P^{i+1}.

8. Is the new matrix P^{i+1} close to guessing matrix $P^{(0)}$. If Yes, the calculation is converged, if No, go to step 5.

2.3 Electron Correlation and Post-HF Methods

As anticipated in previous section, the Hartree-Fock approximation replaced the instantaneous electron-electron repulsion with the averaged electron-electron repulsions. In a physical sense, the HF model allows electrons of the same spin to be too close to each other, however, in reality the electrons avoid each other. Therefore, a proper treatment of the individual electron-electron interactions must be considered. The difference between the exact energy and the Hartree-Fock energy with a complete basis set is called the correlation energy.[173]

$$E_{corr} = E_{exact} - E_{HF} \tag{2.33}$$

The correlation energy can be divided into two types, dynamic correlation, and non-dynamic (static) correlation.[174–176] Dynamic correlation arises from electron-electron repulsion based on the Coulomb law which is not exactly represented by Hartree-Fock model, while the non-dynamic refers to a case where a single determinant is insufficient to represent a nearly degenerate ground state wavefunction. Generally, improving accuracy of calculated energies and molecular geometry by including correlation effects is essential in the case of transition metal complexes even for qualitatively correct results. Therefore, to account for electron correlation effects one needs to go beyond HF theory (post-HF methods). One way to address the electron correlation problem is to use the HF wavefunction as a starting point and then try to make improvements to the HF results. An improvement to the Hartree-Fock wavefunction and its energy can be obtained by introducing configuration interaction.[166] In this method, the

wavefunction can be written as a linear combination of Slater determinates. Starting from the HF wavefunction then new determinants are generated by promoting electrons from occupied to virtual orbitals following the Aufbau principle. In this way a huge number of determinants can be built, promoting one electron from an occupied orbital to a virtual orbital, generated so-called single excited determinant (S). In the same way, we can relocate two electrons in the virtual orbitals to generate doubly excited determinant (D). This process can be continued until all electrons are promoted from occupied to virtual orbitals getting N-tuple excited determinants or the full-CI wavefunction. The expansion coefficients c_i are then determined variationally to yield the final CI wavefunction:

$$\psi_{CI} = c_0\psi_{HF} + \sum_S c_S\psi_S + \sum_D c_D\psi_D + \sum_T c_T\psi_T + \dots \tag{2.34}$$

The size of the CI wavefunction increase rapidly with the number of determinants, therefore, a full-CI calculation that yields the exact ground state energy can be obtained only for very small systems. The full-CI solution gives the lowest possible energy within a finite basis set limit and the difference between the HF and full-CI energies corresponds to the correlation energy for a given basis set. The computational coast can be reduced by using a limited number of excitations and the frozen-core approximation. Usually determinants only up to single, double and triple excitations gives $CISD$ and $CISDT$ methods. Both full-CI and limited CI methods are variational in character, but limited CI methods, in contrast to full-CI, are neither size-consistent nor size-extensive.

In the multi-configurational self-consistent-filed (MCSCF) method, the wavefunction is also multideterminanted, similar to the CI method, but two types of coefficients need to be optimized iteratively, the expansion coefficients in 2.34 and the spin-orbital coefficient in the excited determinants in 2.21. In contrast, in CI methods the coefficients of the orbitals are taken from the HF calculation. The main

challenge in MCSCF is the choice of the determinant to include in the calculations, since this process cannot be done automatically and the size of the configurational space that gives reasonable results is not always obvious. The choice of determinants in the CI wavefunction has been alleviated to some extent by applying the Complete Active Space SCF (CASSCF) method developed by Roos and co-workers.[111] CASSCF is widely used in electronic structure calculations because it depends on chemical intuition, to choose the type and number of determinants in the wavefunction. The molecular orbitals in CASSCF wavefunction are divided into three categories, the inactive, active, and virtual orbitals as shown in Figure 2.1. The inactive orbitals stay fully occupied in the wavefunction, there are basically core-orbitals, while in the active orbitals the average occupation varies from zero to two. The virtual orbitals stay empty in the wavefunction. The number of specific electrons in a number of specific orbitals is called the active space, and is denoted CAS(n, m), where n is the number of electrons and m is the total number of active orbitals. The full-CI wavefunction is constructed within the active space. The size of the active space of CASSCF calculations is usually reduced to less than the full number of valence electrons and orbitals to decrease the computational cost.

The CASSCF wavefunction captures the static correlation of near-degeneracy effects that appear between electrons at large separations in space. However, there is another type of correlation which comes from the interaction between electrons at a short distance which is called dynamic correlation. This type of correlation is not captured in the CASSCF wavefunction and it needs to be calculated to a great extent to obtain accurate energies, even though the wavefunction is not usually affected strongly. The dynamic correlation can be calculated using second-order perturbation theory on top of the complete active space wavefunction. Rayleigh-Schrödinger perturbation theory states that the Hamiltonian operator can split into terms, the unperturbed or zeroth-order Hamiltonian ($\hat{H}^0$) which is solvable and a perturbed

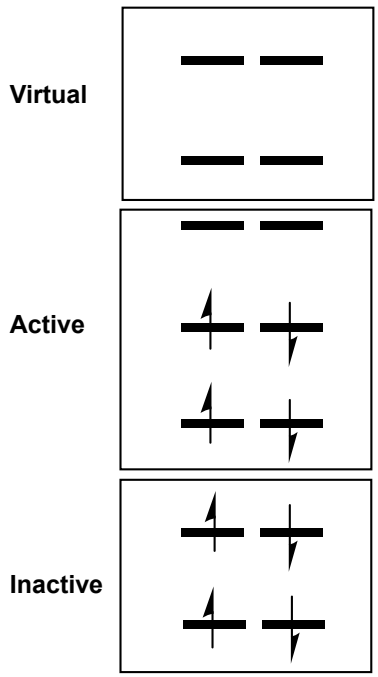

Figure 2.1: Schematic representation of CASSCF wavefunction.

Hamiltonian ($\hat{H}$) which is not solvable. The difference between the two Hamiltonians is the perturbation Hamiltonian ($\hat{H}'$). For the corresponding unperturbed Hamiltonian, we have unperturbed energy and unperturbed wavefunction.[177]

$$\hat{H}^0\psi_n^0 = E_n^0\psi_n^0 \tag{2.35}$$

Our task now is to relate the unknown energy and wavefunction of the perturbed Hamiltonian to the known energy and wavefunction of the unperturbed Hamiltonian. To do so, we insert a parameter into the Hamiltonian:

$$\hat{H} = \hat{H}^0 + \lambda\hat{H}' \tag{2.36}$$

When λ equals zero, we have the unperturbed system, and as λ increases, the perturbation increases. Since the Hamiltonian depends on λ, then the energy and wavefunction also depend on it. For the kth-order correction, the energy and wavefunction have the form:

$$\psi_n = \psi_n^0 + \lambda\psi_n^1 + \lambda^2\psi_n^2 + \cdots + \lambda^k\psi_n^k \tag{2.37}$$

$$E_n = E_n^0 + \lambda E_n^1 + \lambda^2 E_n^2 + \cdots + \lambda^k E_n^k \tag{2.38}$$

Now, we can write the first-order energy and second-order energy correction:

$$E_n^1 = \langle \psi_n^0 | \hat{H}' | \psi_n^0 \rangle \tag{2.39}$$

$$E_n^2 = \langle \psi_n^0 | \hat{H}' | \psi_n^1 \rangle \tag{2.40}$$

If we consider the sum of one-electron Fock operators as the unperturbed Hamiltonian, as suggested by Mϕller and Plesset, then the first-order energy correction is already included in the Hartree-Fock energy. However, the second-order energy correction which accounts for dynamical correction is missing from the Hartree-Fock energy. Including the second-order energy correction in the Hartree-Fock energy is called the second-order perturbation theory (PT2). Similarly, the missing dynamical correlation energy from CASSCF can be accounted by using perturbation theory, using the MCSCF wavefunction as the zeroth-order wavefunction.

2.4 Density Functional Theory

As we have seen in the previous sections, the electronic wavefunction of the n-electron system depends on $3n$ spatial and n spin coordinates. The Hamiltonian operator contains only one- and two-electron terms so the molecular energy can be written in terms of integrals involving only six spatial coordinates. This means the wavefunction of a many-electron system contains more information than is needed and lacking in direct physical significance. For this reason, functions that include fewer variables than the wavefunction but can still be used to calculate the energy and other properties of a molecular system are an attractive target. To do that, in 1964, Pierre Hohenberg and Walter Kohn established two theorems which serve as the fundamentals of density functional theory (DFT). To bring these theorems into practice, in 1965, Kohn and Sham introduced the Kohan-Sham method.[105,178] The two theorems and the method will be introduced in the following sections.

2.4.1 The Hohenberg-Kohn Theorems

The first Hohenberg-Kohn theorem[178] states that for a given molecule with a non-degenerate ground state, the ground-state energy, the wavefunction, and all other molecular electronic properties can be uniquely determined by the ground-state electron probability density ($\rho_0(x, y, z)$). The electron probability density is a function of only three variables. Thus, the ground-state energy is a function of the electron probability density.

$$E_0 = E_0[\rho_0] \tag{2.41}$$

The electronic Hamiltonian operator can be written as:

$$\hat{H} = -\frac{1}{2}\sum_{i=1}^{n}\nabla_i^2 + \sum_{i=1}^{n} v(r_i) + \sum_{j}\sum_{i>j}\frac{1}{r_{ij}} \tag{2.42}$$

$$v(r_i) = -\sum_{\alpha}\frac{Z_\alpha}{r_{i\alpha}} \tag{2.43}$$

In the electronic Schrödinger equation, the quantity $v(r_i)$ is the potential energy of interaction between electron i and the nuclei, while in DFT, this quantity is called the external potential acting on electron i. If we specify the external potential $v(r_i)$ and the number of the electrons, we can determine the electronic wavefunction and the allowed energies of the molecule as a solution to the electronic Schrödinger equation. The Hohenberg-Kohn theorem proved that for a system with a non-degenerate ground-state, the electron probability density $\rho_0(r)$ determines these two quantities (the external potential $v(r_i)$ and the number of electrons). Therefore, the ρ_0 determines the molecular electronic Hamiltonian and thus determines the wavefunction, energy, and all other properties.

$$E_0 = E_v[\rho_0] \tag{2.44}$$

The subscript v is used to emphasize that the ground-state energy depends on the external potential, which differs for different molecules. The ground state energy is

the sum of electronic kinetic energy terms, electron-nuclear attractions, and electron-electron repulsions.

$$E = \bar{T} + \bar{V}_{Ne} + \bar{V}_{ee} \tag{2.45}$$

Each term in this equation is determined by the ground-state density $\rho_0(r)$.

$$E_0 = E_v[\rho_0] = \bar{T}[\rho_0] + \bar{V}_{Ne}[\rho_0] + \bar{V}_{ee}[\rho_0] \tag{2.46}$$

$$\bar{V}_{Ne} = \sum_{i=1}^{n} v(r_i) = \langle \psi_0 | \sum_{i=1}^{n} v(r_i) | \psi_0 \rangle = \int \rho_0(r) v(r) dr \tag{2.47}$$

$$E_0 = E_v[\rho_0] = \int \rho_0(r) v(r) dr + \bar{T}[\rho_0] + \bar{V}_{ee}[\rho_0] \tag{2.48}$$

The value of the first term in equation 2.48 is the nuclear attraction potential-energy function for an electron located at point r, which is known, but the second and third terms are not known, and they do not depend on the external potential. This equation shows that the E_0 can be calculated from ρ_0 without having to find the molecular wavefunction, but it does not provide a practical way to perform this calculation. To calculate E_0 and other properties from ρ_0, we need the second Hohenberg-Kohn theorem and also the Kohn-Sham approach. The second Hohenberg-Kohn theorem states that for every trial density function $\rho_{tr}(r)$ that satisfies $\int \rho_0(r) dr = n$, where n is the number of electrons and $\rho_0(r) \geq 0$ for all r, the following inequality is true:

$$E_0 = E_v[\rho_0] \leq E_v[\rho_{tr}] \tag{2.49}$$

This proves that no trial electron density can give a lower ground-state energy than the true ground-state electron density, then,

$$E_0 = E_v[\rho_0] \leq E_v[\rho_{tr}] = \int \rho_{tr} v(r) dr + \bar{T}[\rho_{tr}] + \bar{V}_{ee}[\rho_{tr}] \tag{2.50}$$

2.4.2 The Kohn-Sham (KS) Method

In 1965, Kohn and Sham[105] came with a practical method to calculate the electron density (ρ_0) and to find the ground-state energy (E_0) from the electron density. In

the Kohn-Sham approach, a fictitious reference system of n non-interacting electrons was considered. In this reference system, each electron experiences the same external potential-energy function, denoted $v_s(r_i)$. The $v_s(r_i)$ makes the ground-state electron probability density $\rho_s(r)$ of the reference system equal to the exact ground-state electron probability density $\rho_0(r)$ of the system of interest. Considering the Hohenberg-Kohn theorem, once $\rho_s(r)$ is defined for the reference system, the $v_s(r_i)$ is uniquely determined.

Kohn and Sham defined the $\bar{T}[\rho_0]$ and $\bar{V}_{ee}[\rho_0]$ terms of the Hohenberg-Kohn equation (2.48) as:

$$\Delta\bar{T}[\rho] = \bar{T}[\rho] - \bar{T}_s[\rho] \tag{2.51}$$

$$\Delta\bar{V}_{ee}[\rho] = \bar{V}_{ee}[\rho] - \frac{1}{2}\iint \frac{\rho(r_1)\rho(r_2)}{r_{12}} dr_1 dr_2 \tag{2.52}$$

where s indicates the reference system and r_{12} is the distance between points x_1,y_1,z_1 and x_2,y_2,z_2. The second term of the last equation (2.52) is the classical expression for the electrostatic interelectronic repulsion energy if the electrons were smeared out into a continuous distribution of charge with electron density ρ. Therefore, equation 2.48 becomes:

$$E_v[\rho] = \int \rho_0(r)v(r)dr + \bar{T}_s[\rho] + \frac{1}{2}\iint \frac{\rho(r_1)\rho(r_2)}{r_{12}} dr_1 dr_2 + \Delta\bar{T}[\rho] + \Delta\bar{V}_{ee}[\rho] \tag{2.53}$$

The $\Delta\bar{T}$ and $\Delta\bar{V}_{ee}$ functionals are unknown and they define the exchange-correlation energy functional $E_{xc}[\rho]$.

$$E_0 = E_v[\rho] = \int \rho(r)v(r)dr + \bar{T}_s[\rho] + \frac{1}{2}\iint \frac{\rho(r_1)\rho(r_2)}{r_{12}} dr_1 dr_2 + E_{xc}[\rho] \tag{2.54}$$

The three terms of the right-hand side of 2.54 are easy to evaluate from the electron density ρ and also, they include the main contribution to the ground-state energy. The fourth term is relatively small but essential and not easy to evaluate accurately.

Before we going to look at the exchange-correlation term in detail; we consider the first and second terms of 2.54. Using equation 2.43, the first term becomes:

$$\int \rho(r)v(r)dr = -\sum_{\alpha} Z_{\alpha} \int \frac{\rho(r_1)}{r_{1\alpha}} dr_1 \tag{2.55}$$

which is easy to calculate if we know the electron density. The second term ($\bar{T}_s[\rho]$) is the kinetic energy of the reference system whose wavefunction is the anti-symmetrized product (Slater determinant) of the lowest-energy Kohn-Sham spin-orbitals u_i^{KS}:

$$\psi_s = |u_i^{KS} u_2^{KS} \dots u_n^{KS}| \qquad u_i^{KS} = \theta_i^{KS}(r_i)\sigma_i \tag{2.56}$$

and the Hamiltonian operator has the form:

$$H_s = \sum_{i=1}^{n} [-\frac{1}{2}\nabla_i^2 + v_s(r_i)] = \sum_{i=1}^{n} h_i^{KS} \tag{2.57}$$

$$h_i^{KS}\theta_i^{KS} = \epsilon_i^{KS}\theta_i^{KS} \tag{2.58}$$

h_i^{KS} is the one-electron Kohn-Sham Hamiltonian, θ_i^{KS} is the spatial part of Kohn-Sham orbital, ϵ_i^{KS} is Kohn-Sham orbital energy and σ_i is the spin part, either α or β.

$$\bar{T}_s[\rho] = -\frac{1}{2}\sum_i \langle \theta_i^{KS}(1)|\nabla_1^2|\theta_i^{KS}(1\rangle) \tag{2.59}$$

The electron density related to the Kohn-Sham orbital is:

$$\rho = \rho_0 = \sum_{i=1}^{n} |\theta_i^{KS}|^2 \tag{2.60}$$

Now we can find E_0 from ρ if we can find the KS-orbital θ_i^{KS} and if we know the E_{xc} functional. The KS orbitals can then be found using the second Hohenberg-Kohn theorem. Just like the Fock operator, one can show that the Kohn-Sham orbitals that minimize equation 2.60 for the molecular ground state energy satisfy:

$$\Big[-\frac{1}{2}\nabla_1^2 - \sum_{\alpha} \frac{Z_{\alpha}}{r_{1\alpha}} + \int \frac{\rho(r_2)}{r_{12}} dr_2 + v_{xc}(1) \Big] \theta_i^{KS}(1) = \epsilon_i^{KS}\theta_i^{KS}(1) \tag{2.61}$$

The exchange-correlation potential (v_{xc}) is found as the functional derivative of the exchange-correlation energy (E_{xc}) respect to electron density ($dE_{xc}[\rho(r)]/d\rho(r)$).

$$\Big[-\frac{1}{2}\nabla_1^2 + v_s(1)\Big]\theta_i^{KS}(1) = \epsilon_i^{KS}\theta_i^{KS}(1) \tag{2.62}$$

$$h^{KS}\theta_i^{KS}(1) = \epsilon_i^{KS}\theta_i^{KS}(1) \tag{2.63}$$

2.4.3 The Exchange-Correlation Functionals

The exchange-correlation energy term contains the kinetic correlation energy, exchange energy, coulombic correlation energy, and self-interaction correction. The kinetic correlation energy is the kinetic energy difference between the real molecule and the reference system. The exchange energy arises from the antisymmetry requirement. The coulombic correlation energy is associated with interelectronic repulsions. The self-interaction comes from the classical charge-cloud electrostatic repulsion expression which allows the portion of electron density in dr_1 that arises from the smeared-out part of a particular electron to interact with the charge contributions of that same electron to electron density throughout space. The key to an accurate KS-DFT calculation is to find a good approximation to E_{xc} term, but this clearly represent a great challenge.

Local Density Methods

Local density approximation assume that the exchange-correlation energy at a particular point can be calculated exclusively from the value of the density at that point. In the LDA approximation, a hypothetical electrically neutral object that has an infinite number of interacting electrons moving in a space where the positive charge is continuously and uniformly distributed is used. If the electron density (ρ) varies extremely slowly with the position, then the exchange-correlation function can be written as:

$$E_{xc}^{LDA}[\rho] = \int \rho(r)\epsilon_{xc}(\rho)dr \tag{2.64}$$

The integral over all space, dr stands for dx, dy, and dz, and $\epsilon_{xc}(\rho)$ is the exchange and correlation energy per electron in uniform electron gas with electron density ρ. The exchange-correlation energy can be written as a sum of exchange and correlation parts.

$$\epsilon_{xc}(\rho) = \epsilon_x(\rho) + \epsilon_c(\rho) \tag{2.65}$$

The exchange part has the form:

$$\epsilon_x(\rho) = -\frac{3}{4}\left(\frac{3}{\pi}\right)^{\frac{1}{3}}(\rho(r))^{\frac{1}{3}} \tag{2.66}$$

The correlation part of the energy has been calculated by Vosko, Wilk, and Nusair (VWN).[179]

$$\epsilon_c(\rho) = \epsilon_c^{VWN}(\rho) \tag{2.67}$$

For open-shell systems and near dissociation geometries, the local-spin-density approximation (LSDA) gives better results than the LDA. The difference between these two functionals is that in LDA the two electrons with opposite spins occupy the same KS spatial orbitals, while LSDA allows each electron to occupied a different KS spatial orbital.

$$E_{xc}^{LSDA}[\rho^\alpha(r), \rho^\beta(r)] = \int \rho(r)\epsilon_{xc}[\rho^\alpha(r), \rho^\beta(r)]dr \tag{2.68}$$

The LDA and LSDA functionals are based on uniform electron gas where the electron density varies very slowly with the position.

Gradient Corrected Methods

In cases where the electron density varies rapidly with the position, the approximation to the exchange-correlation energy must be moved beyond the LDA methods. The gradient of the density $\nabla\rho$ needs to be considered as well as the density ρ itself. The approximation that is used to consider the variation of the electron density with the position is called the Gradient-Corrected approximation (GGA). A large number of

GGAs have been proposed based on the following general formulation:

$$E_{xc}^{GGA}[\rho^{\alpha}(r), \rho^{\beta}(r)] = \int f(\rho^{\alpha}(r), \rho^{\beta}(r), \nabla\rho^{\alpha}(r), \rho^{\beta}(r))dr \tag{2.69}$$

where f is some function of the spin densities and their gradients. Likes the LDA and LSDA, the exchange-correlation energy from the GGA functional can be separated into two parts dealing with exchange and correlation. The earliest and most commonly used GGA exchange functional (B88) was proposed by Becke in 1988 as a correction to the LSDA exchange energy.[180] It contains a single empirical parameter calculated by fitting to the exchange energies of the six noble gas atoms. The correction to the LSDA correlation part was proposed by Perdew in 1986 (P86), and uses one empirical parameter fitted to the correlation energy of the neon atom.[181] This correlation functional were later modified by Perdew and Wang (PW91).[182] Lee, Yang and Parr proposed the most extensively used functional, LYP[183] which contains four empirical parameters optimized by fitting to the helium atom. The performance of the GGA functionals is much better than LSDA and geometries and vibrational frequencies computed by GGA are usually also superior to MP2 results. An extensive literature on BLYP and BP86 has established the reliable accuracy of these functionals for a variety of systems, although they do have problems in predicting of relative energies of different electronic states.

Functionals dependent on the kinetic-energy density are called meta-GGA functionals, which can also include the second derivative of the density ρ.

$$E_{xc}^{MGGA} = \int f(\rho_{\sigma}(r), \nabla\rho_{\sigma}(r), \nabla^2\rho_{\sigma}(r)\tau_{\sigma})dr \tag{2.70}$$

The kinetic energy density for the occupied Kohn-Sham orbitals θ_i^{KS} is defined as:

$$\tau_{\sigma} = \frac{1}{2}\sum_i |\nabla\theta_i^{KS}|^2 \tag{2.71}$$

The meta-GGA functional (B95) proposed by Becke shows that the correlation vanishes for a one-electron problem and so free of the self-interaction, giving a significant

advantage over the previous functionals.[184] The improvement of the GGA functionals through meta-GGA is, however, counteracted by a higher computational cost due to their additional complexity.

Hybrid Methods

The approximate exchange part of the functional can be replaced by the HF exchange energy because the HF exchange energy of a Slater determinant can be calculated exactly. This would seem promising, however, in practice such a hybrid method represents no improvement over GGA functionals because when the exact HF exchange is used the cancellation of errors that occurs in case of approximate exchange and correlation functionals does not work. Including some percentage of exact exchange into density functionals does, however, lead to significant improvements. In 1993 Becke proposed the first successful hybrid functional, the three-parameter B3PW91 functional which has 20% exact exchange.[185]

$$E_{xc}^{B3PW91} = (1-a)E_x^{LSDA} + 0.20E_x^{HF} + 0.72\Delta E_x^{B} + E_c^{LSDA} + 0.81\Delta E_c^{PW91} \quad (2.72)$$

The parameters were chosen to give good fits to experimental molecular atomization and ionization energies. Stevens and co-workers modified this functional to use LYP instead of PW91, this leads to B3LYP functional which is the most popular hybrid functional used now.[186]

$$E_{xc}^{B3LYP} = 0.80E_x^{LSDA} + 0.20E_x^{HF} + 0.72\Delta E_x^{B88} + 0.19E_c^{VWN} + 0.81E_c^{LYP} \quad (2.73)$$

The PBE functional is also improved by including 25% exact exchange to give the PBE0 functional.[187] The 50% exact exchange is included in half-and-half BHandH and BHandHLYP functionals. A arrange of hybrid metal-GGA functionals has been tested on different systems and they generally show excellent accuracy, for example, M06, M06-HF, M06-2X and M05-2X which were developed by the group of Truhlar.

2.5 Basis Sets

Orbitals are naturally used in both wavefunction-based methods such HF and post-HF and density-based methods such as DFT. Basis-free DFT implementations do exist, but in most quantum chemical software the KS orbitals are expanded in a set of basis functions. The purpose of this section is to introduce the fundamental concepts and issues regarding the construction and use of basis set. An atomic orbital (AO) consists of two parts, the spherical harmonic ($Y_l^m(\theta, \phi)$) which determine the shape of the orbital, and the radial part ($R(r)$) which control the size of the orbital.[177]

$$\psi = R_n(r)Y_l^m(\theta, \phi) \tag{2.74}$$

n is the principal quantum number, l is the angular momentum quantum number, and m is the magnetic quantum number of an atomic orbital. The radial part of the wavefunction depends on r so it takes different forms while the spherical part stays unchanged. Therefore, for a many-electron system we need to look carefully at the radial part of the wavefunction. Basis sets can be classified into Slater-type (STOs) or Gaussian-type (GTOs) depending on the form of the radial part. The formula of an STO is:

$$\psi^{STO} = Nr^{n-1}e^{-\zeta r}Y_l^m(\theta, \phi) \tag{2.75}$$

where N is the normalization factor. The advantage of STOs is that they have the same dependence on r (e^{-r}) as the eigenfunctions of the Schrödinger equation for the hydrogen atom. The formula of GTOs is defined as:

$$\psi^{GTO} = Nx^l y^m z^n e^{-\alpha r^2} \tag{2.76}$$

x, y, and z are the cartesian coordinates. The main difference between STOs and GTOs is the latter has e^{-r^2} dependence. STOs have a cusp at the nucleus, and reproduce well the hydrogenic atomic orbitals (Figure 2.2). In contrast, the GTOs have no cusp near the nuclei and tend to zero much faster than STOs at large distances

from the nucleus. Despite these shortcomings, GTOs are far easier to use computationally compared to STOs because the product of two GTOs centered on different atoms produces a third GTO located in between. This results the calculation of one- and two-electron integrals much easier. The accuracy of STOs and the numerical convenience of GTOs can be combined by using not an individual GTO but a linear combination of several primitive GTOs to model a single STO.

$$\chi^{CGF} = \sum_i a_i \chi_i^{GTO} \tag{2.77}$$

where CGF stand for contracted Gaussian function. Most standard quantum chemistry software packages implement basis sets of GTOs type apart from the Amsterdam Density Functional (ADF) package which uses Slater-type basis set.

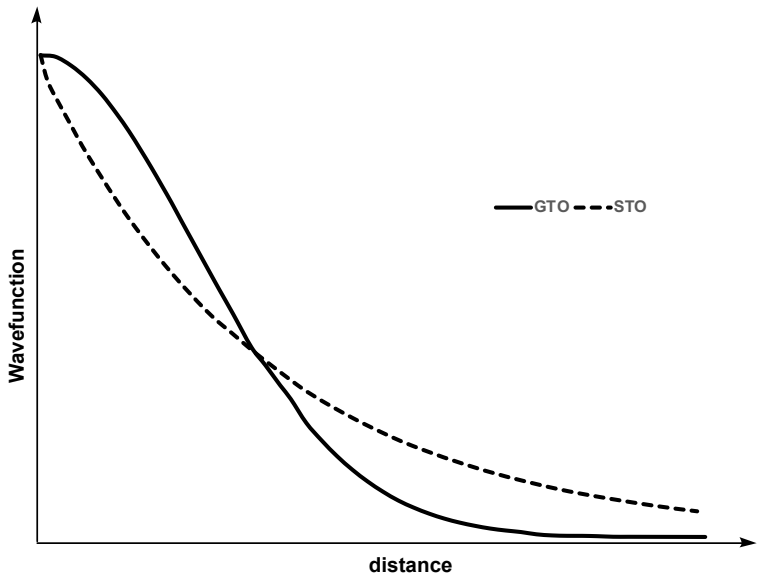

Figure 2.2: Comparison between STO and GTO.

Commonly, basis sets are classified according to the number of functions included: if only one basis function is used to represent the atomic orbital then the results is a minimal basis set which is referred as being of single-ζ (SZ) quality. For example, in the minimal STO-3G developed by Pople and co-workers,[188] each basis function is formed as a linear combination of three GTOs. In order to go beyond a purely

qualitative level, more sophisticated basis set must be considered, using two or more functions for each type of orbital; double-ζ (DZ), triple-ζ (TZ), *etc.*

Valence electrons usually experience changes during chemical process, and so the design of basis sets that allow high flexibility in the valence region must be considered. For example, the 6-31G basis set describes the core orbitals by a single contracted Gaussian function constructed from six primitive GTOs whereas the valence region is described by two functions, one of which consists of three primitives and the other only one.[189] Polarization functions have higher angular momentum than the orbitals occupied in the atomic ground-state and their inclusion allows orbitals to distort to adapt better molecular environment. Polarized double-ζ (DZP) and triple-ζ (TZP) are routinely used in DFT calculations.

2.6 Quantum Chemistry in Periodic Systems

If we compare the solution of the Schrödinger equation of a molecule to an extended solid-state system, we face the immediate problem that the dimensions of the system are infinite. However, introducing the translational symmetry properties of the crystal through Bloch's theorem,[190] allow us to consider only the number of electrons within the fundamental repeating unit, the unit cell.

Bloch's Theorem

Bloch's theorem employs translational symmetry to produce the crystal wavefunction made up of crystal orbitals. Therefore, in any idealized solid-state system whose electronic potential (V) reflects the periodicity of the lattice which is given by a lattice vector (T), then, $V(r+T) = V(r)$ because the potential is identical within each crystallographic unit cell. Bloch's theorem states that for a given wavefunction ($\psi(k,r)$) which satisfies the Schrödinger's equation, there exists a vector k such that

translation by a lattice vector T is equivalent to multiplication by a phase factor.

$$\psi(k, r+T) = e^{ikT}\psi(k, r) \tag{2.78}$$

The left-hand side of this equation is an extended wavefunction that is a function of a lattice vector T. This wavefunction is created from the crystal orbital of one specific site within the unit cell. Thus, we only need to know the wavefunction at this particular point, and then it would be known for the whole crystal $r+T$, due to the system being translationally invariant. The wavefunction is symmetry-adapted to the infinite system by the quantum number k.

The crystal orbital ($\psi(k, r)$) can be expanded over a series of localized atomic orbitals (ϕ_j) which lie on some atomic positions (r_j) inside the unit cell. Thus,

$$\psi(k, r) = \sum_j e^{ikrj}\phi_j \tag{2.79}$$

This equation corresponds to the molecular LCAO ansatz (2.21), adapted to an extended system. The atomic orbitals of the right-hand side of the above equation are weighted by mixing coefficients which are identical to the Bloch exponential factor, generating an extended wavefunction.

Reciprocal Space and the k Quantum Number

The quantum number (k) is located in reciprocal space because it has the dimensions inverse length.[191] Any position in real space is given by the real-space vector R which is a linear combination of the three basic vectors a_1, a_2, and a_3. In the same way, for any reciprocal space, a lattice vector K is built up from the reciprocal basic vectors g_1, g_2, and g_3.

$$R = n_1a_1 + n_2a_2 + n_3a_3 \tag{2.80}$$

$$K = m_1g_1 + m_2g_2 + m_3g_3 \tag{2.81}$$

The real-space and reciprocal-space can be linked as:

$$g_1 = \frac{2\pi}{V}(a_2 + a_3), \quad g_2 = \frac{2\pi}{V}(a_3 + a_1), \quad g_3 = \frac{2\pi}{V}(a_1 + a_2) \tag{2.82}$$

where the volume $V = a_1(a_2 \mathrm{x} a_3)$, for one dimensional infinite system with $R = a_1$, then $g_1 = 2\pi/a_1$ as we expected because $2\pi/a_1$ is the reciprocal vector of a_1. The quantum number (k) gives information about the energies of these electrons and their crystal momentum. The k-dependent wavefunction is called a crystal orbital, and each k might have many one-electron wavefunctions, similar to a molecule with many molecular orbitals. The values of the quantum number (k) can be simply calculated from periodic boundary conditions as long as the unit cell is periodically repeated. For a one-dimensional case, if we consider a crystal of length (L) that consists of a large number of unit cells with lattice parameter (a) and if the wavefunction is identical at both left and right ends, then Bloch's theorem for any value of k would yield:

$$\psi(k, 0) = \psi(k, L) = e^{ikL}\psi(k, 0) \tag{2.83}$$

The values of the quantum number (k) are $0 \leq k \leq \pi/a$, and this part of the reciprocal space is called the Brillouin zone, which can be considered as a unit cell in reciprocal space. The quality of the calculations depends on the number of k points, a large number of k points is needed for smooth representation of reciprocal space. The size of the unit cell determines the size of the basis set, then, the quality of calculations also is determined by the number of basis functions in the unit cell of the real space.

Potentials and Plane-Wave

In extended solid-state systems,[191] the translation symmetry needs to be considered, therefore, we need to use different types of basis functions from those of molecular systems. Local basis functions such as STOs and GTOs are not efficient and Bloch's theorem suggests that the natural basis function for a translational invariant solid is a plane-wave (e^{ikr}). Generally, the plane-wave can be expressed by any kind of crystal wavefunction which is a linear combination of various exponential functions.

$$\psi_n(k, r) = e^{ikr} \sum_k c_n(k, K) e^{iKr} \tag{2.84}$$

c_n are the mixing coefficients which must be calculated either analytically or numerically similar to LCAO-MO method. The plane-wave can be used as a direct basis functions if there were not a rapid oscillation of the atomic wavefunction close to the nuclei due to the high kinetic energy of electrons as shown in Figure 2.3.

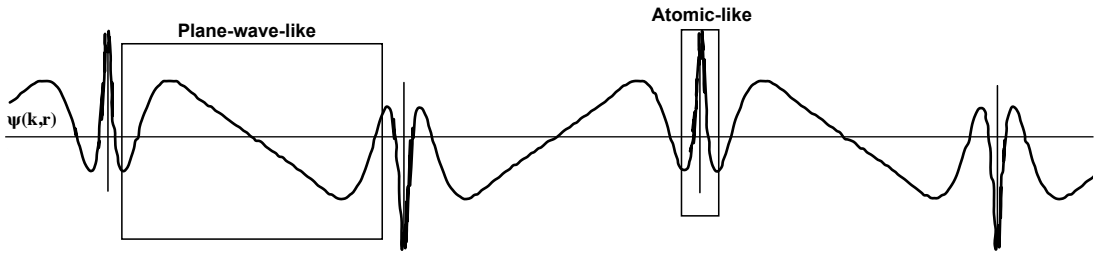

Figure 2.3: Schematic drawing of a 3s-derived Bloch function of a one-dimensional crystal of sodium atoms.

From Figure 2.3 we can clearly see that the wavefunction close to the nuclei oscillates rapidly, whereas in the bonding region we have a smooth function. This behavior is not easy to capture by using plane-wave because the oscillation of the core-like function requires very short wavelengths. However, the core-like function can be treated by the so-called pseudopotential approach proposed by Hellmann.[192–194] The concept is to remove these oscillations by replacing the strong ion-electron potential by a much weaker pseudopotential. The valence electrons experience a lower nuclear charge which is somewhat screened by the core electrons. Furthermore, the valence electrons cannot enter the core region because of the Pauli principle, all core levels are filled so there is a strong repulsion between valence and core electrons. These two opposite effects, the Coulomb attraction of the valence electrons by the nucleus but Pauli repulsion of the valence electrons by core electrons, almost completely cancel each other and only a weak pseudopotential is left.

DFT+U Approach

So far, we have introduced the fundamental theories needed to perform a periodic calculation. However, to use DFT in practice we need to introduce Hubbard U method

because DFT performs poorly in case of strong correlation, when electrostatic interactions between the electrons are poorly described by LDA or GGA. The fundamental phenomena behind DFT+U is to treat the strong on-site Coulomb interaction of localized electrons with an additional Hubbard-like term. The on-site interactions consist of U (Coulomb) and J (exchange), and the U parameter in the Hubbard model is defined as the energy required to remove an electron from one site and pair it with an electron on another site. In some transition metals and their compounds, the Hubbard U can have a dominate effect on the properties, for example, some insulating transition metal oxides (Mott insulators) are predicted to be metals at the LDA level because the local Coulomb repulsion experienced by the electrons within the d-orbital is underestimated.[195,196] The DFT+U corrections can be introduced in ab initio calculations in varies ways. Liechtenstein and co-workers,[197] proposed that the U and J enter as independent corrections in the calculations. The other approach which is widely used proposed by Anasimov and co-workers[198] using a single effect U_{eff} which U-J for the Coulomb interaction. Thus, the DFT+U total energy can be calculated as:

$$E_{DFT_U} = E_{DFT} + \sum_a \frac{U_{eff}}{2} Tr(\rho^a - \rho^a \rho^a) \tag{2.85}$$

where ρ^a is the atomic orbital occupation matrix. The second term is a penalty functional to the DFT total energy which forces the on-site occupancy matrix to either full occupied or completely empty.

Chapter 3

Metal-Metal Bonding in Face-Shared Trinuclear Metal Chains: The Effect of the Identity of the Central Metal Ion and Oxidation State

3.1 Introduction

This chapter focusses on the electronic structure of tri-metallic systems based on the face-shared octahedral architecture, with general formula $L_3M(MCl_6)ML_3$ (Figure 3.1). These clusters have approximate D_{3d} symmetry with three metal ions lying on a common three-fold rotation axis: each terminal metal ion has an approximately C_{3v}-symmetric local coordination environment, while the central metal ion is, to a good approximation, octahedral. The first member of this class to be synthesized was the all-chlorine species, $[Cl_3Ru(RuCl_6)RuCl_3]^{4-}$ (Figure 3.1), reported by Cotton in 1980.[199] Since that initial work, closely-related systems have been synthesized by changing either the identity of the metal ions or by substituting different ligands on the terminal ions. Amongst the first, homoleptic, category, $[Cl_3Mo(MoCl_6)MoCl_3]^{z-}$ and $[X_3Ti(TiX_6)TiX_3]^{z-}$ (X = Cl, Br and I) are all known while in the latter, the phosphine- and arene-terminated chains $[(PR_3)_2ClRu(RuCl_6)RuCl(PR_3)_2]^{0/+}$ (R = Et and tBu), $[(PEt_3)_3Ru(RuCl_6)Ru(PEt_3)_3]^{+}$ and (p−cymene)Ru($RuCl_6$)Ru(p−cymene) have also

been synthesized, primarily in the groups of Cotton and his co-workers.[200–207]

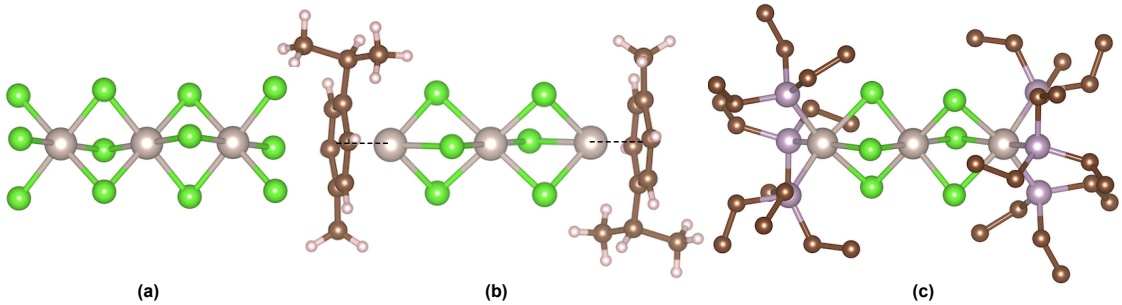

Figure 3.1: The structure of tri-metallic system, $[Ru_3Cl_{12}]$ (a) system along with $[Ru_3Cl_6(p{-}cymene)_2]$ (b) and $(PEt_3)_3Ru[MX_6]Ru(PEt_3)_3$ (c) systems of our interest, where M = Ru (1), Rh (2), and Ir (3). Hydrogen atoms was omitted for clarity.

The electronic structure of $[Cl_3Ru(RuCl_6)RuCl_3]^{4-}$ was investigated in detail using the SCF-X_α-SW methodology by Bursten and Cotton,[153] and their molecular orbital diagram is reproduced schematically in Figure 3.2. The frontier-orbital region features nine molecular orbitals constructed from linear combinations of the t_{2g} orbitals on each (approximately octahedral) metal center. These orbitals split into a σ manifold made up of linear combinations of the d_{z^2} orbital aligned along the trigonal axis (σ, σ^{nb} and σ^*) and a manifold of three doubly degenerate orbitals with mixed δ and π symmetry (denoted δ_π, δ_π^{nb} and δ_π^*). The $[Ru_3Cl_{12}]^{4-}$ complex has a $[Ru_3]^{8+}$ core and hence a valence-electron count of 16, leaving only the highest lying σ^* orbital empty. This gives a formal Ru-Ru formal bond order of $^1/_2$ consistent with the Ru-Ru bond length of 2.805(1) Å which is 0.08 Å longer than that of $[Ru_2Cl_9]^{3-}$ (2.725(3) Å), where the bond order is 1.0.[208]

The nature of the metal-metal interactions in the other known tri-ruthenium chains can also be understood using Figure 3.2. The $(PR_3)_2ClRu(RuCl_6)RuCl(PR_3)_2$ complexes (R = Et, tBu) reported in references 204-206[204–206] also have a 16-electron $[Ru_3]^{8+}$ core and Ru-Ru bond lengths in the region of ∼2.8 , and in this sense are extremely similar to the $[Cl_3Ru(RuCl_6)RuCl_3]^{4-}$. One-electron oxidation of these complexes generates the 15-electron $[Ru_3]^{9+}$ analogues $[(PR_3)_2ClRu(RuCl_6)RuCl(PR_3)_2]^+$,

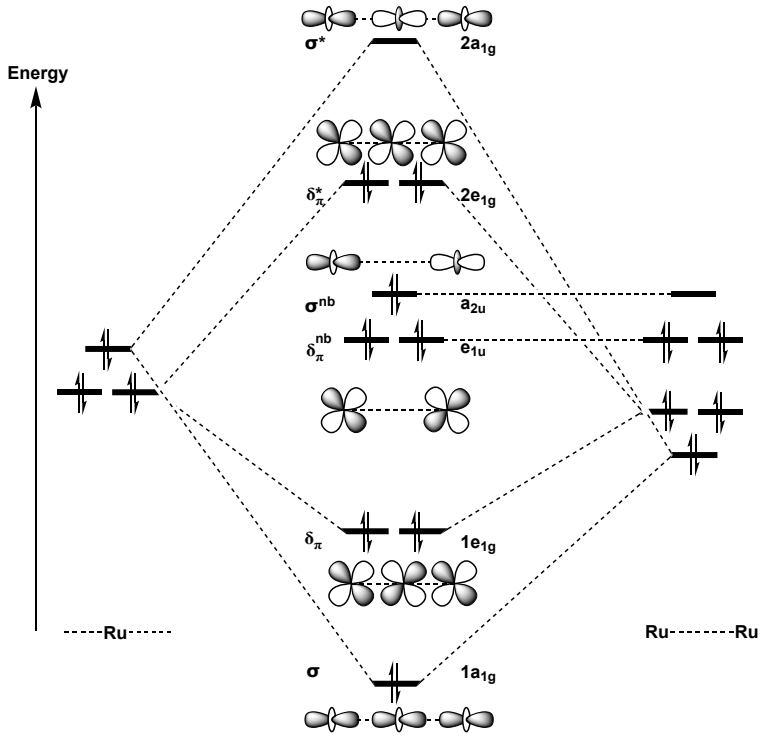

Figure 3.2: Molecular orbital array for $[Cl_3Ru(RuCl_6)RuCl_3]^{4-}$ (D_{3d} symmetry).

which have marginally longer Ru-Ru bond lengths due to the removal of an electron from the weakly antibonding δ_π^* orbital. The (p−cymene)Ru($RuCl_6$)Ru(p−cymene) system, in contrast, has an 18-electron $[Ru_3]^{6+}$ core, and the population of all nine bonding and antibonding molecular orbitals in Figure 3.2 eliminates the Ru-Ru bond entirely, giving a long Ru-Ru separation of 3.1975(8) Å. Finally, and of the most direct relevance to our interests in the present chapter is the $[(PEt_3)_3Ru(RuCl_6)Ru(PEt_3)_3]^+$ cation, described in reference.[206] This has a $[Ru_3]^{7+}$ core with 17 valence electrons, a formal Ru-Ru bond order of 1/4 and an intermediate Ru-Ru bond length of 3.083(1) Å. The structural data for the entire tri-ruthenium series, $[Ru_3]^{6+}$, $[Ru_3]^{7+}$, $[Ru_3]^{8+}$ and $[Ru_3]^{9+}$ can therefore be interpreted using the delocalized electronic structure model developed in Figure 3.2: one electron oxidation removes a weakly antibonding δ_π^* electron with minimal structural consequences while one-electron and two-electron reductions populate a Ru-Ru-Ru σ^* orbital, causing noticeable elongation of the bonds.

Our interest in these compounds comes from work conducted by our collaborators, Professors Graham Heath, and Alison Edwards and Dr Nicholas Perkins (Australian National University), who have reported the synthesis of a series of compounds with general formula $[(PEt_3)_3Ru(MCl_6)Ru(PEt_3)_3]^+$ including the M = Ru case previously reported by Cotton (1^+) but also the Rh and Ir analogues (2^+ and 3^+). The shift from group VIII to group IX metals necessarily increases the electron count by one, with potentially substantial changes in the nature of the metal-metal bonding. The synthetic methodology that gives access to these complexes involves taking the monometallic $[MCl_6]^{3-}$ fragments and capping them with a source of $[Ru(PR_3)_3]_2$. Detailed spectroelectrochemistry has allowed for characterization of these complexes in a range of oxidation states, offering a further opportunity to tune the strength of bonding between the metal ions. Thus although the 18-electron $[RuRhRu]^{7+}$ and $[RuIrRu]^{7+}$ cores of $[(PEt_3)_3Ru(RhCl_6)Ru(PEt_3)_3]^+$ and $[(PEt_3)_3Ru(IrCl_6)Ru(PEt_3)_3]^+$ complexes have no capacity to form metal-metal bonds, one- and two-electron oxidations give rise to species that are isoelectronic with 17-electron $[(PEt_3)_3Ru(RuCl_6)Ru(PEt_3)_3]^+$ and 16-electron $[(PEt_3)_3Ru(RuCl_6)Ru(PEt_3)_3]^{2+}$, respectively.

From an electronic perspective, there are various ways to look at these trimetallic complexes. Based on Figure 3.2 the nature of the metal-metal interactions in these tri-metallic chains depends on the relative energies of the t_{2g} orbitals on the MCl_6 and RuL_3 fragments. We can usefully consider two limiting scenarios: (a) the orbitals on MCl_6 are much higher in energy than those on the outer metals, in which case the orbitals on the RuL_3 will remain fully occupied. The L_3RuCl_3 unit then acts simply as a tripodal ligand. (b) the orbitals on the MCl_6 fragment are much lower than those on the outer metal, in which case charge transfer from the RuL_3 fragments will fill any vacancies in the MCl_6 manifold. In this scenario, the central MCl_6 fragment can be thought of as a bridging ligand, mediating the interaction between two paramagnetic Ru^{III} centers. There is, of course, a continuum of intermediate situations between

these two limits, where covalent bonding between the metals will be important.

The central question that we aim to address in this chapter is to which extent changes the identity of the metal in the $[MCl_6]^{z-}$ (M = Ru, Rh and Ir) fragment effects the communication between the terminal Ru ions $[(PEt_3)_3Ru(MCl_6)Ru(PEt_3)_3]^{z+}$. For this purpose, we compare and contrast the properties of the $[MCl_6]^{z-}$ monomer (where experimental data are available) with the $[(PEt_3)_3Ru(MCl_6)Ru(PEt_3)_3]^{z+}$ chains across a range of oxidation states, using both density functional theory and multi-configurational (CASSCF/PT2) methods. For the all-ruthenium system, the UV/Vis spectra of both $[RuCl_6]^{3-}$ and $[RuCl_6]^{2-}$ have been reported,[209,210] offering a direct comparison of 1^+ and 1^{2+}, respectively. In the limit that metal-metal interactions are insignificant, we would expect to see strong similarities between these compounds. Similarly for the Ir system, the known compounds $[IrCl_6]^{3-}$ and $[IrCl_6]^{2-}$ can be compared to $3^{+/2+}$.[211,212]

The work described in this chapter has been published in Chemistry A European Journal, 2018, 24, 5309-4318.

3.2 Computational Methodologies

All DFT calculations in this chapter were done with the Amsterdam Density Functional package (DFT2016.105).[213–215] In this study, we used two types of functionals, the gradient-corrected BLYP functional of Becke, Lee, Yang, and Parr[216,217] and its hybrid B3LYP,[218,219] in both cases with relativistic scalar corrections (ZORA). A triple-ζ Slater-type basis set extended with a single polarization function (TZP) was used to describe the transition metals while double-ζ Slater-type basis sets extended with a single polarization function (DZP) were used for the main-group atoms. The frozen core approximation was used to treat the electrons in orbitals up to and including 4d on Ir, 3d on Ru, 2p on P and Cl, and 1s on C. For the calculations with PMe_3 ligands, Grimme's corrections for dispersion were adopted.[220] Symmetry break-

ing was allowed by reducing the overall symmetry from D_{3d} to C_{3v} and polarizing the starting potential such that an excess of spin-α and spin-β density was placed on opposite ruthenium centers (using Modifystartpotential keyword in ADF). This allows the electrons to localize in a biradical state if this is more stable than the delocalized alternative, but it does not force them to do so: a spin polarized initial guess can always converge on the delocalized solution if this is more stable. The gradient algorithm of Versluis and Ziegler was used to optimize all structures.[221] Time-dependent DFT[222] was used to calculate UV-Visible spectra with Tamm-Dancoff approximation (TDA)[223] and CH_2Cl_2 as a solvent; B3LYP and M06-L[224,225] functionals with relativistic scalar corrections (ZORA) were used in this method. The EPR spectra were computed by using self-consistent spin-orbit coupling (SCSO) approach.[226,227]

Single point CASSCF/PT2 calculations were done using the MOLCAS 8.0 package.[228] The orbitals are expanded in a basis of atomic natural orbitals optimized for relativistic corrections and core correlation (ANO-RCC).[229] The large primitive set of functions is contracted to [7s6p4d2f1g] for Ru and Rh, [4s3p1d] for P and Cl, and [1s] for H. The Cholesky decomposition with threshold of 1.0 e^{-8} was used for the two-electron integrals.[230]

3.3 Results and Discussion

Structural Data: Comparison of X-ray Experiments to DFT

The structures of 1^+, 2^+, and 3^+ have all been reported in the PhD thesis of Dr Nicholas Perkins.[231] All three adopt the face-shared octahedral architecture shown in Figure 3.1, with metal-metal bond lengths of 3.083(1) Å, 3.1690(3) Å and 3.2332(3) Å in 1^+, 2^+ and 3^+, respectively. The first of these is very similar to Cotton's previous study of the same compound. The long distances in 2^+ and 3^+ are consistent with the absence of any direct metal-metal bonding in these 18-electron species, and they are very similar to the value of 3.1975(8) Å in the 18-electron

(p−cymene)$RuCl_3RuCl_3$Ru(p−cymene) system.[207] For the electronic structure investigations, we have applied two quite different computational methodologies, single-determinant DFT and multi-configurational CASSCF/PT2. At the DFT level, we have considered two quite different functionals BLYP and B3LYP, the latter having 20% Hartree-Fock exchange. Our previous studies have shown that these two functionals often provide qualitatively different pictures of metal-metal interactions.[232] We start our discussion by reproducing the X-ray data of 1^+, 2^+ and 3^+ to validate both the computational methodologies and the simplifications used in our model systems.

The clean separation between σ and δ_π manifolds shown in Figure 3.2 that is possible only in a rigorously D_{3d}-symmetric greatly simplifies the electronic structure analysis and also allows us to converge to specific configurations. It is, however, impossible to impose a D_{3d}-symmetric conformation on $[(PEt_3)_3Ru(RuCl_6)Ru(PEt_3)_3]^+$ without introducing unreasonable steric clashes between the Et groups substituted on phosphine ions in the crystal structure. If, alternatively, we do not impose any symmetry, free rotation about all P-C and C-C bonds generates a very large number of conformers, each of which may correspond to a local minimum. One way to tackle this problem is to replace the bulky Et groups by smaller groups, Me or H, giving the simplified models $[(PMe_3)_3Ru(MCl_6)Ru(PMe_3)_3]$ and $[(PH_3)_3Ru(MCl_6)Ru(PH_3)_3]$. These simplifications are, at least potentially extreme, so in order to explore its impact on the structural parameters, we have optimized the geometries of 1^+, 2^+ and 3^+ with different substituents on the phosphine ligands and then compared them to X-ray data. Table 3.1 shows optimized structural parameters of 1^+, 2^+ and 3^+ with different substitutions on the phosphine ligands, alongside the crystallographic data. The data suggests that the model ligands do appear to capture the majority of the inductive and steric effects of the alkyl group: the Ru-Ru separation of 3.083(1) Å in 1^+ are reproduced to within 0.03 Å with both PH_3 and PMe_3 ligands and with BLYP and B3LYP functionals. The Mulliken spin densities of 1^+ with PH_3 ligands

are also very similar to those with the PMe_3 model. The Ru-M distances of 2^+ and 3^+ are slightly less accurate, perhaps reflecting the fact that there is no direct Ru-M bonding in these 18-electon systems, as a result which the potential energy surface is very flat. There is little difference between the two functionals, at least at the 1^+ oxidation level. The close correspondence between the structural parameters of the different substituents suggests that the extreme simplification of the phosphine ligands does not compromise the description of the metal-metal bonding to any great extent. As a result, we are justified in using the highly simplified model ligand PH_3 in the following sections, taking advantage of the ability to impose D_{3d} symmetry with all of its advantages.

Table 3.1: Comparison of the optimized structure parameters of 1^+, 2^+ and 3^+ with different substitutions on the phosphine ligands (distance in Å). ρ is the Mulliken spin density.

		Ru-M	Ru-Cl	Ru-P	M-Cl	ρ(Ru)	ρ(M)
			1^+				
PM_3	BLYP	3.10	2.57	2.29	2.42	0.11	0.68
	B3LYP	3.09	2.56	2.30	2.41	0.06	0.79
PH_3	BLYP	3.13	2.54	2.31	2.45	0.09	0.73
	B3LYP	3.10	2.52	2.31	2.43	0.04	0.83
PEt_3	X-ray	3.083(1)	2.50	2.31	2.36		
			2^+				
PM_3	BLYP	3.23	2.58	2.28	2.40		
	B3LYP	3.19	2.56	2.29	2.39		
PH_3	BLYP	3.24	2.54	2.30	2.43		
	B3LYP	3.19	2.53	2.31	2.41		
PEt_3	X-ray	3.1690(3)	2.52	2.29	2.34		
			3^+				
PM_3	BLYP	3.27	2.59	2.28	2.41		
	B3LYP	3.22	2.57	2.28	2.40		
PH_3	BLYP	3.27	2.55	2.30	2.43		
	B3LYP	3.21	2.53	2.30	2.42		
PEt_3	X-ray	3.2873(3)	2.54	2.29	2.35		

Electrochemistry

The electrochemistry of compounds 1, 2 and 3, reported in the PhD thesis of Dr Nicholas Perkins,[231] is summarized in Table 3.2. We emphasise that X-ray data are not available for any of these electro-generated species. For 2 and 3, the absence of a reduction wave is consistent with the full occupation of the molecular orbitals in Figure 3.2, which gives, unambiguously, a $Ru^{II}(Rh/Ir)^{III}Ru^{II}$ formulation for the oxidation states. The first and second oxidation processes could, in principle, be localized on the central metal ion or on the terminal ruthenium centers. The high potential of the $Rh^{IV/III}$ couple in $[RhCl_6]^{2-/3-}$ suggests that the latter is more likely in 2.[233] Moreover, the mean of the two oxidation waves in $[(PEt_3)_3RuCl_3Ru(PEt_3)_3]^+$,[234] where the redox events are unambiguously $Ru^{II/III}$ couples, is 1.40 eV, only slightly lower than in 2 (1.53 eV). The separation between the two oxidations waves of 0.17 V in 2 is smaller than in the bimetallic, $[(PEt_3)_3RuCl_3Ru(PEt_3)_3]^+$ (0.17 V) suggesting a weaker interaction consistent with the increased separation between the redox-active centers.[235] For compound 3, the average value of the two oxidation waves of 1.51 V is similar to those in 2 but the lower value for $E_{1/2}$(ox1) of 1.34 V suggests a greater participation of Ir in the frontier orbitals.

Table 3.2: Oxidation and reduction potentials for 1, 2 and 3 (all examined in the 1+ state) vs. Ag/AgCl. (Fc/Fc^+ occurs at 0.55 V).

	$E_{1/2}$(red)[V]	$E_{1/2}$(ox1)[V]	$E_{1/2}$(ox1)[V]
RuRuRu (1)	-0.14	+1.08	+1.78
RuRhRu (2)		+1.45	+1.62
RuIrRu (3)		+1.34	+1.67

For compound 1^+, the assignment of oxidation states is less obvious, simply because all three metals are the same. The fact that the central Ru is surrounded by six π-donor Cl ligands suggests a $Ru^{II}Ru^{III}Ru^{II}$ formulation, but the unoccupied σ^* orbital is clearly delocalized over all three Ru centres. The limit of full delocalization would

correspond to $Ru^{2.33+}Ru^{2.33+}Ru^{2.33+}$. The reduction wave at -0.14 V can be safely assigned to a $Ru^{II/III}$ couple (localized or delocalized) but the shift of 1.39 V relative to $[RuCl_6]^{2-/3-}$ is indicative of a substantial effect from the two $Ru(PEt_3)_3$. The first oxidation process leave us with 16 valence electrons, most likely in a $Ru^{II}Ru^{III}Ru^{III}$ $\leftrightarrow$ $Ru^{III}Ru^{III}Ru^{II}$ arrangement. The alternative formulation as $Ru^{II}Ru^{IV}Ru^{II}$ with oxidation states differing by two seems unlikely, but cannot be ruled out given the different coordination envirnoments of the central and terminal metals. Finally, the second oxidation could give rise to $Ru^{III}Ru^{III}Ru^{III}$, $Ru^{III}Ru^{IV}Ru^{II}$ or $Ru^{II}Ru^{V}Ru^{II}$ arrangements. The much greater separation between the two oxidation waves for 1^+ compared to either 2^+ or 3^+ suggests suggests that the oxidation events are not simply localized on the terminal metals in the former.

3.3.1 Electronic Structure: the DFT Picture

Electronic Structure of the 17-electron Systems

The $[RuRuRu]^{7+}$ core of the isolated all-ruthenium species 1^+ has 17 valence electrons, as do the electro-generated Rh and Ir analogues, 2^{2+} and 3^{2+}. The Kohn-Sham diagram shown in Figure 3.3 shows that the d_{z^2} orbital of a $[RuCl_6]^{3-}$ fragment interacts with linear combinations on the terminal atoms to form the $1a_{1g}$ and $2a_{1g}$ orbitals (σ and σ^* character, respectively) while the out-of-phase combination of d_{z^2} orbitals on the terminal atoms generates the a_{2u} orbital, which is non-bonding with respect to the central metal atom. The 17 valence electrons are distributed over the 9 linear combinations of metal d orbitals, leaving only the $2a_{1g}$ (σ^*) orbital singly occupied in a $^2A_{1g}$, ground state. The Ru-Ru bond lengths are 3.13 Å and 3.10 Å with BLYP and B3LYP functionals, respectively. The same two functionals were used to investigate the stabilities of other possible ground states, including the $^2E_{1g}$ ($2a_{1g}^2 1e_{1g}^3 a_{2u}^2$) and $^2A_{2u}$ ($2a_{1g}^2 1e_{1g}^4 a_{2u}^1$) states arising from promotion of electrons from the $1e_{1g}$ and a_{2u} orbitals into $2a_{1g}$ (Figure 3.3 (right)). Our calculations show that

the $^2E_{1g}$ state lies 0.14 eV and 0.64 eV above the $^2A_{1g}$ state with BLYP and B3LYP functionals, respectively while the $^2A_{2u}$ state is located at +1.44 eV and +1.73 eV with BLYP and B3LYP, respectively. The Mulliken spin density on the central Ru atom is 0.73/0.83 in the $^2A_{1g}$ ground state and 0.09/0.04 on the terminal ruthenium atoms (BLYP/B3LYP), confirming that the unpaired electron is almost entirely localized on the central ruthenium atom (the limiting values of complete localization are 1.0 and 0.0 on the central and outer ruthenium centers, respectively). This implies a $Ru^{II}Ru^{III}Ru^{II}$ ($d^6d^5d^6$) oxidation state distribution, although the iso-surface plot of the $2a_{1g}$ orbital (Figure 3.3 (right)) suggests that there is a significant contribution of the terminal ruthenium ions in the SOMO, giving a three-center three electron bond.

Figure 3.3 compares the UV-Vis spectrum of 1^+ with that of the isolated $[RuCl_6]^{3-}$ molecules. The optimized geometry (BLYP) and Kohn-Sham orbital diagram are also shown. The UV-Vis spectrum of the $[RuCl_6]^{3-}$ molecule in Figure 3.3 (left) shows two bands, both located above 20000 cm^{-1}, at 28200 cm^{-1} and 31000 cm^{-1}. TD-DFT calculations performed with the M06-L functional also predict two intense bands, at 23724 cm^{-1} (ν_1) and 33066 cm^{-1} (ν_2), corresponding to Cl $\rightarrow$ Ru (t_{2g}) and Cl $\rightarrow$ Ru (e_g) transitions, respectively. In a previous study on $[RuCl_6]^{3-}$ using SCF-X_α both transitions were assigned to charge transfer into t_{2g}: the difference in performance of the two methods probably relates to the absence of correlation effects in the SCF-X_α method.[236] For 1^+, the UV-Vis spectra has three intense bands at 11340 cm^{-1} (ε = 5920 $dm^3mol^{-1}cm^{-1}$), 25830 cm^{-1} (ε = 4870 $dm^3mol^{-1}cm^{-1}$) and 32010 cm^{-1} (ε = 3270 $dm^3mol^{-1}cm^{-1}$). The latter two are in a similar region to those in the $[RuCl_6]^{3-}$ fragment, but the intense low-energy band is clearly associated with the tri-metallic chain. TD-DFT calculations predict an intense band at 12610 cm^{-1} (ν_1) (compared to 11340 cm^{-1} in the actual spectrum), corresponding to a dipole-allowed $a_{2u} \rightarrow 2a_{1g}$ excitation ($\sigma^{nb} \rightarrow \sigma^*$). Given the localization of the two orbitals on the outer and inner Ru centres, respectively, this band is best characterised as a metal

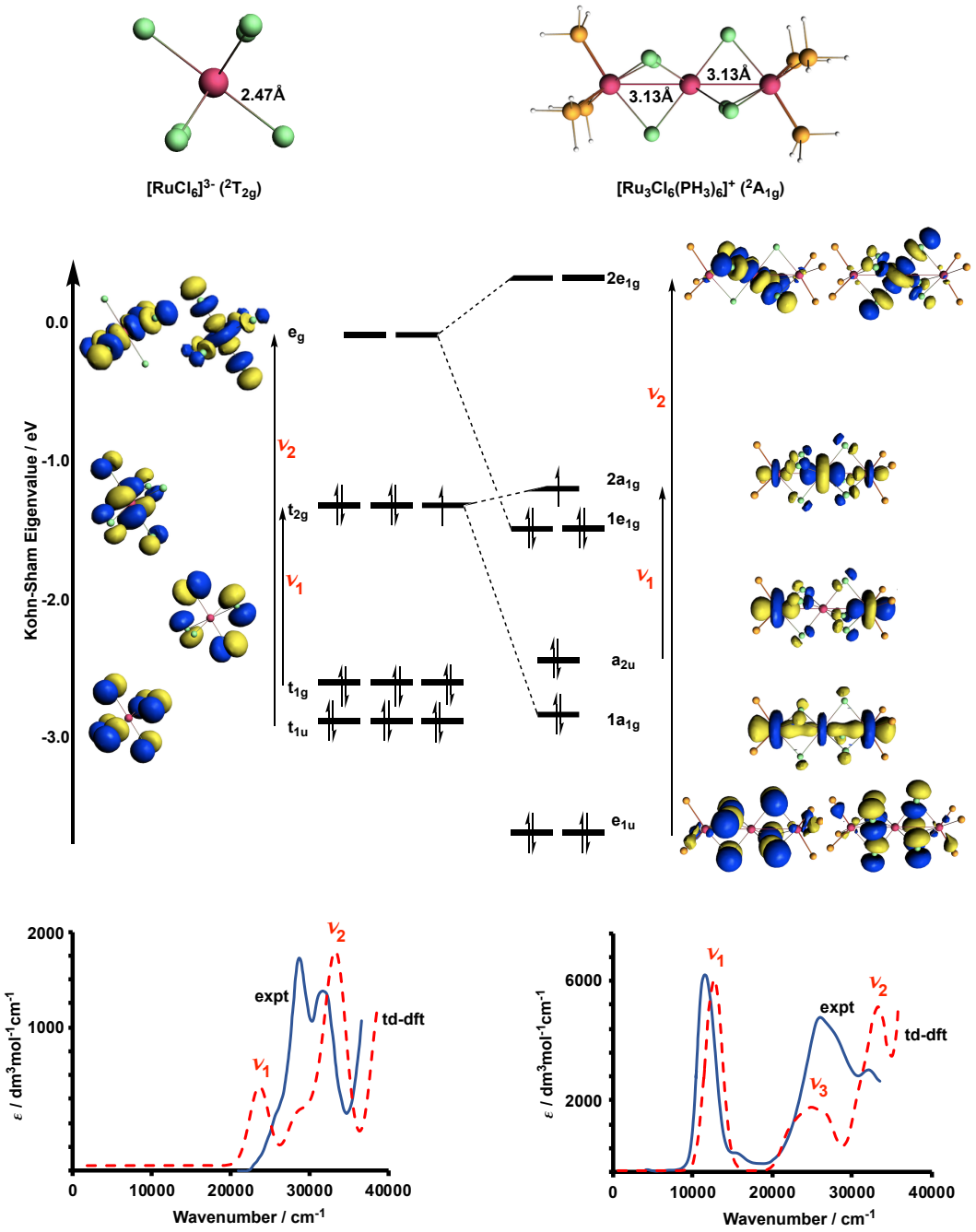

Figure 3.3: Optimized geometry (BLYP), Kohn-Sham orbital manifold and UV-Vis spectra of $[RuCl_6]^{3-}$ (left) and 1^+ (right). The energy scale corresponds to the orbitals of 1^+. The experimental spectrum is shown in blue and the TD-DFT-M06-L in dashed red.

to metal charge transfer. The remaining two bands have transition energy higher than 20000 cm^{-1} similar to those in the $[RuCl_6]^{3-}$. The second band at 32010 cm^{-1} (ν_2) (TD-DFT-M06-L = 33100 cm^{-1}) corresponds to a Cl $\rightarrow$ Ru ($e_{1u} \rightarrow 2e_{1g}$), and is similar in character to the Cl $\rightarrow$ Ru (e_g) (ν_2) transition in $[RuCl_6]^{3-}$. There is extensive literature showing that the position of charge transfer transitions as well as their intensities are sensitive to the applied exchange-correlation functionals. To illustrate this point, TD-DFT-B3LYP shifts the first band (ν_1) by more than 2300 cm^{-1} to 14950 cm^{-1}. The second band is located at 33100 cm^{-1} by M06-L and 34550 cm^{-1} by B3LYP, representing a blue shift of $\sim$1500 cm^{-1}. However, with all different functionals we found an intense metal-metal charge transfer band below 20000 cm^{-1} which is entirely absent in the $[RuCl_6]^{3-}$ fragment, so the assignment of this feature in the spectrum is not in doubt.

In the Rh and Ir analogues, 2^{2+} and 3^{2+}, the ground state also has $^2A_{1g}$ symmetry with Ru-M bond lengths of $\sim$3.10 Å with BLYP and $\sim$3.03 Å with B3LYP which are only slightly shorter than those in all-ruthenium system (3.13 Å /3.10 Å with BLYP/B3LYP). This suggests that electronic structure is qualitatively similar cross this series, but the Mulliken spin density, however, shows a rather different picture of the oxidation state pattern. The spin densities of 0.30/0.29 and 0.33/0.32 on Rh and Ru in 2^{2+} (BLYP/B3LYP), respectively, imply that the unpaired electron are delocalized more equally over all three metals centers. A $d^6d^5d^6$ configuration similar to that found in 1^+ would generate limiting spin densities of 1.0 and 0.0 on Rh and Ru, respectively, but this would imply a rather unrealistic $Ru^{2+}Rh^{4+}Ru^{2+}$ pattern. Alternatively, if all three Rh-t_{2g} orbitals become fully occupied, the oxidation state pattern would be $Ru^{2.5+}Rh^{3+}Ru^{2.5+}$ ($d^{5.5}d^6d^{5.5}$) with spin densities of 0 and 0.5 on Rh and Ru, respectively. The computed values of 0.30 and 0.33 on Rh and Ru in 2^{2+} are intermediate between these two limits. The spin density distribution in Ir case, 3^{2+}, is pushed somewhat towards the $d^6d^5d^6$ limit with somewhat larger

Mulliken spin density on Ir (0.38/0.42 with BLYP/B3LYP) compared to 0.27/0.23 with BLYP/B3LYP on the terminal ruthenium ions. It is perhaps counterintuitive that the hetero-metallic RuRhRu system appears to more delocalized than its homo-metallic RuRuRu counterpart, but it is important to remember that the energies of the orbitals are determined not just by the identity of the metal but also by its coordination environment. The presence of six π-donor chloride ligands around the central metal therefore offsets the intrinsically greater electronegativity of Rh vs Ru, resulting in atom-centered d orbitals of very similar energies on all three metals.

The UV-Vis spectra of the $[IrCl_6]^{2-}$ and 3^{2+} are compared in Figure 3.4, along with the optimized structure (BLYP functional) and the Kohn-Sham molecular orbitals. The spectrum of the $[IrCl_6]^{2-}$ has two bands at 20000 cm^{-1} and 24000 cm^{-1}, while TD-DFT with M06-L predicts two bands at 16871 cm^{-1} (ν_1) and 32487 cm^{-1} (ν_2) corresponding to charge transfer from the chlorine to metal-based orbitals, Cl $\rightarrow$ Ru (t_{2g}) and Cl $\rightarrow$ Ru (e_g), respectively. Again, previous SCF-X_α studies suggested that both bands correspond to Cl $\rightarrow$ Ru (t_{2g}) transitions.[236] The experimental UV-Vis spectrum of the 3^{2+} shows two bands below 20000 cm^{-1}, one at 5730 cm^{-1} (ε = 3070 $dm^3mol^{-1}cm^{-1}$) and the other at 13800 cm^{-1} (ε = 2150 $dm^3mol^{-1}cm^{-1}$). TD-DFT-M06-L predicts bands at 12307 cm^{-1} (ν_1) and 20990 cm^{-1} (ν_2), both corresponding to metal to metal charge transfer. The first, the $a_{2u} \rightarrow 2a_{1g}$ excitation ($\sigma^{nb} \rightarrow \sigma^*$), is entirely within the t_{2g} manifold while the $2e_{1u} \rightarrow 1e_{1g}$ excitation ($\delta_\pi^{nb} \rightarrow \delta_\pi^{vir}$), involves promotion of electrons across the t_{2g}-e_g gap. The Cl $\rightarrow$ Ru charge transfer is predicted to start at 34730 cm^{-1} (ν_3) consistent with the band at 30440 cm^{-1} (ε = 3910 $dm^3mol^{-1}cm^{-1}$) in the experimental spectra. The switch from Ru (1^+) to Ir (3^{2+}) in the central position also results in a marginal contraction of the manifold of states arising from one-electron promotions to the $2a_{1g}$ orbital, and the $\sigma^{nb} \rightarrow \sigma^*$ transition in 3^{2+} is computed at 12307 cm^{-1} (ν_1) (TD-DFT, M06-L) compared to 12610 cm^{-1} (ν_1) in 1^+. Unlike the spectrum of 1^+, where the TD-DFT calculations were very

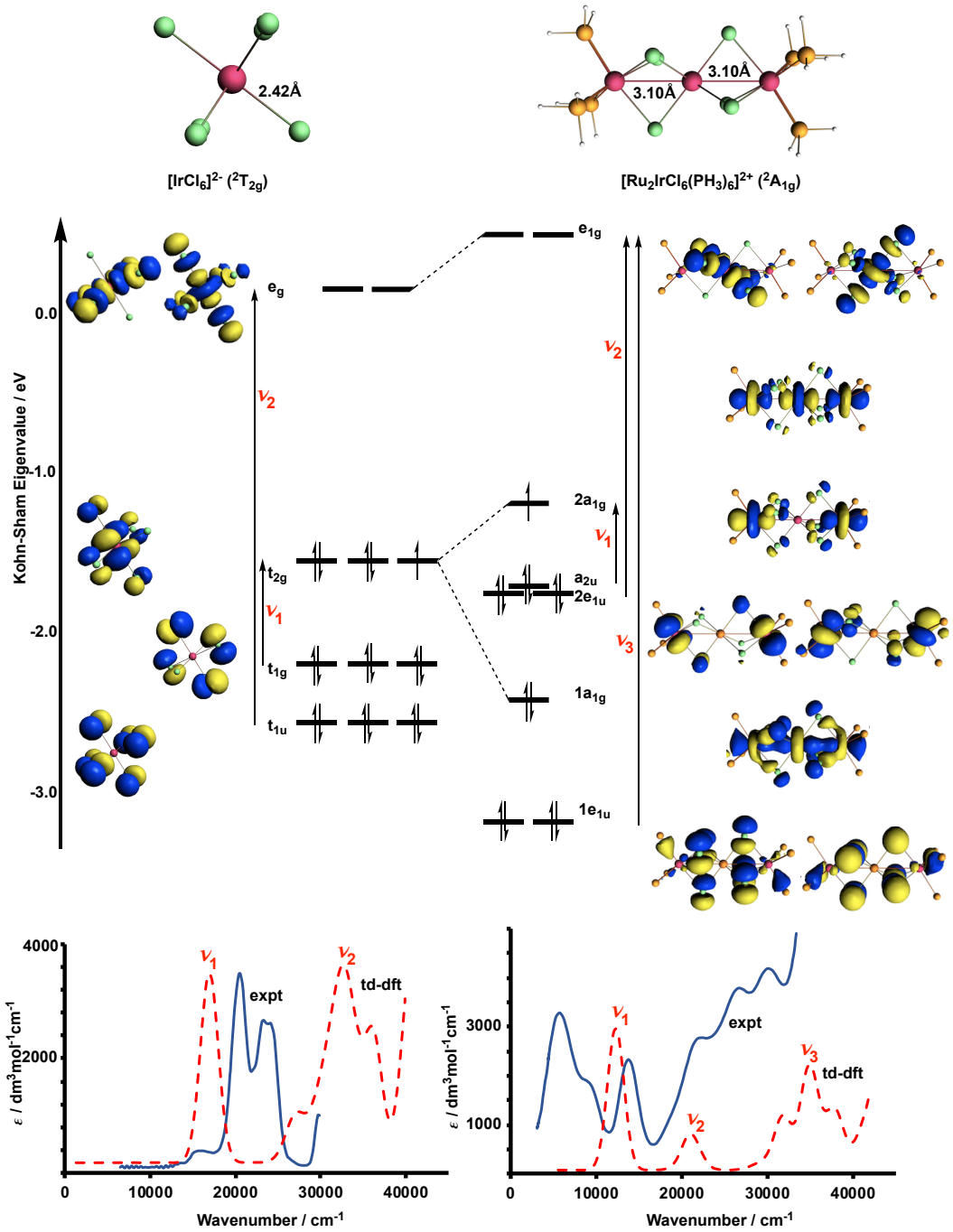

Figure 3.4: Optimized geometry (BLYP), Kohn-Sham orbital manifold and UV-Vis spectra of $[IrCl_6]^{2-}$ (left) and 3^{2+} (right). The energy scale corresponds to the orbitals of 3^{2+}. The experimental spectrum is shown in blue and the TD-DFT-M06-L in dashed red.

similar to the experimental spectrum, there is a substantial discrepancy between the computed and measured spectra of 3^{2+}. Most obviously, the lowest frequency band is much higher in the TD-DFT calculations. This may be a consequence of spin-orbit coupling, which is not included in the calculation. Alternatively, the simplification of the PEt_3 ligands with PH_3 may stabilize the orbitals on the terminal Ru centers, pushing the Ru $\rightarrow$ Ir charge transfer to higher energies. Nevertheless, it is clear that the low-energy bands reflect transitions within the t_{2g} manifold of orbitals.

Computed EPR Spectra of 1^+

The EPR spectrum data of the $^2A_{1g}$ ground state of 1^+ system has been computed using the self-consistent spin-orbit coupling approach using both BLYP and B3LYP functionals. The computed g-tensor values of 1^+ are $g_{x,y}(g_\perp)/g_z(g_\parallel)$ of 2.33/1.90 and 2.48/1.87 with BLYP and B3LYP, respectively, comparing to the experimental values of 2.34/$\sim$1.40. The principal axis of the g-tensor is aligned along the Ru-Ru-Ru chain and the computed principal values are consistent with the experiment in predicting an axial spectrum with (g_{zz}<g_e<g_{xx},g_{yy}).

In a rhombic molecule the three principal values g_x, g_y and g_z differ from each other but if the molecule has axial symmetry two cases can be distinguished: $g_x = g_y = g_\perp$ ($\perp$ perpendicular to the magnetic field) and $g_z = g_\parallel$ ($\parallel$ parallel to the magnetic field). If the symmetry is cubic all three principal values are equal. In cases where the orbital contribution to the g value is completely quenched at zeroth order, g is isotropic and equal to free electron value $g_e = 2.0023$. However, in cases where residual orbital angular momentum remains, there is a deviation from the free electron value due to spin orbit coupling which mixes excited states into ground state. When the ground state is nondegenerate, the deviation from the free electron value can be calculated with second order perturbation theory using the following equation.[237,238]

$$g_i = g_e + 2\lambda \sum_{n=1,2,..} \left(\frac{\langle g|\hat{L}|n\rangle\langle n|\hat{L}|g\rangle}{E_g - E_n} \right) \tag{3.1}$$

where i stands for x, y, or z, λ is a spin orbit coupling constant, E_g and E_n are the energies of ground and excited states, respectively, and $\hat{L}$ is orbital angular momentum. Parameterisation of the matrix elements gives the general formula:

$$g_i = 2.0023 \pm \frac{k\lambda}{E_g - E_n} \tag{3.2}$$

For transition metal ions with more than a half-filled d shell the spin orbit coupling parameter is negative such that g_z is larger than g_x and g_y which in turn are larger than g_e. In contrast, if the d shell is less than half filled the spin orbit parameter is positive. k defines the degree of orbital mixing and, in systems with a single metal centre, can be found by using the so-called magic pentagon (Figure 3.5). So for example, the d_{xz} and d_{yz} orbitals are mixed by the z component of the magnetic field $\hat{L}_z$, the product $\langle xz|\hat{L}_z|yz\rangle\langle yz|\hat{L}_z|xz\rangle$ being equal to 1.

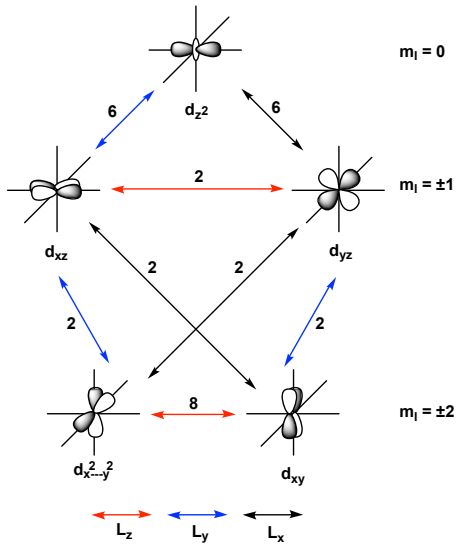

Figure 3.5: Magic pentagon diagram.

The deviation of g-tensor values from the free electron value (2.0023) can be understood in term of the MO diagram in Figure 3.3 (right). For the components of

the magnetic field aligned along x and y, the dominant contribution comes from the matrix element $\langle 1e_{1g}|\hat{L}_{x/y})|2a_{1g}\rangle$, the energy difference between those orbitals being 0.29 eV: it is apparent on a qualitative level that rotating the components of on orbital about the x-axes or the y-axes maps one onto the other. In contrast, the dominant contribution when the magnetic field is aligned along z is $\langle 1e_{1g}|\hat{L}_{x/y}|2e_{1g}\rangle$, where the energy difference is 1.81 eV. The contribution of the first matrix element is much bigger than the contribution from the second one but the impact on the g-tensor is dominated by the denominator, specifically the energy gap, which is much smaller when the vacant orbital is the SOMO, $2a_{1g}$. The end results is that the components perpendicular to the Ru-Ru-Ru chain deviate much more strongly from the free electron value than that parallel to it.

Electronic Structure at the 18-electron Level

The isolated forms of 2^+ and 3^+ both have 18 valence electrons, and are isoelectronic with the one-electron-reduced 1^0. In all three cases the $2a_{1g}$ orbital is now filled (Figure 3.6 (right)) giving formal bond order of zero consistent with longer Ru-M separation of 3.1690(3) Å and 3.2873(3) Å measured by X-ray crystallography for 2^+ and 3^+, respectively. The computed values with B3LYP are 3.19 Å and 3.21 Å for 2^+ and 3^+, respectively, substantially longer than the values of 3.10 Å and 3.04 Å for 17-electron 2^{2+} and 3^{2+}, respectively. Accordingly, the UV-Vis spectrum of 3^+ is featureless below 20000 cm^{-1}, and the TD-DFT-M06-L calculation predicts a first intense peak at 37316 cm^{-1} (ν_1) due to Cl $\rightarrow$ M charge transfer ($1e_{1u} \rightarrow e_{1g}$). This is also consistent with UV-Vis spectra of the $[IrCl_6]^{3-}$,[239] which has a single band at 23000 cm^{-1} (ν_1) due to the charge transfer ($t_{1u} \rightarrow e_g$) and less intense 26719 cm^{-1}, consistent with the experimental spectrum has two bands at 24100 cm^{-1} and 28100 cm^{-1}.

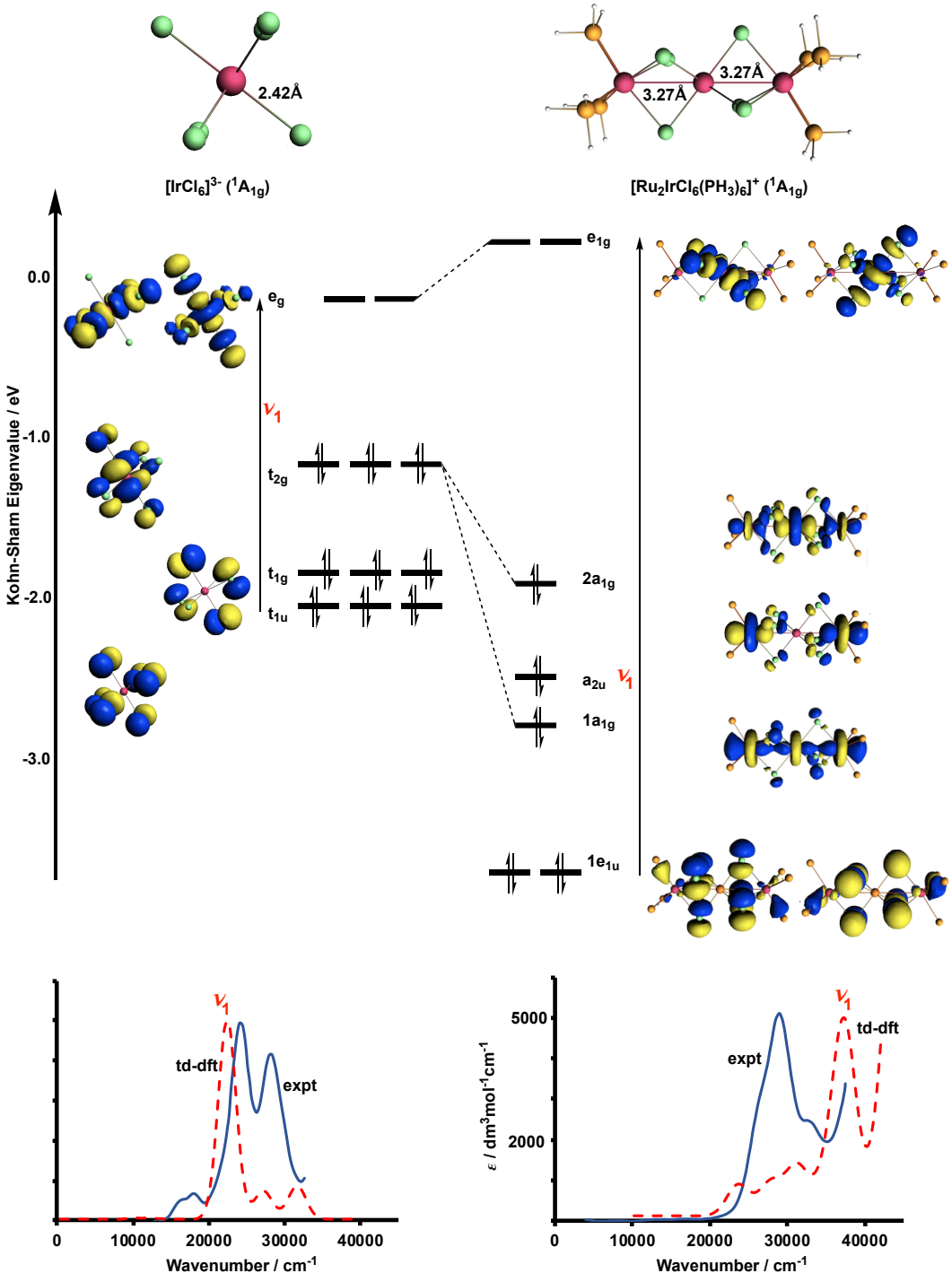

Figure 3.6: Optimized geometry (BLYP), Kohn-Sham orbital manifold and UV-Vis spectra of $[IrCl_6]^{3-}$ (left) and 3^+ (right). The energy scale corresponds to the orbitals of 3^+. The experimental spectrum is shown in blue and the TD-DFT-M06-L in dashed red.

Electronic Structure of the 16-electron Systems

The electro-generated cations 1^{2+}, 2^{3+} and 3^{3+} all share a common 16 valence-electron count, and the increased number of vacancies in the t_{2g} manifold leads to a richer spectrum of low-lying states. As a result, and unlike the 17- and 18-electron cases, the identity of the ground state is not clear cut, and we seek to use the comparison between experimental and predicted (TD-DFT) spectra to identify the most likely candidates in each case. Figure 3.7 shows a comparison of the UV-Vis spectra of $[RuCl_6]^{2-}$ and 1^{2+}, along with optimized geometries and Kohn-Sham molecular orbitals. The point of reference is now the UV-Vis spectrum of $[RuCl_6]^{2-}$, which has two bands at 18168 cm^{-1} (ν_1) and 24708 cm^{-1} (ν_1): TD-DFT-M06-L suggests that these are assigned Cl $\rightarrow$ Ru charge transfer, $t_{1g} \rightarrow t_{2g}$ and $t_{1u} \rightarrow e_g$, respectively. In 1^{2+}, the B3LYP functional predicts a closed-shell singlet ($^1A_{1g}$ state) ground-state with short Ru-Ru separations of 2.87 Å, similar to the values reported for $[Ru_3Cl_{12}]^{4-}$ by Bino and Cotton.[199] The $\sigma^{nb} \rightarrow \sigma^*$ transition energy of 16496 cm^{-1} (ν_1) estimated using TD-DFT-M06-L is the first intense transition, and therefore the most likely candidate for the prominent band at 9950 cm^{-1} (ε = 10860 $dm^3mol^{-1}cm^{-1}$) in the experimental spectrum. The deviation between experiment and theory is, however, large (6500 cm^{-1}), and noticeably larger than in 1^+ where the TD-DFT value is within 1200 cm^{-1} of it is experimental value (Figure 3.3 (right)). One explanation for this deviation is the possible multiconfigurational nature of the singlet excited state in 1^{2+}. We will explore this issue in the context of CASSCF calculations in the following section. The second band at 20000 cm^{-1} (ν_2) (expt. = 21540 cm^{-1} (ε = 3010 $dm^3mol^{-1}cm^{-1}$) corresponds to a Cl $\rightarrow$ Ru charge transfer, similar to that in $[RuCl_6]^{2-}$. In contrast, the ground state at the BLYP level is a $^3E_{1g}$ ($2a_{1g}^1\ 2e_{1g}^3$) state, where a single electron has been promoted from the $1e_{1g}$ orbital to $2a_{1g}$, although the $^1A_{1g}$ state lies only 0.05 eV higher in energy. The single occupation of the Ru-Ru-Ru σ^* orbital, $2a_{1g}$, leads to longer Ru-Ru separations of 3.12 Å.

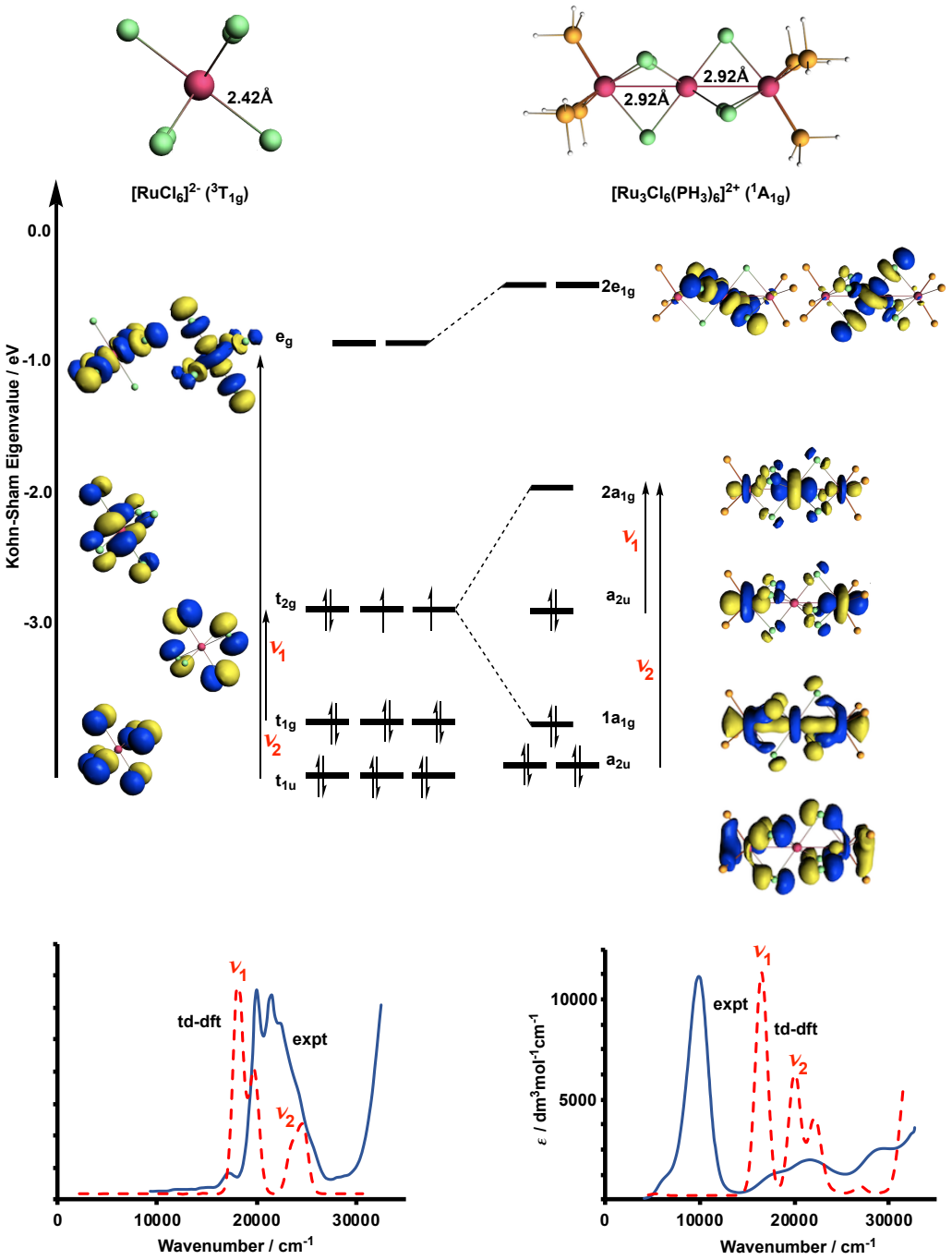

Figure 3.7: Optimized geometry (BLYP), Kohn-Sham orbital manifold and UV-Vis spectra of $[RuCl_6]^{2-}$ (left) and 1^{2+} (right). The energy scale corresponds to the orbitals of 1^{2+}. The experimental spectrum is shown in blue and the TD-DFT-M06-L in dashed red.

In 1^+ (17-electron), we noted that the the inclusion of the exact Hartree-Fock exchange in the B3LYP functional destabilizes the $^2E_{1g}$ ($2a_{1g}^2 2e_{1g}^3$) state relative to $^2A_{2u}$ ($2a_{1g}^2 2e_{1g}^3 a_{2u}^1$), and in general, we find that the B3LYP is systematically biased towards configurations where vacancies reside in orbitals with σ symmetry ($1/2a_{1g}$, a_{2u}) rather than δ_π ($1/2e_{1g}$, e_{1u}). The reasons for this are not clear, but it not exclusive to polymetallic chains: even in the C_{3v}-symmetric monometallic $(PH_3)_3RuCl_3$ fragment (d^5), the $^2A_1$ state lies below ^2E by 0.43 eV with B3LYP but only 0.05 eV with BLYP. Whatever the reason, it is clear that the two popular functionals, BLYP and B3LYP, offer up very different pictures of the ground-state electronic structure.

For the isoelectronic system, 2^{3+}, the DFT shows a very different picture of the metal-metal bonding. The strongly bonded $^1A_{1g}$ state is now not the ground state for either functional, although the Ru-Ru separations of 2.94 Å and 2.87 Å with BLYP and B3LYP, respectively, are not dissimilar to those in 1^{2+}. Instead, we find a triplet state, $^3A_{2u}$, with a $2a_{1g}^1 2e_{1g}^4 2e_{1u}^4 a_{2u}^1$ configuration, to be more stable. The relatively long Ru-Rh separations of 3.04 Å suggest only weak meta-metal bonding, and the spin densities (0.26/0.08 on Rh and 0.78/0.93 on Ru with BLYP/B3LYP) indicate that the electron is localized on the terminal ruthenium centers. We have also identified a broken-symmetry biradical state, BS(σ,σ), which is the antiferromagnetic counterpart of $^3A_{2u}$, where the electrons are localized rigorously on the two terminal Ru centres (Mulliken spin density of 0.00 on Rh and $\pm$0.94 on Ru with B3LYP) which lies just 0.02/0.01 eV above the triplet with BLYP/B3LYP. These results suggested that the communication between the two Ru centers is weak in 2^{3+}.

For the Ir analogue, 3^{3+}, the BS(σ,σ) state with Mulliken spin density of 0.00 on Ir and $\pm$0.80 on terminal Ru has been located with B3LYP and has a rather Ru-Ir separation of 3.02 Å, quite similar to the Rh-Ru distance in 2^{3+}. With the BLYP functional, however, all attempts to converge the broken-symmetry state reverted to a state have same energy to the closed-shell singlet, $^1A_{1g}$, with a short Ru-Ru

bond of 2.95 Å and small spin densities on the terminal Ru centres (±0.26). However, both $^1A_{1g}$ and BS(σ,σ) state are not the ground state at BLYP level, the $^3A_{2g}$ ($2a_{1g}^2 2e_{1g}^2 2e_{1u}^4 a_{2u}^2$) is the ground state with very long Ru-Ru bond of 3.30 Å and Mulliken spin densities of 0.43 and 0.51 on Ir and terminal Ru, respectively. With the B3LYP functional, in contrast, 3^{3+} appears much more like the Rh analogue, with symmetry-breaking clearly favored.

The UV-Vis spectrum of the 3^{3+} is shown in Figure 3.8, along with optimized geometry (B3LYP) and Kohn-Sham orbitals. The UV-Vis spectrum is in fact very close to the spectrum of $[Ru_2Cl_3(PEt_3)_6]^{3+}$ reported by Heath and co-workers,[240] suggesting that the electronic configuration at the Ru centres should be similar. The intense band at 9130 cm^{-1} in 3^{3+} has a similar shape to the 11100 cm^{-1} ($\varepsilon = 4550$ $dm^3mol^{-1}cm^{-1}$) band for $[Ru_2Cl_3(PEt_3)_3]^{3+}$. The computed UV-Vis spectrum of $[Ru_2Cl_3(PH_3)_6]^{3+}$ for the BS state is strikingly similar to the experimental one (Figure 3.8), with an intense band computed (TD-DFT-M06-L) at 12515 cm^{-1} due to the $2a_1 \rightarrow 3a_1$ excitation, a metal to metal charge transfer band. The intense band in 3^{3+} at 12517 cm^{-1} is also assigned to the $2a_1 \rightarrow 3a_1$ excitation, and the iso-surface in Figure 3.8 (right) shows the clear localisation of both donor and acceptor orbitals on the left-hand side of the molecule. In the BS state, then, the electronic structure of 3^{3+} can be viewed as an effective $Ru_2(\mu{-}Cl)_3$ dimer, perturbed weakly by the third Ru centre, and as a result the spectra of the two species are strikingly similar.

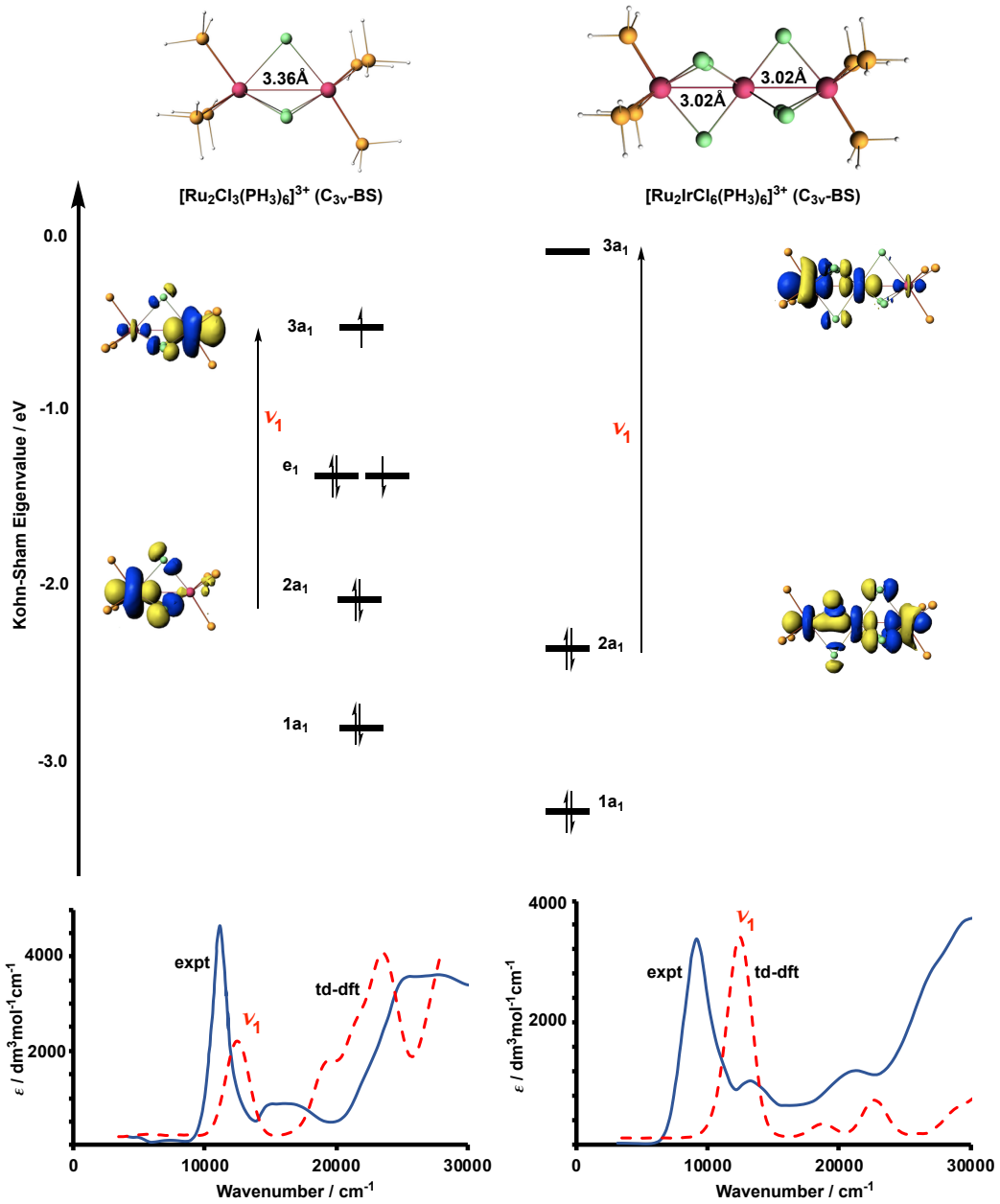

Figure 3.8: Optimized geometry (B3LYP), Kohn-Sham orbital manifold and UV-Vis spectra of $[Ru_2Cl_3(PH_3)_6]^{3-}$ (left) and 3^{3+} (right). The energy scale corresponds to the orbitals of 3^{3+}. The experimental spectrum is shown in blue and the TD-DFT-M06-L in dashed red.

3.3.2 Multi-Configurational SCF (CASSCF) Approach to the Electronic Structure

The DFT study described in the previous section presents a complex picture of the nature of the metal-metal bonding in these isoelectronic systems, with a number of the key conclusions regarding ground states strongly dependent on the choice of functional. Given circumstances, we turned to a wavefunction-based method, and in particular the Complete Active Space (CASSCF) ansatz, as an alternative tool for the study of metal-metal bonds where the generally weak overlap leads to multi-configurational character. We will focus on the 16-electron 1^{2+}, 2^{3+} and 3^{3+} complexes where the presence of two holes in the valence manifold leads to a rich spectrum of states, as shown in Figure 3.9. Depending on the location of the two holes, these configurations can be grouped into three groups: in the first group, the two holes are located in the orbitals with σ-symmetry, giving single-determinant states with $1^1\mathrm{A}_{1g}$, $2^1\mathrm{A}_{1g}$ and $^3\mathrm{A}_{2u}$ symmetry ($\sigma^2\delta_\pi^8$). In the second group, one hole is located in σ manifold and one in δ_π that are $^3\mathrm{E}_{1g}$ and $^3\mathrm{E}_{1u}$ ($\sigma^3\delta_\pi^7$). In the remaining configurations, both holes are located in the δ_π manifold ($\sigma^4\delta_\pi^6$). These configurations are classified in such way because they are related by two electron excitations ($1/2^1\mathrm{A}_{1g}$, $1/2^3\mathrm{E}_{1g}$, $1/2^3\mathrm{E}_{1u}$ and $1/2^3\mathrm{A}_{2g}$) and these may interact strongly in the configuration interaction (CI) matrix as we will see shortly. Furthermore, these effects are likely to become important in the case of the weak metal-metal bonding. To investigate these possibilities, the CASSCF approach followed by second-order perturbation theory (CASPT2) will be used.

For both systems, 1^{2+} and 2^{3+}, we adopt a CAS(10,6) active space, with ten electrons in six orbitals including the $1\mathrm{a}_{2u}$, $1\mathrm{e}_{1u}$, $2\mathrm{e}_{1g}$ and $2\mathrm{a}_{1g}$ orbitals in Figure 3.2. Attempted to expand this space to include the $1\mathrm{e}_{1g}$ and $1\mathrm{a}_{1g}$ orbitals, with an extra six electrons in the active space (CAS(16,9)) provides no further stabilization, and the occupations of the additional orbitals remaining close to 2.0 or 0.0 in the wavefunction.

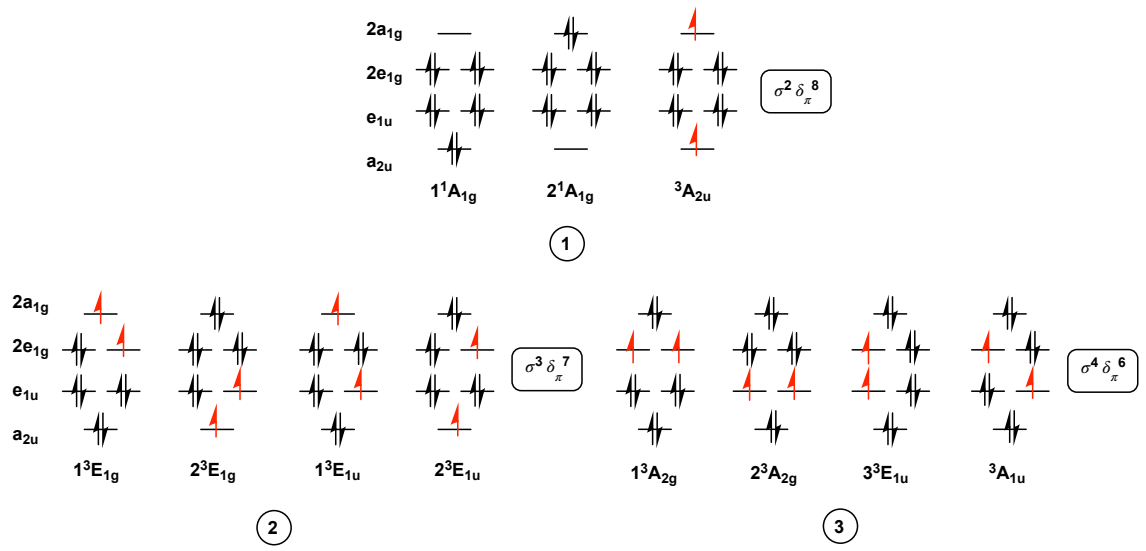

Figure 3.9: The manifold of configurations for the 1^{2+}, 2^{3+} and 3^{3+} (16-electron) systems.

The orbitals were averaged over the nine lowest-lying states of each multiplicity (9 singlets and 9 triplets) that emerge from this active space. In both cases there is a clear separation between these nine lowest states and those at higher energy, and moreover these nine states gave an even distribution of electrons over the two orbitals of σ symmetry and over the four orbitals of δ_π symmetry (as measured by equal populations). The active orbitals of 1^{2+} and 2^{3+} systems are shown in Figure 3.10. In the triplet manifold, the nine states consistent of a $^3\mathrm{A}_{2u}$ state arising from the $\sigma^2\delta_\pi^8$ manifold, and $^3\mathrm{E}_{1g}$ and $^3\mathrm{E}_{1u}$ arising from the $\sigma^3\delta_\pi^7$ manifold. All these states are highly multi-configurational, containing in-phase combinations of the two configurations shown in Figure 3.9 i.e. $1/2^3\mathrm{E}_{1g}$ and $1/2^3\mathrm{E}_{1u}$, with almost equal weights. The $^3\mathrm{A}_{2g}$ state arises from the $\sigma^4\delta_\pi^6$ manifold and is again highly multi-configurational, containing the in-phase combination of $1^3\mathrm{A}_{2g}$ and $2^3\mathrm{A}_{2g}$ configurations shown in Figure 3.10. $^3\mathrm{E}_{1u}$ also arises from $\sigma^4\delta_\pi^6$ manifold, and specifically from two components of the $\mathrm{e}_{1u}^3\mathrm{e}_{1g}^3$ configuration, $\mathrm{e}_{1u}x^1\mathrm{e}_{1u}y^2\mathrm{e}_{1g}x^1\mathrm{e}_{1g}y^2$ and $\mathrm{e}_{1u}x^2\mathrm{e}_{1u}y^1\mathrm{e}_{1g}x^2\mathrm{e}_{1g}y^1$. The final state is $^3\mathrm{A}_{1u}$ state which arising from an in-phase combination of $\mathrm{e}_{1u}x^1\mathrm{e}_{1u}y^2\mathrm{e}_{1g}x^2\mathrm{e}_{1g}y^1$ and $\mathrm{e}_{1u}x^2\mathrm{e}_{1u}y^1\mathrm{e}_{1g}x^1\mathrm{e}_{1g}y^2$.

The singlet manifold contains the eight singlet analogues of the triplets identified above, $^1E_{1g}$ and $^1E_{1u}$, $^1A_{2g}$, $^1E_{1u}$ and $^1A_{1u}$ and in addition it contains the $^1A_{1g}$ state arising from the $\sigma^2\delta_\pi^8$ manifold. This final state, which proves to be the ground state in all systems, is highly multi-configurational, containing weights of the 1^1A_{1g} and 2^1A_{1g} configurations that will be discussed in the following section.

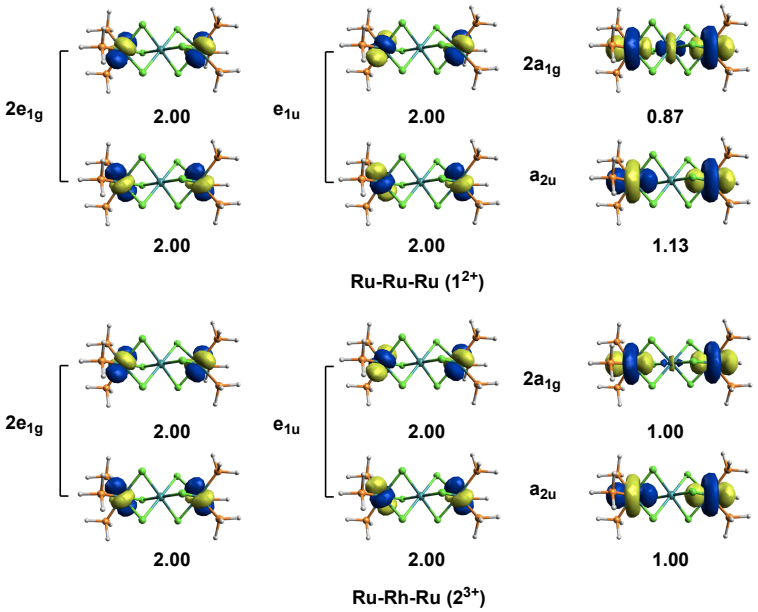

Figure 3.10: Active space natural orbitals of 1^{2+} and 2^{3+} complexes.

The CASSCF calculations were performed on the optimized B3LYP geometry for all systems, with Ru-M separations of 2.87 Å, 3.09 Å and 3.02 Å for 1^{2+}, 2^{3+} and 3^{3+}, respectively. For the 1^{2+} systems, the CASSCF wavefunction for the $^1A_{1g}$ ground state has contributions from both 1^1A_{1g} and 2^1A_{1g} configurations (Figure 3.9) with configuration weights of 0.56 and 0.44, respectively, giving overall occupations of 1.13 and 0.87 for the $1a_{2u}$ and $2a_{1g}$ orbitals, respectively (Figure 3.10). The multi-configurational character of the $^1A_{1g}$ ground state suggests a weak metal-metal bonds with effective bond order of 0.13. The next most stable state is $^3A_{2u}$ (Table 3.3) which is dominated by a single configuration, which at the same geometry lies +0.16 eV higher than the $^1A_{1g}$ state. The multi-configurational $^3E_{1g}$ and $^3E_{1u}$ states are at +0.39 eV and +0.46 eV, respectively while $^3A_{2g}$ lies at +0.99 eV . The CASSCF

wavefunctions of all these states are multi-configurational, this suggests that the DFT energies based on single determinant must be treat with some caution: only the $^3A_{2u}$ state can be reasonably described by single configurational method.

Table 3.3: CASPT2 relative energies (eV) of the manifold configurations of 1^{2+}.

Electronic state	Configuration	E_{rel}
$^1A_{1g}$	$\sigma^2\delta_\pi{}^8$	0.00
$^3A_{2u}$	$\sigma^2\delta_\pi{}^8$	+0.16
1^3E_{1g}	$\sigma^3\delta_\pi{}^7$	+0.39
2^3E_{1g}	$\sigma^3\delta_\pi{}^7$	+0.39
1^3E_{1u}	$\sigma^3\delta_\pi{}^7$	+0.46
2^3E_{1u}	$\sigma^3\delta_\pi{}^7$	+0.46
1^3A_{2g}	$\sigma^4\delta_\pi{}^6$	+0.94
2^3A_{2g}	$\sigma^4\delta_\pi{}^6$	+0.94
$^3E_{1u}$	$\sigma^4\delta_\pi{}^6$	+0.99
$^3A_{1u}$	$\sigma^4\delta_\pi{}^6$	+0.99

The CASSCF wavefunction of the isoelectronic 2^{3+} system is qualitatively similar to that of 1^{2+}. However, the $^3A_{2u}$, $^3E_{1g}$, $^3E_{1u}$ and $^3A_{2g}$ states now all lie within ~0.1 eV of the $^1A_{1g}$ ground state, and the wavefunction of the $^1A_{1g}$ ground state is more multi-configurational than in all-ruthenium system. The weights of the 1^1A_{1g} and 2^1A_{1g} configurations are now 0.50 and the occupations of the $1a_{2u}$ and $2a_{1g}$ natural orbitals are both 1.0. For the 3^{3+} system,$^1A_{1g}$ ground state again has contributions from 1^1A_{1g} and 2^1A_{1g} configurations with weight of 0.52 and 0.48, and occupations of the $1a_{2u}$ and $2a_{1g}$ orbitals equal to 1.03 and 0.97, respectively. Both of these lie very close to the biradical limit (where occupations would be 1.0 and 1.0). The series 1^{2+}, 3^{3+} and 2^{3+} therefore represent a progressive weakening of the interaction between the Ru centers, so the extent that they are close to the exchange coupled limit for the latter two. Even in 1^{2+}, however, the multi-configurational character is extreme, and this may be the origin of the poor match between TD-DFT computed transition energy and the experimental spectrum in this case.

3.4 Conclusion

In this chapter, we have discussed the electronic structure of three isoelectronic complexes with general formula $[(PEt_3)_3Ru(MCl_6)Ru(PEt_3)_3]^{z+}$, $1^{+/2+}$ (M = Ru), $2^{2+/3+}$ (M = Rh) and $3^{2+/3+}$ (M=Ir) systems at both the DFT and CASSCF levels of theory. The UV-Vis spectra of these species are computed using the TD-DFT methodology and are compared to the spectra of the $[MCl_6]^{z-}$ fragments, where these are available. Initial computational tests on different substituents on the phosphine ligands suggest that the $[(PH)_3Ru(MCl_6)Ru(PH)_3]^{z+}$ model that is used throughout is acceptable. For the 17-electron species, the UV-Vis spectra of 1^+ and 3^{2+} show a peak due to metal-to-metal charge transfer that is entirely absent in the $[MCl_6]^{z-}$ fragments. The computed electronic structure at the DFT level shows that replacement of the central Ru^{III} ion by Rh or Ir weakens the metal-metal bonding. The effect is most pronounced in the 16-electron level, where the nature of the metal-metal bonding proves to depend critically on the applied exchange-correlation functional. The CASSCF wavefunction shows that the 1^{2+}, 2^{3+} and 3^{3+} systems differ only in the degree of multi-configurational character in the $^1A_{1g}$ ground state. The continuous variation in the composition of the $^1A_{1g}$ wavefunction maps a transition from weak covalent 3-center-4-electron bonding in 1^{2+} to an exchange-coupled in 2^{3+}, where the Rh^{III} ion act as a diamagnetic bridge between two paramagnetic Ru^{III} centers. These systems highlight the point that covalent bonding and antiferromagnetic coupling are simply two ends of a continuous spectrum, with many cases lying between these two limits.

Chapter 4

Metal-Metal Bonding in Face-Shared Tetranuclear Metal Chains: The Effect of the Oxidation States

4.1 Introduction

This chapter focusses on the electronic structure of the $(PEt_3)_3Ru[Ru_2Cl_9]Ru(PEt_3)_3$ (4) molecule (Figure 4.1). This structure has a face-shared octahedral architecture which is closely related to the structure of the trimetallic systems described in the previous chapter. This molecule has approximately D_{3h} symmetry with four ruthenium ions lying along the common three-fold rotation axis: each metal ion has an approximately C_{3v} local symmetry.

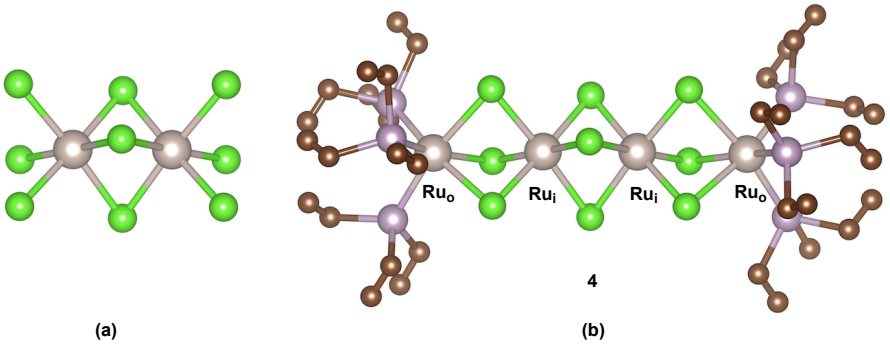

Figure 4.1: The structure of di-metallic, $[Ru_2Cl_9]^{3-}$ (a) along with 4^+. Hydrogen atoms were omitted for clarity.

Our interest in this compound comes from work conducted by our collaborators, Professors Graham Heath, and Alison Edwards and Dr Nicholas Perkins (Australian National University), who have reported the synthesis of 4^+. The synthetic method that gives access to this complex involves taking the $[Ru_2Cl_9]^{3-}$ unit rather than $[MCl_6]^{z-}$ fragments in the trimetallic systems in the previous chapter and capping it with a source of $Ru(PR_3)_3$. The electronic structure of $[Ru_2Cl_9]^{3-}$ is well studied, and its molecular orbital array well known.[241–243] Therefore, to a good approximation, the molecular orbital diagram of 4^+ can be generated based on that of the $[Ru_2Cl_9]^{3-}$ dimer. The six t_{2g} orbitals of the $[Ru_2Cl_9]^{3-}$ unit and the three t_{2g} orbitals from each of the $[Ru(PR_3)_3]^{2+}$ fragments are combined to form twelve molecular orbitals as shown in Figure 4.2. These orbitals split into a σ manifold made up of linear combinations of the d_{z^2} orbitals aligned along the trigonal axis (σ_1, σ_2, σ_3, and σ_4) and a manifold of three doubly degenerate orbitals with mixed δ and π symmetry (δ_{π_1} δ_{π_2}, δ_{π_3}, and δ_{π_4}). The 4^+ complex has a $[Ru_4]^{10+}$ core and hence a valence-electron count of 22, leaving the σ_4 ($2a_2''$) orbital empty.

Detailed spectro-electrochemistry has allowed for characterization of the 4^+ complex in a range of oxidation and reduction states, offering a further opportunity to tune the strength of bonding between the ruthenium ions. The oxidation and reduction processes on the 4^+ ($[Ru_4]^{10+}$) generate four cores, $[Ru_4]^{8+}$, $[Ru_4]^{9+}$, $[Ru_4]^{11+}$ and $[Ru_4]^{12+}$ with valence-electron count of 24, 23, 21 and 20, respectively. The $[Ru_4]^{8+}$ core of the 4^- molecule has no capacity to form metal-metal bonds due to fully occupation of the molecular orbitals of Figure 4.2. However, the other cores have the ability to form metal-metal bonds between ruthenium centers. The metal-metal bonding in these cores can be developed over all four metal ions, or, alternatively, localized on specific part of the molecule.

From an electronic structure point of view, there are different ways to look at this tetra-metallic system. Based on the Figure 4.2 the nature of the ruthenium-ruthenium

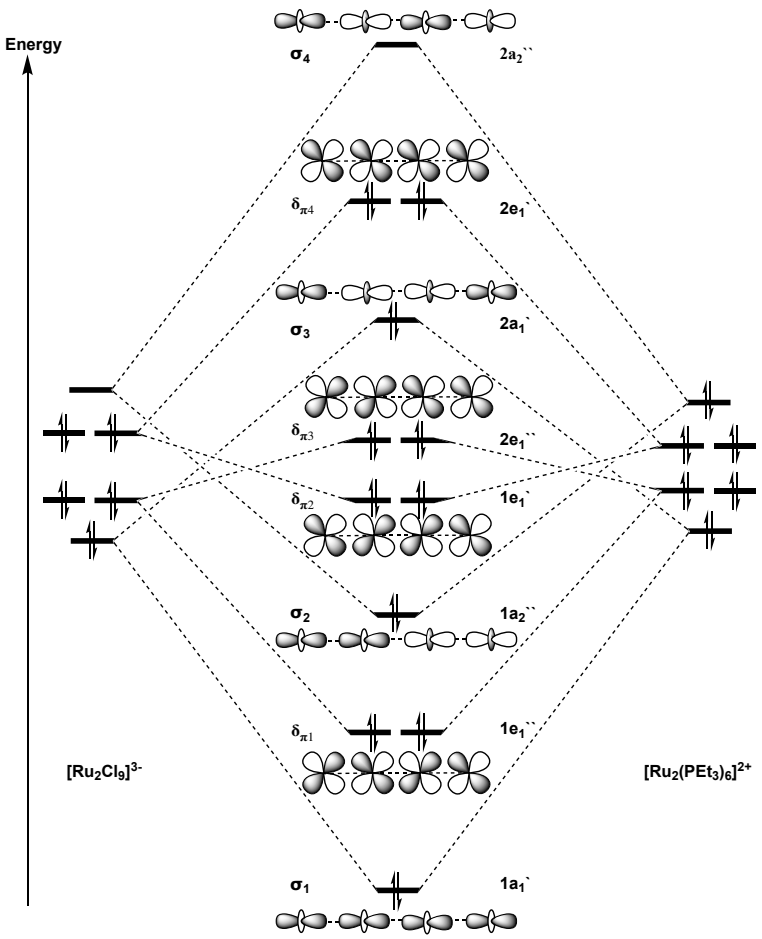

Figure 4.2: Molecular orbital array for $[(PEt_3)_3Ru[Ru_2Cl_9]Ru(PEt_3)_3]^+$ (D_{3h} symmetry).

bonding in these species depends on the relative energies of the t_{2g} orbitals on the $[Ru_2Cl_9]$ unit and the $Ru(PR_3)_3$ fragments. Therefore, we can consider two scenarios: (a) the orbitals on $[Ru_2Cl_9]$ are much higher in energy than those on the outer metals, in which case the metal-metal bonding would be localized in the central $[Ru_2Cl_9]$ unit. (b) the orbitals on $[Ru_2Cl_9]$ unit are much lower than those on the outer metals, in which case the orbitals on the central $[Ru_2Cl_9]$ unit become fully occupied. In this case, the central $[Ru_2Cl_9]$ fragment can be thought of as bridging ligand, mediating the interaction between two paramagnetic ruthenium centers. There is, of course, a continuum of intermediate scenarios of between these two limits.

The central question we aim to address in this chapter is whether we should view

the $(PEt_3)_3Ru[Ru_2Cl_9]Ru(PEt_3)_3$ system as a $[Ru_2Cl_9]$ dimer between two $[Ru(PEt_3)_3]$ inert units or all four ruthenium ions participate in the metal-metal interactions. For this purpose, we compare and contrast the properties of the $[Ru_2Cl_9]^{z-}$ dimer with the $[(PEt_3)_3Ru[Ru_2Cl_9]Ru(PEt_3)_3]^{z+/-}$ chains across a range of oxidation and reduction states, using both density functional theory and multi-configurational (CASSCF/PT2) methods. Our results clearly suggest that the answer to this question depends on the oxidation state of the $(PEt_3)_3Ru[Ru_2Cl_9]Ru(PEt_3)_3$ system. The $[Ru_2Cl_9]^{3-}$ has a 10-electron core ($[Ru_2]^{6+}$) which will be compared to 4^+ which has 22-electron ($[Ru_4]^{10+}$). The reduced form, $[Ru_2Cl_9]^{4-}$ has an 11-electron core ($[Ru_2]^{5+}$) will can be compared to 4^0 with 23-electron core ($[Ru_4]^{9+}$). While the oxidized forms, $[Ru_2Cl_9]^{2-}$ vs 4^{2+} and $[Ru_2Cl_9]^{1-}$ vs 4^{3+} ($[Ru_4]^{12+}$) are also comparable. In the limit that the $[Ru(PEt_3)_3]$ units are inert, the UV-Vis spectrum of the $(PEt_3)_3Ru[Ru_2Cl_9]Ru(PEt_3)_3$ molecule should map directly on to that of $[Ru_2Cl_9]$ dimer analogue.

The work described in this chapter has been submitted for publishing

4.2 Computational Methodologies

All DFT calculations in this chapter were done with the Amsterdam Density Functional package (DFT2016.105).[213–215] In this study, we used two types of functionals, the gradient-corrected BLYP functional of Becke, Lee, Yang, and Parr[216,217] and its hybrid B3LYP,[218,219] in both cases with relativistic scalar corrections (ZORA). A triple-ζ Slater-type basis set extended with a single polarization function (TZP) was used to describe the transition metals while double-ζ Slater-type basis sets extended with a single polarization function (DZP) were used for the main-group atoms. The frozen core approximation was used to treat the electrons in orbitals up to and including 3d on Ru, 2p on P and Cl, and 1s on C. For the calculations with PMe_3 ligands, Grimme's corrections for dispersion were adopted.[220] Symmetry breaking was allowed by reducing the overall symmetry from D_{3h} to C_{3v} and polarizing the starting potential

such that an excess of spin-α and spin-β density was placed on opposite ruthenium centers (using Modifystartpotential keyword in ADF). This allows the electrons to localize in a biradical state if this is more stable than the delocalized alternative, but it does not force them to do so: a spin polarized initial guess can always converge on the delocalized solution if this is more stable. The gradient algorithm of Versluis and Ziegler was used to optimize all structures.[221] Time-dependent DFT[222] was used to calculate UV-Visible spectra with Tamm-Dancoff approximation (TDA)[223] and CH_2Cl_2 as a solvent, the B3LYP and M06-L[224,225] functionals with relativistic scalar corrections (ZORA) were used in this method.

Single point CASSCF/PT2 calculations were done using the MOLCAS 8.0 package.[228] The orbitals are expanded in a basis of atomic natural orbitals optimized for relativistic corrections and core correlation (ANO-RCC).[229] The large primitive set of functions is contracted to [7s6p4d2f1g] for Ru, [4s3p1d] for P and Cl, and [1s] for H. The Cholesky decomposition with threshold of 1.0 e^{-8} was used for the two-electron integrals.[230]

4.3 Results and Discussion

Structural Data: Comparison of X-ray Experiments to DFT

The structure of $[(PEt_3)_3Ru[Ru_2Cl_9]Ru(PEt_3)_3]^+$, 4^+, have been reported in the PhD thesis of Dr. Nicholas Perkins.[231] This system has been identified as a face-shared octahedral architecture shown in Figure 4.1, with two different groups of metal-metal bonds. The Ru-Ru distance between the two inner ions (Ru_i-Ru_i) is 2.696(2) Å while the separation between inner and outer ions (Ru_i-Ru_o) is much longer at 3.102(8) Å. The Ru_i-Ru_i distance is slightly shorter than the value of 2.725(3) Å in the $[Ru_2Cl_9]^{3-}$ molecule.[208] The Ru_i-Ru_o distance value is similar to the value of 3.083(1) Å in the 16-electron $[(PEt_3)_3Ru[RuCl_6]Ru(PEt_3)_3]^+$ system. For the electronic structure investigations, we have applied two quite different computational methodologies, single-

determinate DFT and multi-configurational CASSCF/PT2. At the DFT level, we have considered two quite different functionals BLYP and B3LYP, the latter having 20% Hartree-Fock exchange. In the previous chapter, we have shown that these two functionals provide qualitatively different pictures of metal-metal interactions. We start our discussion by reproducing the X-ray data of 4^+ to validate both the computational methodologies and the simplification used in our model system.

Table 4.1: Comparison of the optimized structure parameters of 4^+ with different substitutions on the phosphine ions (distance in Å).

		Ru_i-Ru_i	Ru_i-Ru_o	Ru_i-Cl	Ru_o-Cl	Ru_o-P
PMe_3	BLYP	2.68	3.13	2.42	2.56	2.29
	B3LYP	2.63	3.12	2.41	2.53	2.30
PH_3	BLYP	2.72	3.17	2.42	2.54	2.31
	B3LYP	2.65	3.15	2.40	2.52	2.31
PEt_3	X-ray	2.696(2)	3.102(8)	2.35	2.50	2.31

The substituents on the phosphine ligands are similar to those in tri-metallic system in the previous chapter (Et groups). To reduce the great flexibility of the Et groups, we replaced this bulky group by smaller groups, Me or H, giving the simplified models $[(PMe_3)_3Ru(Ru_2Cl_9)Ru(PMe_3)_3]^+$ and $[(PH_3)_3Ru(Ru_2Cl_9)Ru(PH_3)_3]^+$. Table 4.1 shows the key optimized structural parameters of 4^+ with different substituents on the phosphine ions, along the crystallographic data. The data suggests that both model ligands do appear to capture the majority of the inductive and steric effects of the alkyl group: the Ru_i-Ru_i bond length of 2.696(2) Å is reproduced to within ±0.02 Å with PH_3 and PMe_3 with BLYP. With B3LYP the Ru_i-Ru_i bond length is reproduced to within about 0.06 Å compared to the X-ray value. The computed values of the Ru_i-Ru_o separation with BLYP are within 0.07 Å and 0.03 Å with PH_3 and PMe_3, respectively. The B3LYP results, in contrast, show that the Ru_i-Ru_o separation within 0.05 Å and 0.02 Å with PH_3 and PMe_3, respectively. Overall, the computed values of the structure parameters of the different substituents suggests

that this simplification of the phosphine ligands does not compromise the description of the metal-metal bonding to any great extent. As a result, we will use the high simplified model ligand PH_3 in the following sections, taking advantage of the ability to impose D_{3h} symmetry with all its advantages.

Electrochemistry

The electrochemistry of compound 4 reported in the PhD thesis of Dr. Nicholas Perkins,[231] is summarized in Table 4.2. We need to note here that X-ray data are not available for any of these electro-generated species. The electrochemistry of 4^+ shows two reversible oxidation waves and two reversible reduction waves as shown in Table 4.2, the first and second oxidation waves are at +0.99 V and +1.16 V, respectively, the first and second reduction waves located at -0.13 V and -1.25 V, respectively. The voltammetry of the $[Ru_2Cl_9]^{3-}$ system also has two reversible oxidation waves and one quasi-reduction wave (Table 4.2) at +0.92 V, +1.58 V and -0.57 V, respectively. The X-ray data of 4 is available for just 4^+ (22-electrons) oxidation state and the 3- oxidation state of the $[Ru_2Cl_9]$ molecule but the UV-Vis spectra are available for the entire oxidation and reduction series of 4 and $[Ru_2Cl_9]$, $4^{3+/2+/+/0/-}$ and $[Ru_2Cl_9]^{-/2-/3-/4-}$. In the following section we will compare 4^{3+}, 4^{2+}, 4^+ and 4^0 to the isoelectronic member of $[Ru_2Cl_9]^{z-}$ series, the purpose of being to understand the nature of changes in metal-metal bonding across a range of oxidation states.

Table 4.2: Oxidation and reduction potentials for 4 and $[Ru_2Cl_9]$ (they examined in the 1+ and 3- states, respectively) vs. Ag/AgCl in CH_2Cl_2 solution.

	$E_{1/2}$(red2)[V]	$E_{1/2}$(red1)[V]	$E_{1/2}$(ox1)[V]	$E_{1/2}$(ox1)[V]
RuRuRuRu (4)	-1.25	-0.13	+0.99	+1.16
Ru_2Cl_9		-0.57	+0.92	+1.58

4.3.1 The Electronic Structure at DFT Level

Electronic Structure of the 22-electron System

We anticipated above that the $[Ru_4]^{10+}$ core has 22 valence-electron which populates all molecular orbitals in Figure 4.2 leaving the $2a_2''$ orbital with σ_4 character empty. The Kohn-Sham molecular orbital diagram of 4^+ shown in Figure 4.3 confirms this. The Kohn-Sham orbital array of 4^+ has similar features to the $[Ru_2Cl_9]^{3-}$, the $1a_1'$, $1e_1''$, $2e_1'$ and $1a_2''$ frontier orbitals of $[Ru_2Cl_9]^{3-}$ with σ, δ_π, δ_π^* and σ^* character, respectively, map directly on to the $1a_1'$, $1e_1''$, $2e_1'$ and $1a_2''$ orbitals of 4^+ molecule. For 4^+, Kohn-Sham array also shows that the linear combinations of the t_{2g} orbitals of the terminal ruthenium ions all lie in a very narrow band this located below the LUMO ($2a_2''$) and above the $1a_1'$ orbital. The ground state for both $[Ru_2Cl_9]^{3-}$ and 4^+ has $^1A_1'$ symmetry, as predicted by both BLYP and B3LYP functionals. The Ru-Ru bond lengths of 2.76 Å and 2.69 Å with BLYP and B3LYP, respectively, for $[Ru_2Cl_9]^{3-}$ compare to the X-ray value of 2.725(3) Å. For 4^+, the iso-surfaces of orbitals in Figure 4.3 (right) show that there is a clear separation between orbitals that are localized on the central Ru ions and those that are localized on the terminal ions. However, there is some contribution from all four Ru ions in all orbitals with σ-symmetry.

The experimental UV-Vis spectrum of 4^+ shows two intense bands at 11780 cm^{-1} (ε = 15320 $dm^3mol^{-1}cm^{-1}$) and 23410 cm^{-1} (ε = 8120 $dm^3mol^{-1}cm^{-1}$). In contrast, the spectrum of $[Ru_2Cl_9]^{3-}$ has no band below 20000 cm^{-1} but shows two bands at 22500 cm^{-1} and 25500 cm^{-1}. The UV-Vis spectra of both systems have been computed at the TD-DFT level with both B3LYP and M06-L functionals as shown in Figure 4.3. For 4^+, the first intense band is computed at 11310 cm^{-1} (ν_1) and 13386 cm^{-1} (ν_1) with M06-L and B3LYP, respectively, and can be assigned to the $2a_1' \rightarrow 2a_2''$ transition. From the iso-surface of the $2a_1'$ and $2a_2''$ orbitals, this band can be clearly assigned as a metal-to-metal charge transfer, specifically, from the outer ruthenium to the inner ruthenium ions. The second intense band is computed at 21366 cm^{-1}

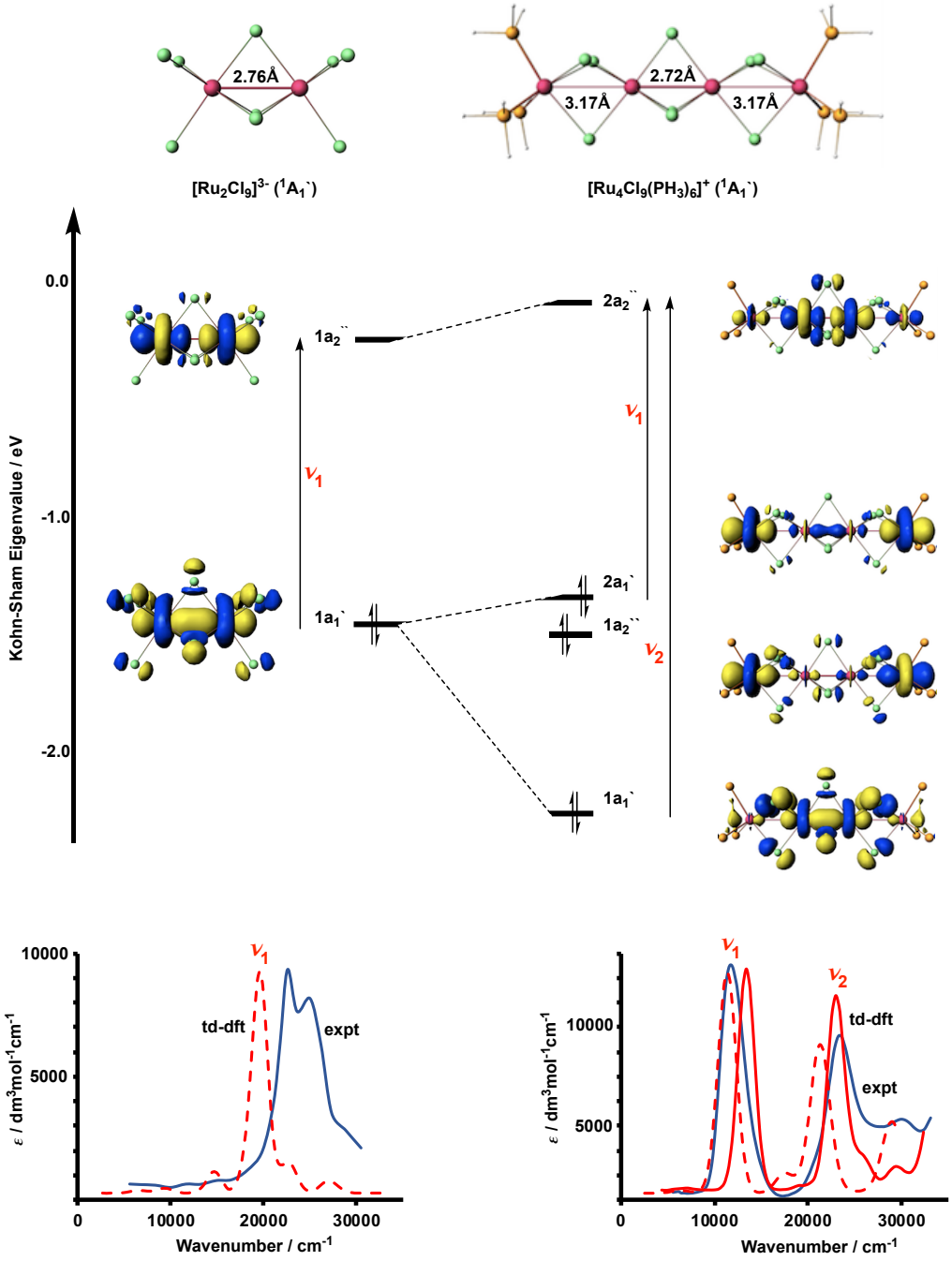

Figure 4.3: Optimized geometry (BLYP), Kohn-Sham orbital manifold and UV-Vis spectra of $[Ru_2Cl_9]^{3-}$ (left) and 4^+ (right). The energy scale corresponds to the orbitals of 4^+. The experimental spectrum is shown in blue, the TD-DFT-M06-L in dashed red and TD-DFT-B3LYP in solid red.

(ν_2) and 22900 cm^{-1} (ν_2) with M06-L and B3LYP functionals, respectively. This band corresponds to the $1a_1' \rightarrow 2a_2''$ transition, the $\sigma \rightarrow \sigma^*$ transition of the central Ru_2Cl_9 unit. The corresponding band in $[Ru_2Cl_9]^{3-}$ is calculated at 19635 cm^{-1} (ν_1) with M06-L, and can be assigned to the feature at 24000 cm^{-1} in the experiment. In a previous study on $[Ru_2Cl_9]^{3-}$ using the SCF-X_α methodology the same assignment was proposed.[242] However, at this level of theory the agreement between the calculated and experimental values was much poorer, this transition is under-estimated by about 7000 cm^{-1}. The TD-DFT methodology gives a much better description of the open-shell excited state than SCF-X_α theory. The $1a_1' \rightarrow 2a_2''$ transition energy is given approximately by ΔW+K where ΔW is the difference in one-electron (orbital) energies given by ΔSCF methodology and K is the exchange integral. In cases where the two singly-occupied orbitals in the excited state (for example $1a_1'$ and $2a_2''$ in $[Ru_2Cl_9]^{3-}$ are localized in the same region of space, the exchange integral is large and its absence in the SCF-X_α approach leads to an underestimation of the energy. Therefore, the deviation from experimental value is found. The positions and intensities of the charge transfer band (ν_1) is found to be sensitive to the applied functionals and this consistent with the literature. For example, the charge transfer band of 4^+ is found at 11310 cm^{-1} (ν_1) and 13386 cm^{-1} (ν_1) with M06-L and B3LYP, respectively, compare to experimental value of 11780 cm^{-1}. The deviation from the experimental value is 470 cm^{-1} with M06-L and 1606 cm^{-1} with B3LYP. Despite the fact that the two functionals shows significant deviation from the experiment, the presence of two intense bands is consistent with the data.

Electronic Structure of the 23-electron System

The reduction of 4^+ and $[Ru_2Cl_9]^{3-}$ molecules populates the $2a_2''$ and $1a_2''$ orbitals, respectively. Therefore, the ground state of both 4^0 and $[Ru_2Cl_9]^{4-}$ systems has $^2A_2'$ symmetry with single unpaired electron in the σ^* orbital (Figure 4.4), as predicted by both BLYP and B3LYP functionals. Populating the $2a_2''$ orbital of 4^0 and the

$1a_2''$ orbital of $[Ru_2Cl_9]^{4-}$ with one unpaired electron leads to elongation of the Ru-Ru bond lengths of both systems. The Ru_i-Ru_i bonds increase by 0.24 Å and 0.23 Å, with BLYP and B3LYP, respectively, compared to 4^+ (2.96 Å vs 2.72 Å with BLYP and 2.88 Å vs 2.65 Å with B3LYP). The Ru_i-Ru_o bonds also elongated by around 0.05 Å with both functionals (3.23 Å vs 3.17 Å with BLYP and 3.18 Å vs 3.15 Å with B3LYP). The effect of populating the $2a_2''$ orbital is less pronounced in the Ru_i-Ru_o distance compare to Ru_i-Ru_i due to small degree of Ru_i-Ru_o σ^* character in the $2a_2''$ orbital. The Ru-Ru bond length of $[Ru_2Cl_9]^{4-}$ also increases by around 0.26 Å with both functionals compared to $[Ru_2Cl_9]^{3-}$ (3.04 Å vs 2.76 Å with BLYP and 2.96 Å vs 2.69 Å with B3LYP).

The experimental UV-Vis spectrum of 4^0 in Figure 4.4 shows two bands at 13000 cm^{-1} and a broad band around 26000 cm^{-1}. The experimental spectrum of $[Ru_2Cl_9]^{4-}$ has an intense band at 12400 cm^{-1}. The similarity between the spectra of 4^0 and $[Ru_2Cl_9]^{4-}$ is obvious, particularly in the area below 20000 cm^{-1}, consistent with the expectation of the $[Ru(PEt_3)_3]^{2+}$ units being inert in a redox sense, making the Ru_2Cl_9 units very similar in both systems. TD-DFT with the M06-L functional predicts two intense bands for 4^0 at 13837 cm^{-1} (ν_1) and 20117 cm^{-1} (ν_2), assigned to $2a_1' \rightarrow 2a_2''$ and $1a_1' \rightarrow 2a_2''$ excitations, respectively. The iso-surface shown in Figure 4.4 (right) shows that the first band (ν_1) is mainly the $\sigma \rightarrow \sigma^*$ transition while the second band (ν_2) is dominated by charge transfer. The order of these transitions is reversed now compared to 4^+; the $\sigma \rightarrow \sigma^*$ transition now occurs at low energy (experimental value of 13000 cm^{-1}), similar to the band at 12400 cm^{-1} of $[Ru_2Cl_9]^{4-}$ which is predicted at 14065 cm^{-1} (ν_1), while the charge transfer band (ν_2) at high energy (experimental value of 26000 cm^{-1}). The ν_1 band is also assigned to $\sigma \rightarrow \sigma^*$ transition in the other systems, for example $[Ru_2Cl_3(PR_3)_6]^{2+}$, $[Ru_2Cl_3(AsR_3)_6]^{2+}$, $[Ru_2Cl_3(NH_3)_6]^{2+}$ and $[Ru_2Cl_3(H_2O)_6]^{2+}$.[244–246] The reason for the shifting of the charge transfer band to higher energy compared to 4^0 is clear: all orbitals on the Ru_2Cl_9 unit (including

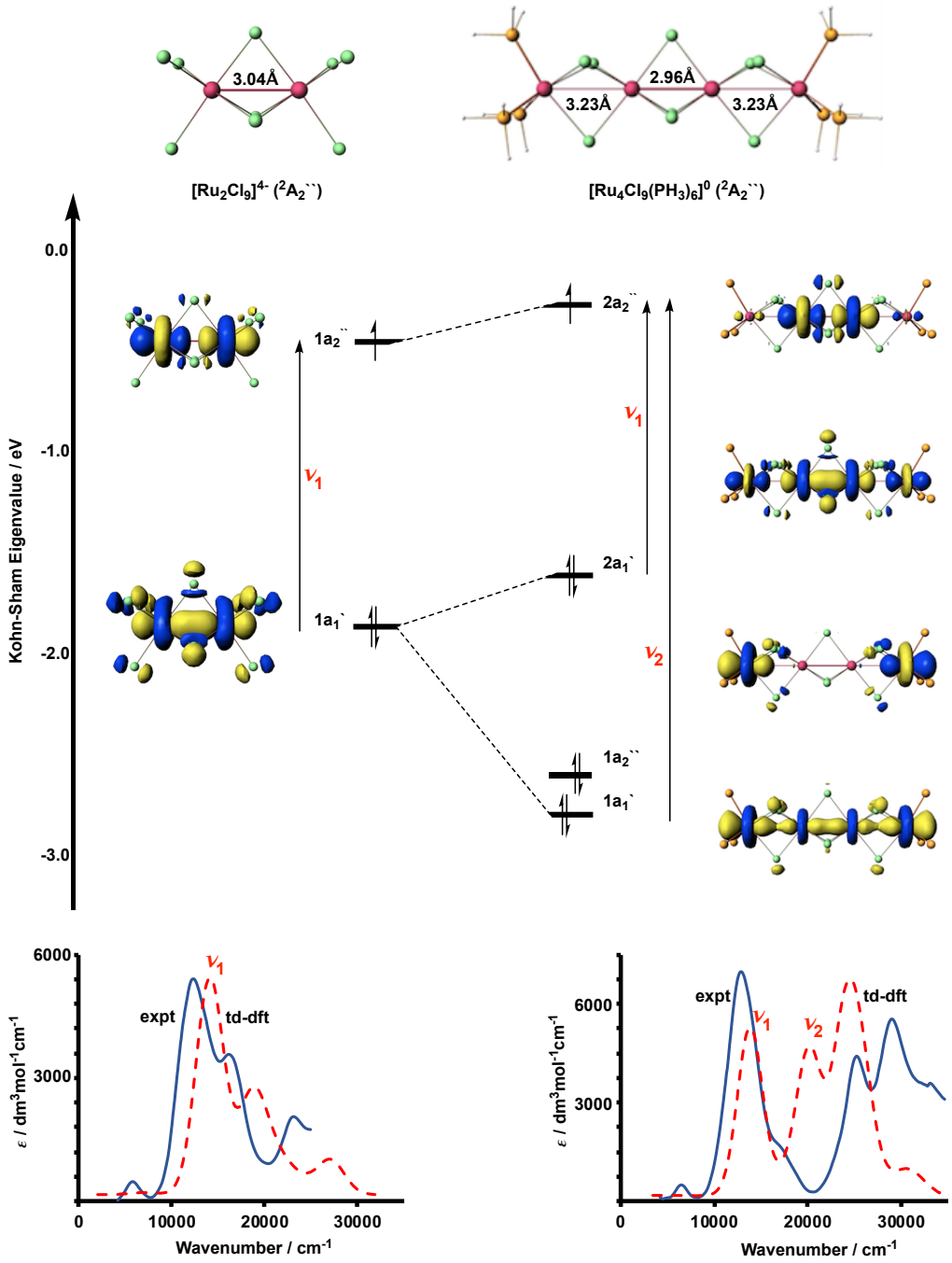

Figure 4.4: Optimized geometry (BLYP), Kohn-Sham orbital manifold and UV-Vis spectra of $[Ru_2Cl_9]^{4-}$ (left) and 4^0 (right). The energy scale corresponds to the orbitals of 4^0. The experimental spectrum is shown in blue, the TD-DFT-M06-L in dashed red.

the SOMO) are upward shifted as a consequence of the reduction process that occurs on the central Ru_2Cl_9 fragment. In contrast, the shift of the $\sigma \rightarrow \sigma^*$ transition to much lower frequency in 4^0 vs 4^+ and also $[Ru_2Cl_9]^{4-}$ vs $[Ru_2Cl_9]^{3-}$ requires further comment because the changes in separation between the relevant orbitals in Figure 4.3 and Figure 4.4 are much less pronounced. In 22-electron and 10-electron systems (4^+ and $[Ru_2Cl_9]^{3-}$), the singlet excited states are multiconfigurational in nature whereas the doublet ground state $^2A_2''$ of 4^0 and $[Ru_2Cl_9]^{4-}$ are well described by a single determinate. As a result, the excitation energy is, to a good approximation, given by the difference in orbital energies (ΔW) and not by ΔW+K. We should therefore be careful when using the frequency of the intense $\sigma \rightarrow \sigma^*$ transition as a direct measure of the metal-metal bond strength.

The second reduction process (4^-) leads to a filled the $2a_2''$ orbital in the Figure 4.2, and, therefore, the net bond order is zero. The computed Ru_i-Ru_i and Ru_i-Ru_o separation values of 3.26 Å and 3.29 Å, respectively, with BLYP are consistent with the absence of metal-metal bonding at this level of oxidation state. The UV-Vis spectrum of 4^- is not of interest because it is featureless below 20000 cm^{-1}, as would be expected due to the large HOMO-LUMO gap. Furthermore, the 5- oxidation state of the isoelectronic dimer Ru_2Cl_9 is not available so we cannot make any direct comparison between these two complexes, 4^- and $[Ru_2Cl_9]^{5-}$.

Electronic Structure of the 21-electron System

At first sight the first oxidation of 4^+ (22 valence electron) should remove one electron from the doubly degenerate $2e_1'$ orbital in Figure 4.2, giving a $^2E_1'$ ($2e_1'^3\ 2a_2''^0$) ground state for both 4^{2+} and $[Ru_2Cl_9]^{2-}$ systems. However, the number of vacancies in the valence manifold has increased (we have three vacancies in 4^{2+} compare to two in 4^+) and alternative arrangements of these three holes have to be considered, the $^4A_1''$ ($2e_1'^2\ 2a_2''^1$) and unsymmetrical-$^2E_1'$ as shown in Table 4.3. The unsymmetrical-$^2E_1'$ state has three different Ru-Ru bond lengths that are Ru_o-Ru_i, Ru_i-Ru_i, and

Ru_i-Ru_o of 2.92 Å, 2.97 Å and 3.05 Å, respectively, with Mulliken spin density of -0.21, -0.43, 1.29, and 0.17, respectively, leading to separate one of the two $Ru(PEt_3)_3$ units. Therefore, the molecule can be viewed as trimetallic systems connected to $Ru(PEt_3)_3$ fragment. The ground state for both 4^{2+} and $[Ru_2Cl_9]^{2-}$ molecules is unsymmetrical-$^2E'_1$, but, the quartet state with very different geometry located at +0.16 eV and +0.36 eV for 4^{2+} and $[Ru_2Cl_9]^{2-}$, respectively. The computed UV-Vis spectra of both 4^{2+} and $[Ru_2Cl_9]^{2-}$ complexes suggest, in contrast, that the ground state should be the quartet ($2e'^2_1\ 2a''^1_2$), as we will see shortly. The fact that these two methodologies (DFT and TD-DFT) suggest different ground states of 4^{2+} means that we turn to multiconfigurational methods (CASSCF/PT2) to rationalize the identity of the ground state of this system.

Table 4.3: Relative energies (eV), optimized bond lengths (Å) and Mulliken spin densities (summed over both inner and outer Ru centres) at B3LYP level of the three states of 4^{2+} and $[Ru_2Cl_9]^{2-}$ systems.

	E_{rel}	Ru_i-Ru_i	Ru_i-Ru_o	ρRu_i	ρRu_o
			4^{2+}		
$^4A''_1$ ($2e'^2_1\ 2a''^1_2$)	+0.16	2.98	3.18	2.21	0.15
$^2E'_1$ ($2e'^3_1\ 2a''^0_2$)	+0.52	2.71	3.13	0.42	0.24
Unsymmetrical-$^2E'_1$	0.00	2.97	2.92, 3.05	+1.29, -0.43	+0.17, -0.21
	E_{rel}	Ru-Ru	ρRu	ρRu	
			$[Ru_2Cl_9]^{2-}$		
$^4A''_1$ ($2e'^2_1\ 2a''^1_2$)	+0.36	3.07	1.20	1.20	
$^2E'_1$ ($2e'^3_1\ 2a''^0_2$)	+0.91	2.64	0.38	0.38	
Unsymmetrical-$^2E'_1$	0.00	2.97	3.21	+1.53, -0.82	

The UV-Vis spectrum of 4^{2+} and $[Ru_2Cl_9]^{2-}$ is shown in Figure 4.5, along with optimized metal-metal bond and the Kohn-Sham orbitals. The experimental spectrum of 4^{2+} shows an intense band at 8200 cm^{-1} (ε = 15400 $dm^3mol^{-1}cm^{-1}$) and a weaker band at 12100 cm^{-1} (ε = 5900 $dm^3mol^{-1}cm^{-1}$). In contrast, the spectrum of $[Ru_2Cl_9]^{2-}$ features a broad band at ∼10000 cm^{-1} and a second band at ∼18000 cm^{-1} with a shoulder to higher frequency. The latter band is similar to those of

$[RuCl_6]^{3-}$ and $[RuCl_6]^{2-}$ reported in the previous chapter (Figure 3.3 and Figure 3.7), of which have both been reported as Cl $\rightarrow$ Ru(IV) charge transfer. The intense band at 10000 cm^{-1} is inconsistent with a similar Cl $\rightarrow$ Ru charge transfer of a localized valence configuration. For both molecules, the ground state at the B3LYP level is unsymmetrical-$^2E_1'$, however, the UV-Vis spectrums seem inconsistent with this ground state. In contrast, the computed spectrum of the $^4A_1''$ state is consistent with the key feature of the experimental spectrum of both systems as shown in Figure 4.5. TD-DFT calculations on the $^4A_1''$ state of $[Ru_2Cl_9]^{2-}$ predict a broad band envelope around 10130 cm^{-1} containing the $\sigma \rightarrow \sigma^*$ one-electron transition (ν_1) and a weaker transition due to the $\delta_\pi \rightarrow \delta_\pi^*$ (ν_2) excitation. The frequency of the $\sigma \rightarrow \sigma^*$ transition is very close to that in $[Ru_2Cl_9]^{4-}$, and the Ru-Ru separation is also similar (3.07 Å vs 2.96 Å (B3LYP)), consistent with their shared $1a_1'^2\ 1a_2''^1$ configuration in the σ manifold.

For 4^{2+} molecule, the major features of computed spectra of all the three states, $^4A_1''$, $^2E_1'$, and unsymmetrical-$^2E_1'$, is similar. All spectra show one intense band and one weaker band at higher wavenumber. The first band (ν_1) is computed at 8239 cm^{-1}, 15000 cm^{-1} and 13191 cm^{-1} for $^4A_1''$, $^2E_1'$ and unsymmetrical-$^2E_1'$ states, respectively. The second band (ν_2) is computed at 13628 cm^{-1}, 17433 cm^{-1} and 16543 cm^{-1} for $^4A_1''$, $^2E_1'$ and unsymmetrical-$^2E_1'$ states, respectively. The intense band ν_1 is dominated by the $2a_1' \rightarrow 2a_2''$ transition while the second band, ν_2, corresponds to $1a_1' \rightarrow 2a_2''$. The quartet and unsymmetrical-doublet states are very close in energy (the quartet just 0.16 eV higher in energy). However, these two states show two different scenarios of metal-metal bonding (Table 4.3): in the quartet state the two terminal ruthenium ions participate in the bonding (spin density on the terminal Ru is 0.15) while in the unsymmetrical-doublet state only one of the terminal Ru centres participates in the bonding. The Mulliken spin density distribution of +0.17, +1.29, -0.43 and -0.21 of unsymmetrical-doublet confirms that the unpaired electron is

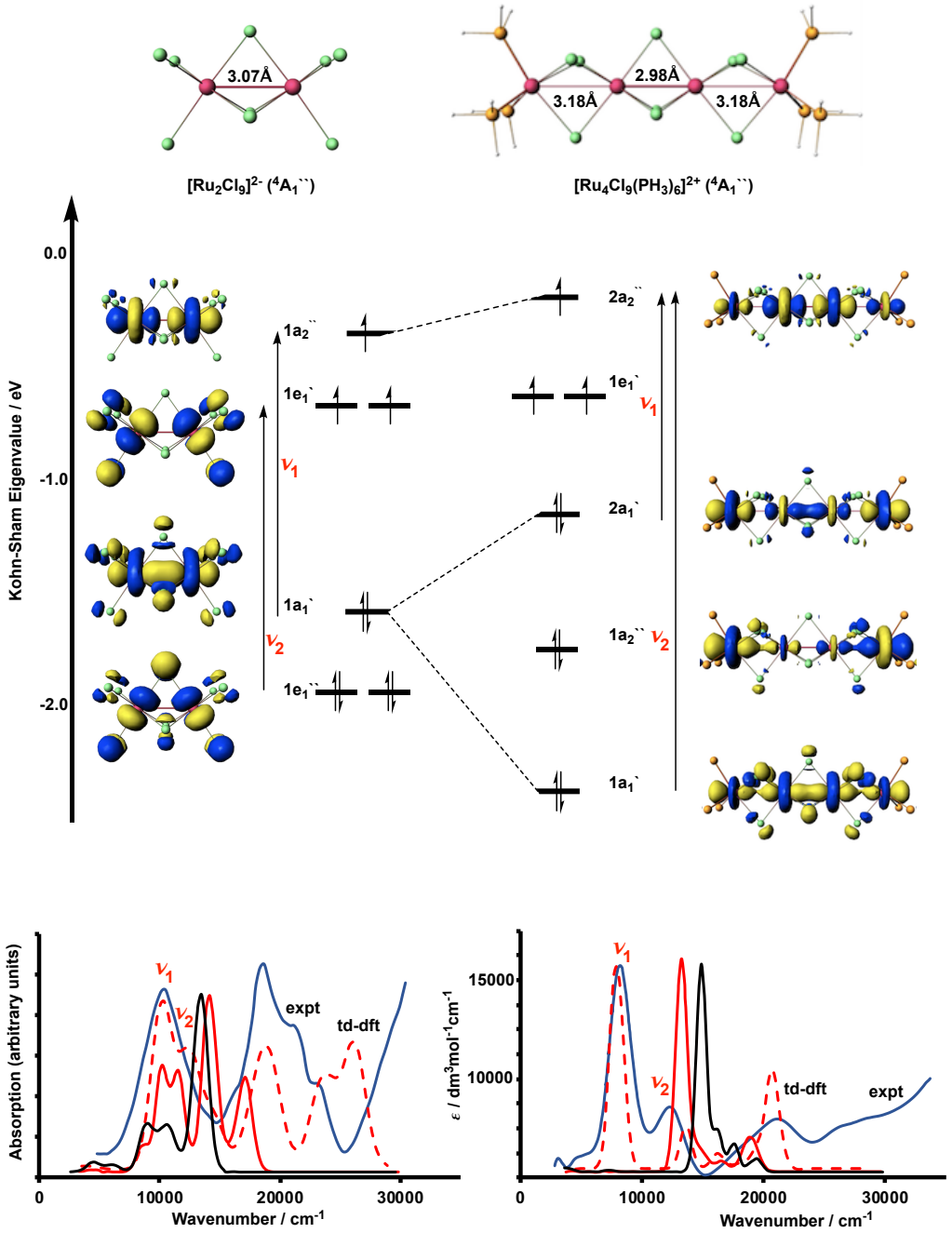

Figure 4.5: Optimized geometry (B3LYP), Kohn-Sham orbital manifold and UV-Vis spectra of $[Ru_2Cl_9]^{2-}$ (left) and 4^{2+} (right). The energy scale corresponds to the orbitals of 4^{2+}. The experimental spectrum is shown in blue, the $^4A_1''$-TD-DFT in dashed red, the unsymmetrical-$^2E_1'$-TD-DFT in solid red and $^2E_1'$-TD-DFT black.

localized on a single centre, giving an oxidation state pattern of $Ru^{2+}Ru^{3+}Ru^{3+}Ru^{3+}$, with the isolated Ru^{2+} centre separated from a trimetallic Ru_3 unit. The localization of orbitals on the different region of space leads to a 2^{nd} order Jahn-Teller instability where the symmetry reduction allows the HOMO and LUMO to mix and then the charge allowed to flow from one $Ru(PH_3)_3$ cap to the Ru_2Cl_9 unit. On the other hand, the quartet shows that the charge transfer flows symmetrically from both $Ru(PH_3)_3$ caps to the central Ru_2Cl_9 unit, the $2a_1' \rightarrow 2a_2''$ transition in Figure 4.5. The iso-surface of the $2a_1'$ orbital is localized mainly on the $Ru(PH_3)_3$ caps while the $2a_2''$ is localized on the central Ru_2Cl_9 dimer. The second band ν_2 corresponds to the $1a_1' \rightarrow 2a_2''$ ($\sigma \rightarrow \sigma^*$) transition with the $1a_1'$ orbital delocalized over the all three ruthenium ions. In summary, in both quartet and doublet cases the terminal ruthenium ions start to participate to some extent in the metal-metal bonding at this oxidation level.

Electronic Structure of the 20-electron System

The ground state of $[Ru_2Cl_9]^{1-}$ is a broken-symmetry singlet (BS-$^1A_1'$) with antiferromagnetically coupled Ru^{4+} centres, a Ru-Ru separation of 3.31 Å and Mulliken spin density of ± 1.50 (B3LYP). In contrast, the broken-symmetry singlet (BS-$^1A_1'$) (qualitatively similar to the ground state of $[Ru_2Cl_9]^{1-}$) with Mulliken spin densities of ± 1.04 on the central Ru_2Cl_9 dimer and ± 0.54 on the outer ruthenium ions is not the ground state of 4^{3+}. However, we have located two states very close in energy, a $^5A_1''$ state with $2e_1'^{\,2}2a_1'^{\,1}2a_2''^{1}$ configuration and a close-shell singlet ($^1A_1'$) with $2e_1'^{\,4}2a_1'^{\,0}2a_2''^{0}$ configuration. The closed shell singlet has a total σ bond order of 2.0 distributed over all four ruthenium ions, and the optimized structure has two very short Ru_i-Ru_o bond lengths of 2.70 Å and a long Ru_i-Ru_i distance of 3.19 Å. The oxidation state of this state has a $Ru^{3+}Ru^{3+}Ru^{3+}Ru^{3+}$ arrangement with single bonds between the inner and outer ruthenium centres, this molecule can be viewed as two dimers of $Ru_2Cl_6(PEt_3)_3$. The $^5A_1''$ state differs from the broken-symmetry state only in the coupling between

the Ru_2 units which now has a ferromagnetic arrangement. In both cases, a single electron occupies both $2a_1'$ and $2a_2''$ orbitals, giving relatively long Ru_i-Ru_o (∼2.98 Å).

Table 4.4: Relative energies (eV), optimized bond lengths (Å) and Mulliken spin densities (summed over both inner and outer Ru centres) at B3LYP level of the three states of 4^{3+} system.

	E_{rel}	Ru_i-Ru_i	Ru_i-Ru_o	ρRu_i	ρRu_o
		4^{3+}			
$^5A_1''$ $(2e_1'^2 2a_1'^1 2a_2''^1)$	0.00	3.18	2.97	2.20	1.00
$^1A_1'$ $(2e_1'^4 2a_1'^0 2a_2''^0)$	+0.06	3.19	2.70	0.00	0.00

The optimized geometry (B3LYP) along with Kohn-Sham molecular orbital and experimental and computed UV-Vis spectra of $[Ru_2Cl_9]^{1-}$ and 4^{3+} are shown in Figure 4.6. The experimental UV-Vis spectrum of 4^{3+} has no intense features below 18000 cm^{-1}. There is no sign of a charge transfer band similar to those in the 4^+ and 4^{2+} or the $\sigma \rightarrow \sigma^*$ transition in 4^0. This might reflects substantial charge transfer from both $Ru(PH_3)_3$ caps to the central Ru_2Cl_9 unit occurs in the ground state. The spectrum of $[Ru_2Cl_9]^{1-}$ is very close to that of $[RuCl_6]^{2-}$ in the previous chapter (Figure 3.7) with an intense band located at ∼18000 cm^{-1} consistent with valence-localized configuration. For $[Ru_2Cl_9]^{1-}$, TD-DFT with M06-L at the BS-$^1A_1'$ ground state shows that the spectrum is dominated by Cl → Ru^{4+} charge transfer, which gives a reasonable match to the experimented spectrum. In the previous chapter we have shown that the spectra of $[RuCl_6]^{2-}$ and $[RuCl_6]^{3-}$ are also dominated by Cl → Ru charge transfer.

For 4^{3+}, the quintet and BS-singlet states gives intense $\sigma \rightarrow \sigma^*$ transitions below 15000 cm^{-1} (Figure 4.6) similar to that for $[Ru_2Cl_9]^{4-}$, $[Ru_2Cl_9]^{2-}$ and 4^0 (Figure 4.4, 4.5 and 4.4, respectively). However, this band is completely absent in the experimental spectrum, suggesting that the quintet and BS-singlet states cannot be the ground state of 4^{3+}, despite the fact that the $^5A_1''$ state is more stable than BS-$^1A_1'$ and $^1A_1'$ states. The computed spectrum of the close-shell singlet ($^1A_1'$) state with unoccupied

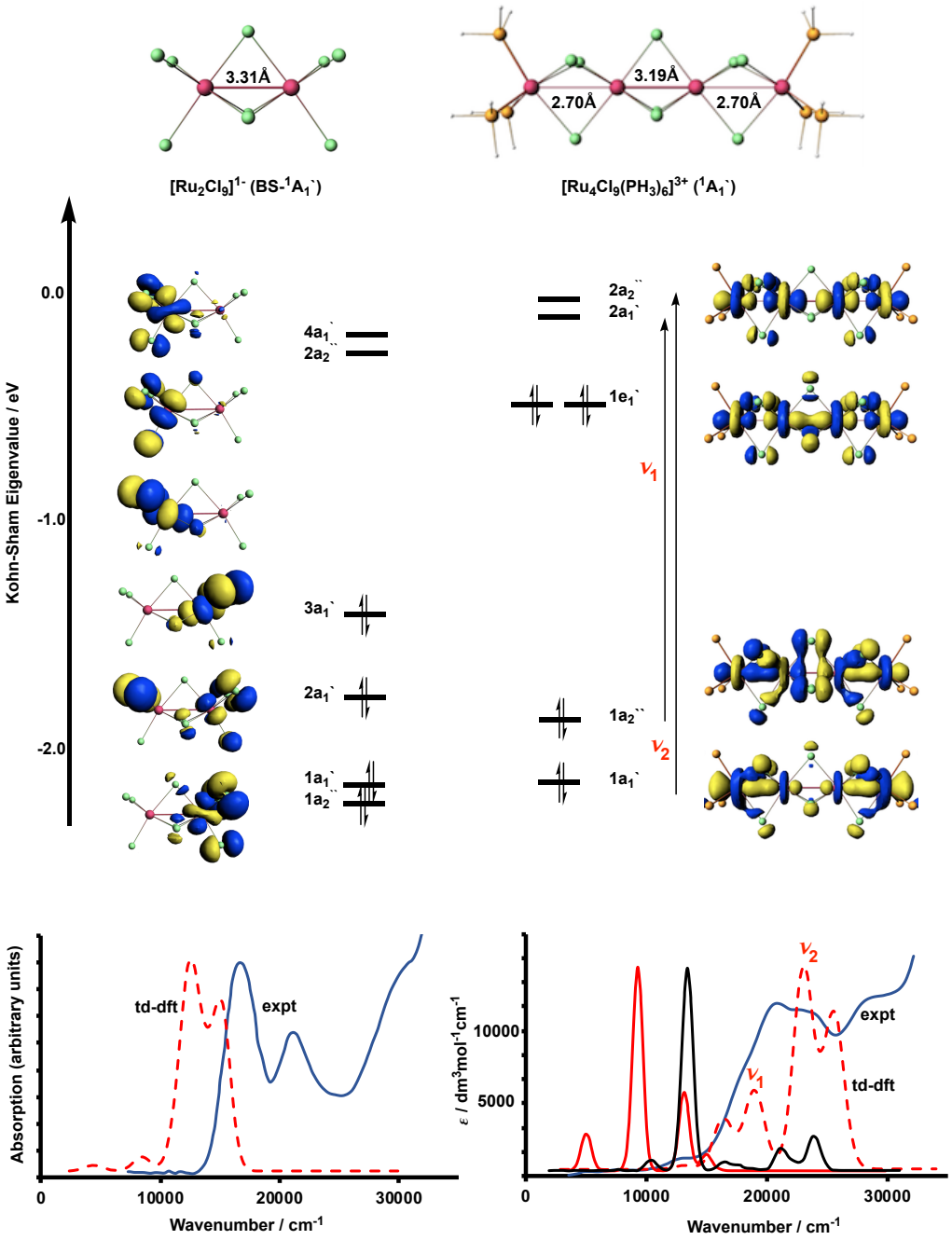

Figure 4.6: Optimized geometry (B3LYP), Kohn-Sham orbital manifold and UV-Vis spectra of $[Ru_2Cl_9]^-$ (left) and 4^{3+} (right). The energy scale corresponds to the orbitals of 4^{3+}. The experimental spectrum is shown in blue, the $^1A_1'$-TD-DFT in dashed red, the $^5A_1''$-TD-DFT in solid red and BS-$^1A_1'$-TD-DFT black.

$2a_1'$ and $2a_2''$ orbitals is, in contrast, a good match with experiment. The first band (ν_1) at 18745 cm^{-1} corresponding to the $1a_2'' \rightarrow 2a_1'$ transition and second band (ν_2) at 22957 cm^{-1} is assigned to the $1a_1' \rightarrow 2a_2''$ transition. The $\sigma^2\sigma^{*0}$ configuration at each dimer unit similar to that in $[Ru_2Cl_9]^{3-}$ and 4^+ (Figure 4.3) where the $\sigma \rightarrow \sigma^*$ transition occurs above 20000 cm^{-1}. Despite the fact that, the spectrum of close-shell singlet matches the experimental spectrum, this is not the predicted ground state, which is $^5A_1''$. The tendency of hybrid functionals to stabilise a configuration with larger number of vacancies in the σ-symmetry ($2e_1'^4 2a_1'^0 2a_2''^0$ vs $2e_1'^2 2a_1'^1 2a_2''^1$) also appears, as it did in the tri-metallic systems introduced in the previous chapter. Therefore, it is hard to conclude the nature of the ground state, although the better match between the experimental spectrum with the close-shell singlet is strong evidence in support of this argument. The CASSCF methodology will be introduced in the next section to identify the nature of the ground state of 4^{3+}.

4.3.2 Multi-Configurational SCF (CASSCF) Approach to the Electronic Structure

In the above section, we have relied on the match between the computed UV-Vis and experimental spectra to identify the ground state of the 4^{2+} and 4^{3+}. However, the possible multiconfigurational nature of 4^+, 4^{2+} and 4^{3+} needs to be investigated to understand the nature of the metal-metal bonding in these systems. For these reasons, in this section, the Complete Active Space SCF (CASSCF) methodology will be introduced.

For 4^+, we have seen in Figure 4.3 that the Kohn-Sham LUMO is mainly localized on central Ru_2Cl_9 dimer, however, there some contributions from the outer ruthenium ions. Therefore, firstly the active space was chosen to be CAS(22,12) that includes all orbitals in the Figure 4.2 with 22 electrons distributed amongst them. These orbitals include the four σ-mainfold orbitals (σ_1, σ_2, σ_3, and σ_4) and the doubly degenerate δ_π-manifold ($\delta_{\pi 1}$ $\delta_{\pi 2}$, $\delta_{\pi 3}$, and $\delta_{\pi 4}$). We found that the orbitals on the terminal ruthenium

ions stay fully occupied in the wavefunction and this has no effect on the CASPT2 energy. In order to reduce the computational cost, the active space was reduced to CAS(10,6) that includes ten orbitals of central Ru_2Cl_9 unit with it is six electrons as shown in Figure 4.8.

We used the state-averaged method, as we did with the trimetallic systems in the previous chapter with the same CAS(10,6) active space; the orbitals were averaged over nine lowest-lying states of each multiplicity (9 singlets and 9 triplets). A systematic representation of these states is shown in Figure 4.7. In the triplet manifold, the nine states consist of $^3A_1''$ arising from the $\sigma^2\delta_\pi{}^8$ manifold, four states of $1/2^3E_1''$ and $1/2^3E_1'$, both have $\sigma^3\delta_\pi{}^7$ configuration, and four states of $1/2^3A_2''$ and $1/2^3A_2'$, both have $\sigma^4\delta_\pi{}^6$ manifold. Table 4.5 shows CASPT2 relative energies of these nine states compared to $^1A_1'$ state, this state is the most stable as predicted by DFT.

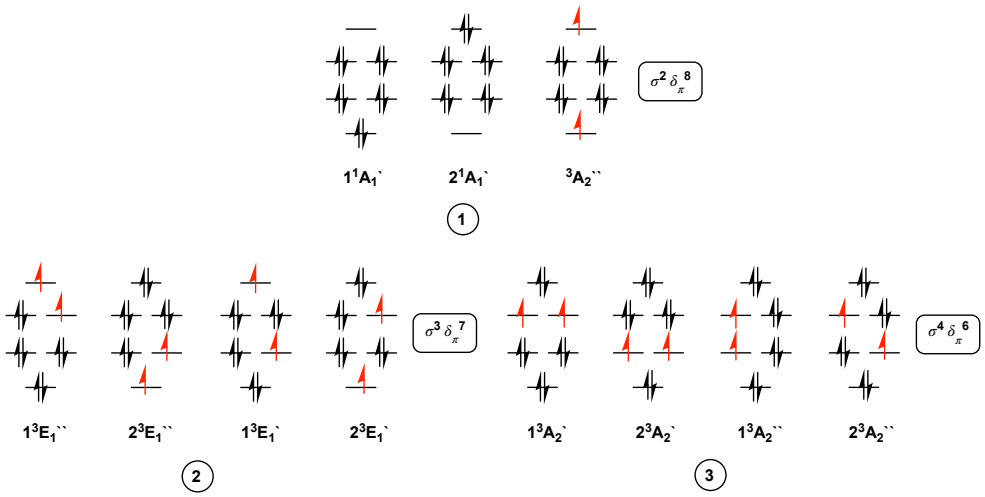

Figure 4.7: The manifold of configurations for the 4^+ (22-electron) system.

To analyse the wavefunction of the $^1A_1'$ state we used the B3LYP geometry, Ru_i-Ru_i of 2.72 Å and Ru_i-Ru_o of 3.17 Å. The total wavefunction of the $^1A_1'$ ground state has $\delta_\pi{}^4\delta_\pi^{*4}\sigma^2\sigma^{*0}$ and $\delta_\pi{}^4\delta_\pi^{*4}\sigma^0\sigma^{*2}$ configurations with weights of 0.78 and 0.22, respectively, giving occupations of 1.55 and 0.45 of σ and σ^* orbitals, respectively, as shown in Figure 4.8. This multiconfigurational nature of the ground state cannot be captured by a single determinant DFT method.

Table 4.5: CASPT2 relative energies (eV) of the manifold configurations of 4^{+} at B3LYP geometry (Ru_i-Ru_i of 2.72 Å and Ru_i-Ru_o of 3.17 Å)

Electronic state	Configuration	E_{rel}
$^1A_1'$	$\sigma^2\delta_\pi{}^8$	0.00
$^3A_1''$	$\sigma^2\delta_\pi{}^8$	+1.23
$1^3E_1''$	$\sigma^3\delta_\pi{}^7$	+0.56
$2^3E_1''$	$\sigma^3\delta_\pi{}^7$	+0.56
$1^3E_1'$	$\sigma^3\delta_\pi{}^7$	+0.56
$2^3E_1'$	$\sigma^3\delta_\pi{}^7$	+0.55
$1^3A_2''$	$\sigma^4\delta_\pi{}^6$	+0.94
$2^3A_2''$	$\sigma^4\delta_\pi{}^6$	+0.94
$1^3A_2'$	$\sigma^4\delta_\pi{}^6$	+0.94
$2^3A_2'$	$\sigma^4\delta_\pi{}^6$	+0.94

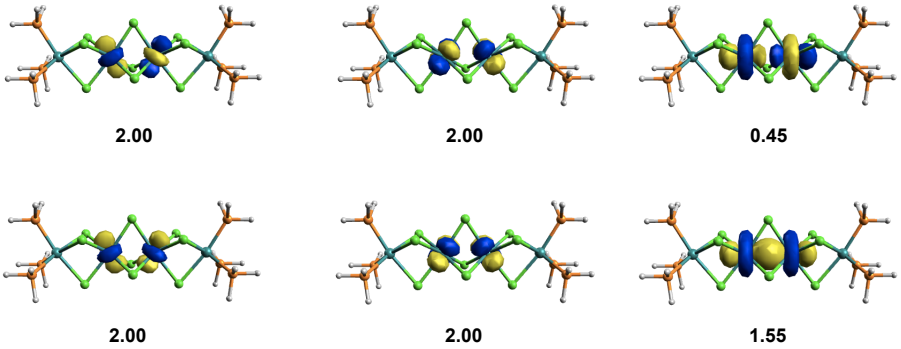

Figure 4.8: Active space natural orbitals of 4^{+} molecule with it is occupations of $^1A_1'$ ground state.

For 4^{2+}, DFT predicts that the ground state is unsymmetrical-$^2E_1'$, however, the computed UV-Vis spectrum of $^4A_1''$ is a better match to the experimental spectrum (Figure 4.5), this suggests that $^4A_1''$ should be the ground state. The geometries of these two states, the $^4A_1''$ and unsymmetrical-$^2E_1'$, are very different (Table 4.3). The active space of both unsymmetrical-$^2E_1'$ and $^4A_1''$ state was chosen to be CAS(21,12) that includes all twelve orbitals of Figure 4.2 and 21 electrons distributed amongst them. We found that the unsymmetrical-$^2E_1'$ geometry is used, the orbitals of one terminal ruthenium ion (the Ru_o of Ru_i-Ru_o bond length of 3.05 Å) stay fully occupied in the wavefunction. Therefore, the active space was reduced to CAS(15,9) that includes the orbitals of three ruthenium ions (six orbitals of Ru ions of central Ru_2Cl_9

unit and three orbitals of one terminal ruthenium ion) and 15 electrons. However, at the $^4A_1''$ geometry we found that both terminal ruthenium orbitals stay fully occupied in the wavefunction, hence, the active space was reduced to CAS(9,6) that includes just six orbitals of central Ru_2Cl_9 fragment with it is nine electrons. In CAS(15,9) active space we need to average over 36 states while using CAS(9,6) required averaging over 18 states. Using different sizes of active space and averaging over different states make energy comparison very difficult. However, the UV-Vis shapes of the unsymmetrical-$^2E_1'$ and $^2E_1'$ are very similar, this suggests that these two states in principle have similar electronic structures even thought their geometries are significantly different. Noticeably, the geometries of quartet and doublet states are close to each other (both have short Ru_i-Ru_i bond length and long Ru_i-Ru_o separation (Table 4.3), then, we can use the same size of active space (CAS(9,6)) and we can compare them to rationalize the identity of the ground state of 4^{2+}.

Using a CAS(9,6) active space on both $^4A_1''$ and $^2E_1'$ geometries (Table 4.3), we found that in both cases the $^4A_1''$ state is more stable than $^2E_1'$ by around 0.2 eV. This is consistent with TD-DFT which predicts the spectrum of $^4A_1''$ state is in better agreement with experimental spectrum than the unsymmetrical-$^2E_1'$ and $^2E_1'$ states. To analysis the wavefunction we have used the geometry of the quartet state with Ru_i-Ru_i of 2.98 Å and Ru_i-Ru_o of 3.18 Å. The ground state has $\delta_\pi{}^4\delta_\pi^{*2}\sigma^2\sigma^{*1}$ and $\delta_\pi{}^2\delta_\pi^{*4}\sigma^2\sigma^{*1}$ configurations with weights of 0.65 and 0.35, respectively, giving total occupations of 3.32 and 2.68 of δ_π and $\delta_\pi{}^*$, respectively, and 2.00 and 1.00 of σ and σ^*, respectively, as shown in Figure 4.9.

For 4^{3+}, DFT calculations show that the ground state has $^5A_1''$ symmetry, however, the computed UV-Vis spectrum matches better to the spectrum of closed-shell $^1A_1'$ state. Therefore, to rationalize the identity of the ground state we have used the CASSCF/PT2 method. Figure 4.6 shows that the Kohn-Sham orbitals are delocalized over four ruthenium ions, more precisely, over the two $Ru_2Cl_3(PH_3)_3$ dimers

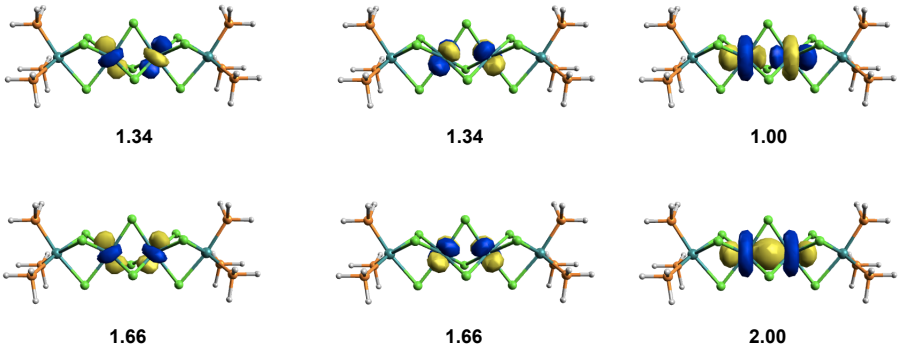

Figure 4.9: Active space natural orbitals of 4^{2+} molecule with it is occupations of $^4A_1''$ ground state.

of 4^{3+}. Therefore, the active space should include all orbitals of the four ruthenium ions, this active space is CAS(20,12). We found that all orbitals with δ_π-symmetry stay fully occupied in the wavefunction similar to those in 4^+ where the correlation happens just between the orbitals with σ-mainfold of $^1A_1'$ state. Because we have two $Ru_2Cl_3(PH_3)_3$ dimers and the correlations happen in 4^+ between the σ-mainfold orbitals of the Ru_2Cl_9 dimer, the active space was reduced to CAS(4,4) that includes just the orbitals within the σ-mainfold as shown in Figure 4.10. The quintet and closed-shell singlet states have different geometry, Ru_i-Ru_i of 3.18 Å and Ru_i-Ru_o of 2.97 Å for the quintet state and Ru_i-Ru_i of 3.19 Å and Ru_i-Ru_o of 2.70 Å for the closed-shell singlet state. Therefore, the CASSCF/PT2 calculations was done on both geometries, one set of calculations using the singlet and quintet multiplicities on close-shell $^1A_1'$ geometry, and another set with both multiplicities on the $^5A_1''$ geometry. For both geometries, we found that the close shell singlet state is more stable than quintet state, by 3.14 eV and 1.22 eV at the closed-shell singlet and quintet geometries, respectively. At the closed-shell $^1A_1'$ geometry, the $^1A_1'$ state has $\sigma_1{}^2\sigma_2{}^0\sigma_3{}^2\sigma_4{}^0$ and $\sigma_1{}^0\sigma_2{}^2\sigma_3{}^0\sigma_4{}^2$ configurations with weights of 0.62 and 0.05, respectively, giving overall occupations of 1.58, 0.42, 1.57, 0.43 of σ_1, σ_2, σ_3, and σ_4, respectively. On the $^5A_1''$ geometry these two configurations have weight of 0.46 and 0.10 of the total wavefunction, respectively, giving overall occupations of 1.37, 0.63, 1.34, 0.66 of σ_1, σ_2, σ_3,

and σ_4, respectively. In summary, the CASSCF/PT2 suggest that the close-shell $^1A_1'$ state is the ground state as predicted by TD-DFT.

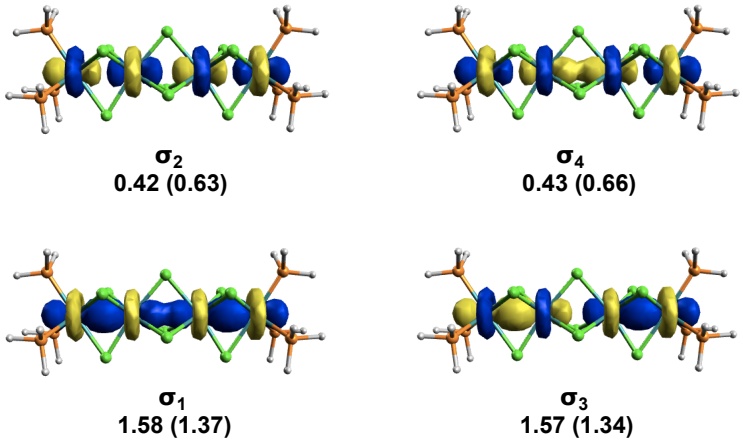

Figure 4.10: Active space natural orbitals of 4^{3+} molecule with it is occupations of the closed-shell $^1A_1'$ state on both $^1A_1'$ and $^5A_1''$ geometries. The occupations of quintet geometry between the parenthesis.

4.4 Conclusion

In this chapter, we have discussed the electronic structure of 4 in a range of oxidation state (4^- to 4^{3+}) using both DFT and CASSCF methods. The electronic structure of 4^0, 4^+, 4^{2+} and 4^{3+} is compared to $[Ru_2Cl_9]^{4-}$, $[Ru_2Cl_9]^{3-}$, $[Ru_2Cl_9]^{2-}$ and $[Ru_2Cl_9]^-$, respectively. The UV-Vis spectra of the 4^0, 4^+, 4^{2+} and 4^{3+} molecules are computed using the TD-DFT methodology and they compared to the spectra of the $[Ru_2Cl_9]^{z-}$ fragments. If the capping $Ru(PEt_3)_3$ units in 4 are inert in redox sense, then the central Ru_2Cl_9 units of 4^0, 4^+, 4^{2+} and 4^{3+} are isoelectronic with the four species of $[Ru_2Cl_9]^{z-}$. Therefore, the comparison of their spectra can be used to validate this assumption and hence probe the extent to which the redox chemistry can drive the formation of metal-metal bonds. The electronic structure of 4^0 and 4^+ is qualitatively similar to $[Ru_2Cl_9]^{4-}$ and $[Ru_2Cl_9]^{3-}$. The ground states of 4^0 and 4^+ have $^2A_2''$ and $^1A_1'$ symmetries, respectively, identical to those in $[Ru_2Cl_9]^{4-}$ and $[Ru_2Cl_9]^{3-}$. The computed UV-Vis spectra of 4^0 and 4^+ confirm these assignments of the ground state.

The UV-Vis spectra of all molecules (4^0, 4^+, $[Ru_2Cl_9]^{4-}$ and $[Ru_2Cl_9]^{3-}$) show a band corresponding to $\sigma \rightarrow \sigma^*$, but the spectra of 4^0 and 4^+ feature additional bands corresponding to metal to metal ($Ru_o \rightarrow Ru_i$) charge transfer. In 4^0, the charge transfer band is blue shifted by about 10000 cm^{-1} consistent with a reduction process that localized entirely on the central Ru_2Cl_9 unit. In 4^+, the CASSCF method shows that the orbitals on the terminal ruthenium ions are very stable compare to those on the central Ru_2Cl_9 dimer. Therefore, there is no driving force to include them in the active space, as illustrated by CASPT2 calculations where the CAS(10,6) has the same ground state energy as CAS(22,12). In both 4^0 and 4^+, the DFT, TD-DFT and CASSCF/PT2 methods indicate that the $Ru(PEt_3)_3$ caps do not significantly participate in the metal-metal bonding. This situation changes in the 4^{2+} and 4^{3+} molecules where the spectra of tetra- and bi-metallic systems appear rather different and the DFT calculations show ground states of different multiplicity. These differences come from the presence of the d_{z^2} orbitals on the terminal ruthenium ions of 4 which can donate electron density into central Ru_2Cl_9 unit. For 4^{2+}, there are two plausible candidates for the ground state, but at DFT level both (unsymmetrical-$^2E_1'$ and $^4A_1''$) show some contribution of the terminal $Ru(PEt_3)_3$ caps in the total metal-metal interactions. To try to establish the identity of ground state we used TD-DFT and CASSCF methods. Both methods suggest that the $^4A_1''$ state is the ground state. Finally, upon further oxidation to 4^{3+}, the site of oxidation is clearly the $Ru(PEt_3)_3$ caps, leads to a singlet state with $Ru^{3+}Ru^{3+}Ru^{3+}Ru^{3+}$ valence configuration with short Ru-Ru bonds between the inner and outer ruthenium centers. The ground state of 4^{3+} is not definitive at DFT level and alternative $^5A_1''$ state lies very close in energy. However, the singlet state with short Ru_i-Ru_o bond lengths offers a convincing match to the experimental UV-Vis spectrum, and CASCF/PT2 calculations support this assignment.

Chapter 5

Metal-Metal Bonding in $(Cp^*RuCl)_2(\mu\text{-}Cl)_2$: A Case of Bond-Stretch Isomerism?

5.1 Introduction

This chapter is closely linked to the two previous chapters where we have also explored metal-metal bonding in linear clusters of ruthenium. This chapter also focuses on metal-metal bonding, but now in the solid-state, and so periodic density functional theory is the tool of choice. The system of interest is $(Cp^*RuCl)_2(\mu{-}Cl)_2$ where $Cp^* = C_5Me_5$, the X-ray structure of which is taken from a report by Kölle and co-workers.[247–249] The remarkable feature of this system is that two different isomers of $(Cp^*RuCl)_2(\mu{-}Cl)_2$, with dramatically different bond lengths, are present in same unit cell as shown in Figure 5.1. The Ru-Ru bond length in the first of these is 2.930(1) Å while in the second it is 3.752(1) Å. In the context of metal-metal bonding, such bond lengths are characteristic of the two extreme limits of covalent bonding on one hand and exchange coupling on the other. The fact that the two isomers coexist suggests that the energetic balance between covalent and exchange-coupling regimes is very delicate, and this presents a very significant challenge to theory. In particular, the presence of a pair of electrons in a Ru-Ru bonding orbital in the short isomer but not in the long isomer means that the electron-electron repulsion problem is rather

different in the two cases.

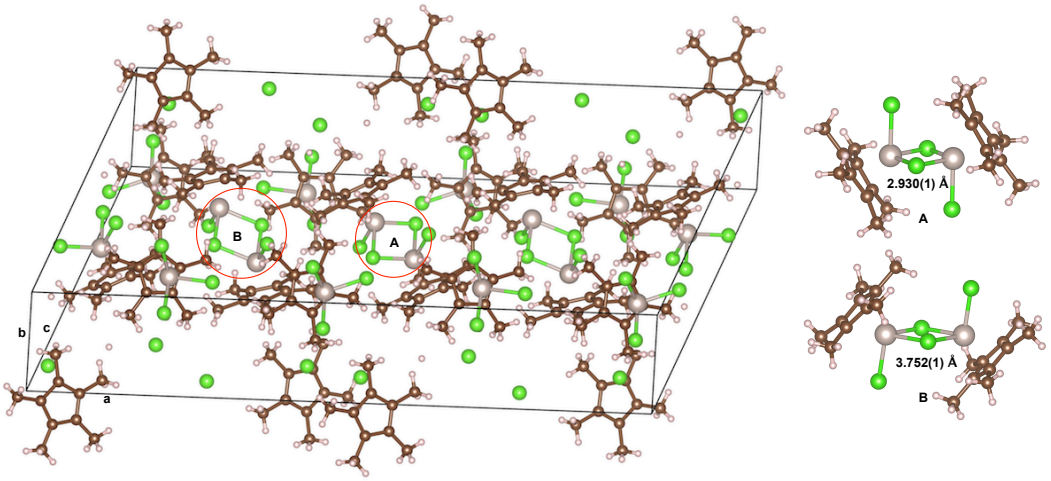

Figure 5.1: X-ray structure of $(Cp^*RuCl)_2(\mu{-}Cl)_2$ system taken from reference 247-249.

The reasons for the coexistence of these isomers in the same unit cell has been debated since the compound was first synthesized in 1991. The elongation of the metal-metal separation from 2.930 Å to 3.752 Å might, in principle, be due to the change in the spin coupling between the Ru centers, from spin singlet (antiferromagnetic) arrangement in the short form (2.930 Å) to a triplet state (ferromagnetic) in the long bond length (3.752 Å). These two arrangements should, in principle, generate a double minimum on the potential surface but in practice, a barrier of at least 1.3 eV would be necessary to allow for the isolation of both isomers under normal conditions.[250]

The electronic structure of system such as this, where two isomers differ only in the length of one or more chemical bonds, is often terms bond-stretch isomerism.[251] The most prominent example of the phenomenon, $[Mo(O)Cl_2(PMe_2Ph)_3]$, was reported by Chatt and co-worker,[252] where a short Mo-O bond is accompanied by a long cis Mo-Cl bond in one isomer, and *vice versa* in the other. The cis-mer-isomer of $[W(O)Cl_2(Me_3tacn)]^+$ was studied by Hoffmann and co-workers using Extended Hückel theory, who argued that the bond-stretch isomerism was a result of electron

redistribution within the π framework of the molecule which leads to a crossing of occupied and unoccupied orbitals in $[W(O)Cl_2(Me_3tacn)]^+$ or to a second-order Jahn-Teller effect in cis-mer-$[Mo(O)Cl_2(PMe_2Ph)_3]$.[250] However, the structure of these systems was later reinvestigated by Hall and Song[253] using ab initio methods, who were able to locate only a single minimum on the potential energy surface. At around same time, the structure of cis-mer-$[Mo(O)Cl_2(PMe_2Ph)_3]$ system was reinvestigated experimentally, and the results show that the different in Mo-O distances is, in fact, an artifact of compositional disorder due to traces of mer-$[MoCl_3(PMe_2Ph)_3]$.[254,255] This clearly illustrates that the level of the quantum chemical methods is crucial in understanding the electronic structure of such systems. At the time, this reinterpretation of the crystallographic data appeared to be the nail in the coffin of the bond-stretch isomerism debate.

Returning to the $(Cp^*RuCl)_2(\mu{-}Cl)_2$ system of interest here, and electronic structure study of the isolated gas-phase molecule using broken-symmetry density functional theory. These calculations confirmed the presence of two minima on the surface, with Ru-Ru separations very close to the experimental values.[256] Moreover, the short Ru-Ru bond was associated with a long terminal Ru-Cl bond in one isomer and vice versa in the other. The fundamental ideas developed by Hoffmann in the context of the molybdenum oxychlorides therefore seem to have some relevance in this case. However, by definition only one of these can be the global minimum, and this was found to be the isomer with a short (i.e. covalent) Ru-Ru bond. A gradient-corrected functional (BP86) was used in this work, and the results reported in previous chapters have highlighted the extreme dependence of Ru-Ru bonding on the precise characteristics of the exchange correlation functional. In this chapter, I revisit the question of the origins of bond stretch isomerism in this system using a wider range of functionals, and also periodic DFT, which allows us to include the wider crystalline environment. We have also applied the CASSCF/CASPT2 methodology developed in the previous

chapters to offer complementary perspective on the Ru-Ru bonding. In the following discussion we will refer to the molecule with short Ru-Ru separation as molecule A and the molecule with long Ru-Ru separation as molecule B.

5.2 Computational Methodologies

All molecular DFT calculations were done with the Amsterdam Density Functional package (DFT2016.105).[213–215] In this study, we used two types of functionals, the gradient-corrected BLYP functional of Becke, Lee, Yang, and Parr[216,217] and its hybrid B3LYP,[218,219] in both cases with relativistic scalar corrections (ZORA). A triple-ζ Slater-type basis set extended with a single polarization function (TZP) was used to describe the Ru centres while double-ζ Slater-type basis sets extended with a single polarization function (DZP) were used for the main-group atoms. The frozen core approximation was used to treat the electrons in orbitals up to and including 3d on Ru, 2p on Cl, and 1s on C. Symmetry breaking was allowed by reducing the overall symmetry from C_{2h} to C_s and polarizing the starting potential such that an excess of spin-α and spin-β density was placed on opposite ruthenium centers (using Modifystartpotential keyword in ADF). This allows the electrons to localize in a biradical state if this is more stable than the delocalized alternative, but it does not force them to do so: a spin polarized initial guess can always converge on the delocalized solution if this is more stable. The gradient algorithm of Versluis and Ziegler was used to optimize all structures.[221]

Single point CASSCF/PT2 calculations were done using the MOLCAS 8.0 package.[228] The orbitals are expanded in a basis of atomic natural orbitals optimized for relativistic corrections and core correlation (ANO-RCC).[229] The large primitive set of functions is contracted to [7s6p4d2f1g] for Ru, [4s3p1d] for Cl, [3s2p1d] for C and [1s] for H. The Cholesky decomposition with threshold of 1.0 e^{-8} was used for the two-electron integrals.[230]

For plane-wave based calculations, the Vienna Ab initio Simulation Package (VASP 5.3.2) was used.[257] All calculations were performed using the GGA-PE functional with the plane-wave basis code. In all calculations, the ions are allowed to move freely, and the cell volume and shape allow to change. Due to large unit cell, Γ-point sampling (a 1x1x1 k-point grid) was used. Different values of the plane-wave energy cut-off and the Hubbard U parameter, U_{eff}, have been used, and these choices will be discussed in detail in the relevant section.

5.3 Results and Discussion

5.3.1 The Electronic Structure at the Molecular DFT Level

Figure 5.2 shows Kohn-Sham molecular orbital arrays of both molecule A and B. We need to note here that the molecular orbital array of $(Cp^*RuCl)_2(\mu{-}Cl)_2$ is qualitatively different from those of face-shared octahedral molecules that discussed in the previous two chapters, the δ- and π-manifold are not degenerate in this system. For molecule A, the ground state has ^1A_g symmetry with σ^* character. The computed Ru-Ru separations of 2.95 Å and 2.89 Å with BLYP and B3LYP, respectively, are in excellent agreement with the value of 2.930(1) Å from the X-ray data. In contrast, the ground state of molecule B has ^3B_u symmetry with two unpaired electrons in the Ru-Ru δ-manifold. The Ru-Ru separation of 3.81 Å and 3.75 Å with BLYP and B3LYP, respectively, are again in excellent agreement with the X-ray value of 3.752(1) Å. The terminal Ru-Cl bond length of molecule A computed at 2.47 Å with both BLYP and B3LYP compared to the X-ray value of 2.418(2) Å. The molecule B has noticeably short terminal Ru-Cl distance of 2.38 Å computed with both BLYP and B3LYP compared to 2.3619(6) Å of the X-ray counterpart. A broken symmetry singlet state, where one electron is localized on one Ru center with spin up and other electron on the second Ru center with spin down (±0.77 with BLYP and ±0.85 with B3LYP) lies only 0.01 eV below the ^3B_u state with both BLYP and B3LYP, consistent

with very weak coupling between the two Ru centers at this distance. These results suggest a strong exchange interaction between two Ru centers in molecule A, but not in molecule B where metal-metal distance is similar to the nonbonding Rh-Rh distance in $(Cp^*RhCl_2)_2$ system.[258]

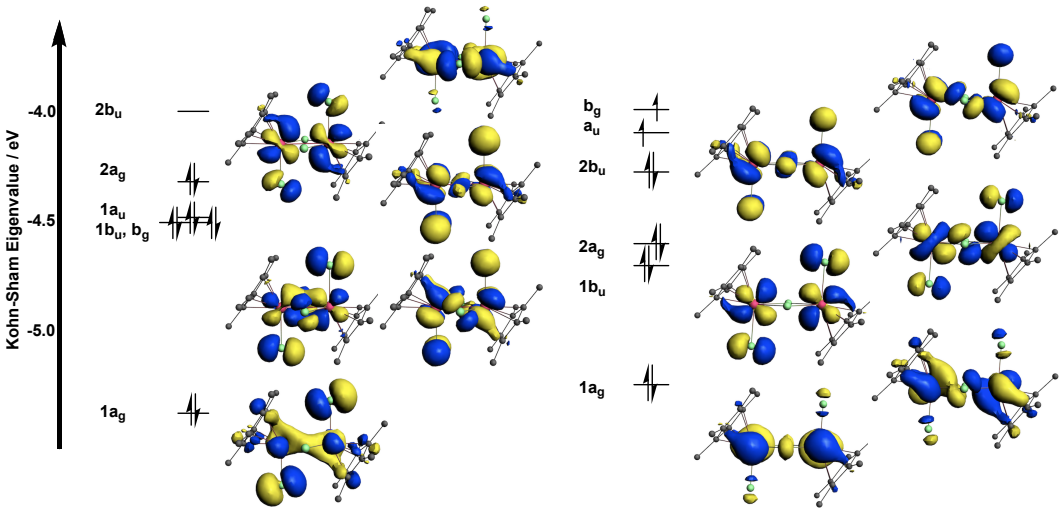

Figure 5.2: Kohn-Sham molecular orbital of molecule A (left) and molecule B (right) computed by BLYP functional.

The unoccupied orbital of molecule A has σ-symmetry while in molecule B the singly-occupied orbitals have δ-symmetry, and so the transition from covalent bonding to exchange coupling is intimately connected to the increase of δ character in the unoccupied manifold as a function of increasing Ru-Ru bond length as we will see in next section. Figure 5.3 shows the potential energy surface of $(Cp^*RuCl)_2(\mu{-}Cl)_2$ for three states, the closed-shell singlet, the triplet and the broken-symmetry (BS) singlet. In the BS state the symmetry was reduced from C_{2h} to C_s, and the BS state was generated from the triplet ($\delta\delta^*$) by flipping the spin from up to down on the second Ru-center. The potential energy surfaces with BLYP and B3LYP show similar general trends, with a minimum at about 2.9 Å for the closed-shell singlet and a minimum at about 3.8 Å for the triplet and BS states. Along the whole PES the triplet and BS states are almost degenerate, even at short Ru-Ru bond lengths, suggesting that the exchange coupling through the δ symmetry orbitals is very weak.

The singlet state is more stable than both the triplet and BS states at bond lengths between 2.5 Å to 3.3 Å, after which the order is reversed. Furthermore, the minima for the triplet and BS states are more stable than the singlet for both BLYP and B3LYP functionals, although the B3LYP functional stabilizes the triplet and BS states substantially compared to singlet.

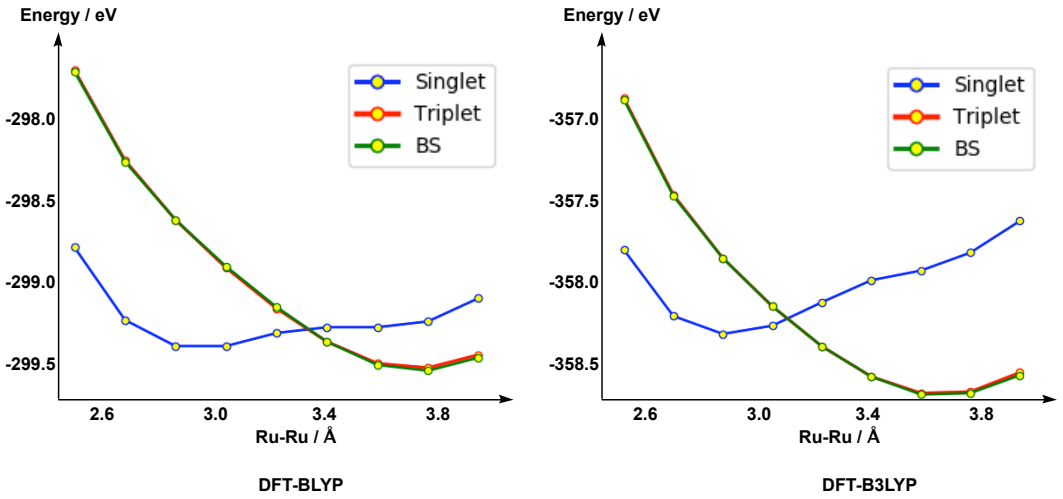

Figure 5.3: Potential energy surface at three different configurations optimized by BLYP (left) and B3LYP (right) functionals.

5.3.2 Multi-Configurational SCF (CASSCF) Approach to the Electronic Structure

In this section, we will investigate the electronic structure of the $(Cp^*RuCl)_2(\mu{-}Cl)_2$ system at the CASSCF level to provide a different perspective on the transition from covalent bonding to exchange coupling. For this reason, we will analysis the wavefunction at the two extremes, at short Ru-Ru and long Ru-Ru bond lengths, then we will look at the composition of the wavefunction at different Ru-Ru bond length between these two extremes. For both systems we adopt a CAS(10,6) active space that includes the six orbitals in Figure 5.3 and the ten electrons distributed among them. A state-averaged approach was used, with the averaging over the nine lowest-lying states (singlets or triplets), as was done in the previous chapters.

For molecule A (short Ru-Ru bond length), the active space orbitals are shown in Figure 5.4: the CASSCF calculations were done on the BLYP optimized geometry of the minimum for the ^1A_g state (Ru-Ru = 2.95 Å). The ground state wavefunction has contributions from two dominant configurations, $\pi^2\pi^{*2}\delta^2\delta^{*2}\sigma^2\sigma^{*0}$ and $\pi^2\pi^{*2}\delta^2\delta^{*2}\sigma^0\sigma^{*2}$, with weights of 0.49 and 0.19, respectively. The remainder of the wavefunction is made up of the $\pi^2\pi^{*2}\delta^2\delta^{*1}\sigma^2\sigma^{*1}$, $\pi^2\pi^{*2}\delta^1\delta^{*2}\sigma^1\sigma^{*2}$, $\pi^2\pi^{*2}\delta^2\delta^{*0}\sigma^2\sigma^{*2}$, and $\pi^2\pi^{*2}\delta^0\delta^{*2}\sigma^2\sigma^{*2}$ configurations with weights of 0.16 , 0.11, 0.03 and 0.02, respectively. This gives ground-state occupations of 1.35 and 0.65 for σ and σ^*, respectively, as shown in Figure 5.4. Thus although the ground state is dominated by configurations with two vacancies in the σ-mainfold, configurations with vacancies in the δ-manifold do contribute.

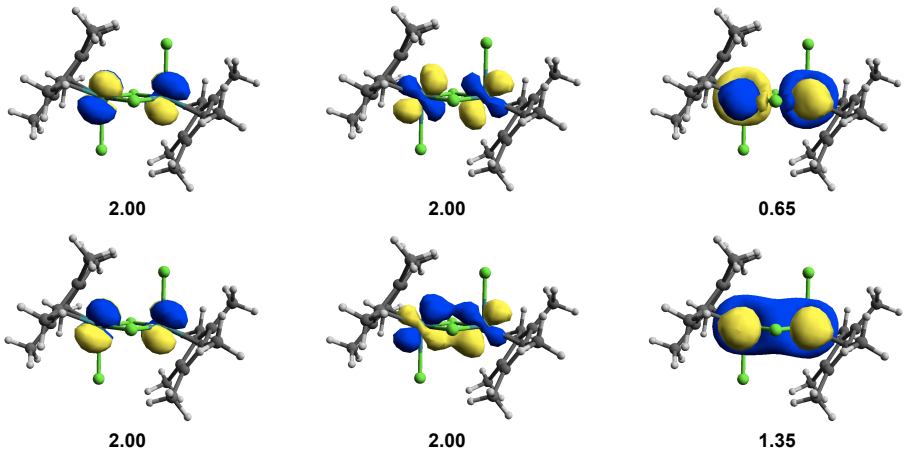

Figure 5.4: Active space orbitals of molecule A (averaged over the nine lowest singlets) and the orbital occupations in the lowest singlet state.

For molecule B, the CASSCF calculation was done at the BLYP-optimized geometry of the ^3B_u state (Ru-Ru = 3.81 Å). The active space of molecule B is shown in Figure 5.5 along with orbital occupations for the lowest singlet. In this case, the ground state has almost equal contributions from the $\pi^2\pi^{*2}\delta^2\delta^{*0}\sigma^2\sigma^{*2}$, and $\pi^2\pi^{*2}\delta^0\delta^{*2}\sigma^2\sigma^{*2}$ configurations (0.49 and 0.51, respectively), giving occupations of 1.02 and 0.98 for δ and δ^*, respectively. Unlike molecule A, the total wavefunction is

completely dominated by configurations with vacancies in the δ-symmetry orbitals. Therefore, we now analyze the changes in the wavefunction across a range of Ru-Ru bond distances intermediate between the covalent and exchange coupling limits.

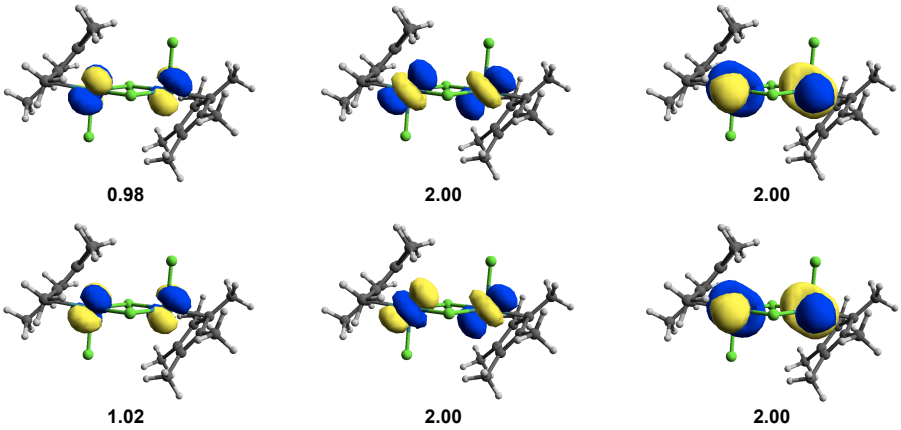

Figure 5.5: Active space orbitals of molecule B (averaged over the nine lowest singlets) and the orbital occupations in the lowest singlet state.

Table 5.1 (top) shows the composition of total wavefunction at different Ru-Ru bond lengths of the lowest-lying singlet state. As the Ru-Ru bond length increases, the weight of configurations with σ-vacancies decreases and the weight of configurations with vacancies in the δ-manifold increases. Between metal-metal bond separations of 2.5 Å and 3.1 Å, the wavefunction is dominated by the $\pi^2\pi^{*2}\delta^2\delta^{*2}\sigma^2\sigma^{*0}$ and $\pi^2\pi^{*2}\delta^2\delta^{*2}\sigma^0\sigma^{*2}$ configurations with the former decreasing in weight. Between 3.1 Å and 3.7 Å, an increasing proportion of the wavefunction is made up of configurations where a single electron is promoted from the δ manifold to σ, such that there is a single vacancy in each. Beyond 3.8 Å, the wavefunction has almost equal weights from the $\pi^2\pi^{*2}\delta^2\delta^{*0}\sigma^2\sigma^{*2}$, and $\pi^2\pi^{*2}\delta^0\delta^{*2}\sigma^2\sigma^{*2}$ configurations with no vacancies in the σ manifold. This is broadly consistent with the DFT calculations where it predicted that the ground state of molecule A has σ-mainfold while the ground state of molecule B has δ-symmetry. Therefore, the transition from covalent bond in molecule A to exchange coupling in molecule B can be understood in terms of a progressive transfer of electron density out of the δ manifold and into σ. For the triplet state,

the wavefunction is dominated by δ and σ manifolds at Ru-Ru bond lengths 2.5 Å to 3.3 Å (Table 5.1 (bottom)). At long Ru-Ru bond distances (3.8 Å and 3.9 Å) the wavefunction has weight of just δ manifold similar to singlet state.

Table 5.1: Total wavefunction composition of different configurations at different Ru-Ru bond lengths (Å) of the lowest-lying singlet and triplet states.

	Ru-Ru								
	2.5	2.7	2.9	3.1	3.3	3.5	3.7	3.8	3.9
lowest-lying singlet state									
$\pi^2\pi^{*2}\delta^2\delta^{*2}\sigma^2\sigma^{*0}$	0.66	0.62	0.52	0.40	0.28	0.19	0.08	0.00	0.00
$\pi^2\pi^{*2}\delta^2\delta^{*2}\sigma^0\sigma^{*2}$	0.14	0.17	0.19	0.19	0.16	0.13	0.07	0.00	0.00
$\pi^2\pi^{*2}\delta^2\delta^{*1}\sigma^2\sigma^{*1}$	0.10	0.11	0.15	0.20	0.25	0.27	0.24	0.00	0.04
$\pi^2\pi^{*2}\delta^1\delta^{*2}\sigma^1\sigma^{*2}$	0.06	0.07	0.10	0.14	0.19	0.22	0.24	0.00	0.03
$\pi^2\pi^{*2}\delta^2\delta^{*0}\sigma^2\sigma^{*2}$	0.03	0.02	0.02	0.04	0.07	0.10	0.19	0.51	0.50
$\pi^2\pi^{*2}\delta^0\delta^{*2}\sigma^2\sigma^{*2}$	0.01	0.01	0.02	0.03	0.06	0.09	0.18	0.49	0.43
lowest-lying triplet state									
$\pi^2\pi^{*2}\delta^2\delta^{*2}\sigma^1\sigma^{*1}$	0.20	0.23	0.32	0.35	0.32	0.28	0.06	0.00	0.00
$\pi^2\pi^{*2}\delta^2\delta^{*1}\sigma^2\sigma^{*1}$	0.53	0.51	0.40	0.33	0.30	0.28	0.20	0.00	0.04
$\pi^2\pi^{*2}\delta^1\delta^{*2}\sigma^1\sigma^{*2}$	0.15	0.17	0.18	0.20	0.21	0.28	0.18	0.00	0.04
$\pi^2\pi^{*2}\delta^1\delta^{*1}\sigma^2\sigma^{*2}$	0.08	0.09	0.11	0.13	0.17	0.22	0.55	1.00	0.93

Figure 5.6 shows the potential energy surface for the singlet and triplet states generated by CASPT2. We again see two distinct minima, one for the singlet at short Ru-Ru separations and the other for the triplet at longer distances. Unlike the DFT studies, however, the singlet state is now more stable than triplet, reflecting the qualitatively correct treatment of the singlet afforded by the CASSCF but not the singlet-determinant DFT methodology.

5.3.3 Solid-State Electronic Structure: the Plane-Wave Approach

In previous sections we have seen that at both the DFT and CASSCF levels there are two local minima on the potential energy surface of the gas-phase molecule, one of which is necessarily more stable than the other (although the identity of the

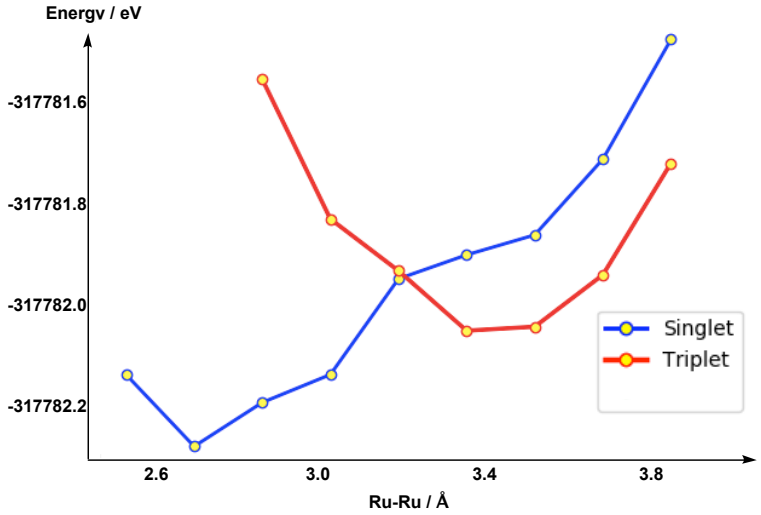

Figure 5.6: Potential energy surface at CASPT2 level.

more stable one depends critically on methodology). However, the X-ray structure of $(Cp^{*}RuCl)_2(\mu{-}Cl)_2$ confirms that both molecule A and B co-exist in the same unit cell, suggesting that the wider crystalline environment plays an important part. Periodic DFT using the plane-wave approach allows us to study the electronic structure of both molecules in the unit cell. The comparison of DFT and CASPT2 approaches for the molecular system highlights the importance of an accurate treatment of the electron-electron repulsion. In the context of periodic DFT, this can be manipulated through the so-called Hubbard U parameter, U_{eff}, which imposes an energetic penalty for double occupation of orbitals. The external pressure and the energy cut-off also present opportunities to perturb the balance between the covalent and exchange-coupled limits. We found that by changing the optimization conditions we can locate all three conceivable scenarios: one short Ru-Ru bond length and one long (as in the X-ray structure), two short Ru-Ru bond lengths and two long Ru-Ru separations. Optimization using an energy cut-off set to the default value of 400 eV and a U_{eff} parameter of zero on the Ru centre Yields the structural parameters summarized in Table 5.2. These parameters are in excellent agreement with X-ray values, with Ru-Ru separations of 2.88 Å and 3.80 Å for molecules A and B, respectively,

compared to 2.930(1) Å and 3.752(1) Å from the X-ray data. The terminal Ru-Cl bonds also show the same pattern observed in the X-ray data, with longer bonds in A and relatively shorter bonds in B. These calculations confirm that the structure with both isomers present in the same unit cell is indeed a local minimum on the potential energy surface, a point that was anticipated based on the gas-phase surface.

Table 5.2: Structural parameters of $(Cp^*RuCl)_2(\mu{-}Cl)_2$ system along with X-ray data (bond distance in Å, Cl_{br} stand for bridging chlorine).

	Ru-Ru	Ru-Cl_t	Ru-Cl_{br}	Ru-Cp
Molecule A				
GGA-PE	2.88	2.46	2.36	2.19
X-ray	2.930(1)	2.418(2)	2.366(1)	2.191
Molecule B				
GGA-PE	3.80	2.37	2.44	2.18
X-ray	3.752(1)	2.365(2)	2.445(1)	2.173

The agreement between X-ray structure parameters and our calculations allow us to analysis the electronic structure of $(Cp^*RuCl)_2(\mu{-}Cl)_2$ system. For molecule A, the spin density is equal to zero everywhere, while for molecule B the spin density at Ru is 0.73 in the ferromagnetic configuration (the initial density of Ru centers was polarized to have parallel arrangements) (Table 5.3). We have also located the corresponding anti-ferromagnetic arrangement (the initial density of Ru centers was polarized to have anti-parallel arrangements), where the spin densities on the two centers are opposed, just 0.03 eV higher in energy.

Table 5.3: Relative energy, spin densities (ρ) for ferromagnetic and anti-ferromagnetic configurations of $(Cp^*RuCl)_2(\mu{-}Cl)_2$ system.

	E_{rel}(eV)	ρ(Ru)/Molecule A	ρ(Ru)/Molecule B
Ferromagnetic	0.00	0.00	0.73
Anti-ferromagnetic	+0.03	0.00	±0.70

In the gas-phase DFT calculations we showed that the vacant orbitals in the

ground states of isomers A and B have character: σ-for molecule A and δ for molecule B. To search for these features in the plane-wave calculations, we have generated a density of state (DOS) diagram for the unit cell, projected onto the 4d orbitals of the Ru centers (Figure 5.7). Molecule A (left) has a completely empty d_{xz} band (note that the Ru-Ru bond is aligned along the bisector of the x and z axes). For molecule B, in contrast, the majority-spin manifold is completely filled and the two vacancies in the minority-spin band are localized in the d_{yz} orbitals (note that there are two such orbitals, one on each Ru center of molecule B). with the projected DOS is therefore entirely consistent with the different nature of the SOMOs of molecule A and B observed at the gas-phase DFT level.

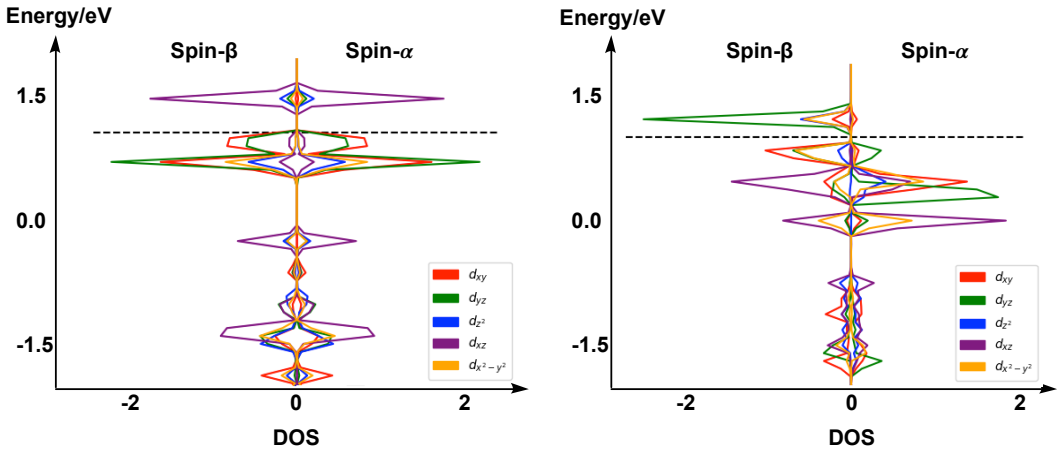

Figure 5.7: DOS of molecule A (left) and B (right), projected onto the Ru 4d orbitals, for the ferromagnetic configuration.

The gas-phase potential energy surfaces in Figure 5.4 highlight the point that increasing amounts of exact Hartree-Fock exchange in the wavefunction stabilize states with singly occupied orbitals over the closed-shell singlet. In periodic DFT, the effects of increasing Hartree-Fock exchange can be replicated by using finite values for the Hubbard U parameter, which imposes an energetic penalty for double occupation of orbitals, effectively favouring electron localisation. To explore whether the nature of the metal-metal bonding can be perturbed by different choices of parameter set, we have re-optimized the structure of the unit cell under different conditions.

Table 5.4 (top) shows the relation between U_{eff} and the optimized structural parameters (the magnetic moments were initialized in a ferromagnetic configuration in all cases). As the value of U_{eff} is increased from 0 to 3 eV, the Ru-Ru bond length in molecule A remains short while the Ru-Ru separation in molecule B remains long. The spin density at the Ru centers in B increases slightly, but otherwise the electronic changes are minimal. As U_{eff} is increased beyond 3.0 eV, the Ru-Ru separation in molecule A increases and finite spin density develops on molecule A. At U_{eff} 6.0 eV, the two molecules, A and B, are almost identical, both structurally and in terms of spin densities. Very similar patterns are apparent in the calculations where an antiferromagnetic alignment of spins was imposed in the initial density. Specifically, we find that for $U_{eff} = 4.0$ eV and larger, the two molecules are electronically identical, although the Ru-Ru separation remains somewhat shorter in A than in B. These calculations highlight again the very delicate balance between covalent and exchange coupled scenarios, a relatively small changes in the treatment of electron-electron repulsion can drive a molecule from one extreme to another.

It is less obvious how we can drive the system to the short-short geometry (i.e more delocalized), because 0.0 eV is clearly the lower limit in U_{eff}. However, by first optimizing the structure with a rather low energy cutoff (200 eV) and an external pressure of 50 GPa, we can converge on a structure with short Ru-Ru bonds in both A and B (2.50 Å and 2.59 Å, respectively). Such a low energy cutoff is clearly far from convergence, but starting from this structure, removing the applied pressure and increasing the cut-off back to the default value of 400 eV, leads to a closed-shell singlet with Ru-Ru bond lengths of 2.71 Å (A) and 2.87 Å (B). This structure is, however, 1.79 eV less stable than the short/long combination described in table 5.4 for $U_{eff} = 0$.

Table 5.4: The relation between U_{eff} and structural parameters of molecule A and B (bond length in Å) in ferromagnetic and in anti-ferromagnetic configurations.

U_{eff}	Ru-Ru in A	Ru-Ru in B	ρ(Ru) in A	ρ(Ru) in B
Ferromagnetic				
0	2.88	3.80	0.00	0.73
1	2.87	3.79	0.00	0.79
2	2.87	3.79	0.00	0.85
3	2.86	3.78	0.00	-0.91
4	3.65	3.79	0.98	-0.97
5	3.42	3.80	1.08	1.04
6	3.64	3.77	1.12	1.12
Anti-ferromagnetic				
0	2.87	3.80	0.00	±0.73
1	2.87	3.79	0.00	±0.78
2	2.86	3.79	±0.01	±0.85
3	3.14	3.78	±0.84	±0.91
4	3.30	3.78	±0.97	±0.98
5	3.36	3.77	±1.05	±1.05
6	3.39	3.76	±1.13	±1.13

5.4 Conclusion

The electronic structure of $(Cp^{*}RuCl)_2(\mu{-}Cl)_2$ system has been studied at three different levels of theory, gas-phase DFT, CASSCF, and periodic DFT. The gas-phase DFT results show that the ground state for the two molecules present in the unit cell have qualitatively different vacant orbitals: in molecule A the vacancy is in the σ manifold while in molecule B they are in the δ manifold. The potential energy surface at this level of theory has two minima corresponding to the different ground states. A more nuanced perspective on the transition from covalent bonding to exchange coupling can be understood by analyzing the CASSCF wavefunction as a function of Ru-Ru distance. An increase in Ru-Ru distance leads first to an increase in contributions from configurations with vacancies in both the σ and δ manifolds at the expense of configurations where both vacancies are in σ orbitals. Beyond 3.7 Å, the σ manifold becomes fully occupied and both vacancies localize in the δ orbitals. The

transition from covalent to exchange-coupled scenarios therefore involves a progressive transfer of electron density from δ to σ.

Periodic DFT confirms that the structure where the two isomers co-exist in the same unit cell is a stable minimum, and moreover that it is more stable than the corresponding case where both bond lengths are short. A relatively modest increase in the value of the Hubbard U parameter, U_{eff}, is sufficient to drive localization and hence a switch to the long/long form.

References

[1] E. C. R. Peligot. *Acad. Sci.*, 19:609–618, 1844.

[2] E. Peligot. *Ann. Chim. Phys.*, 12:528, 1844.

[3] F. A. Cotton, G. Wilkinson, C.A. Murillo, and Bochmann. *Advanced Inorganic Chemistry*. John Wiley & Sons, Inc.:New York, 6th ed., 1999.

[4] J. A. Bertrand, F. A. Cotton, and W. A. Dollase. *Inorg. Chem.*, 2:1166–1171, 1963.

[5] F. A. Cotton and J. T. Mague. *Inorg. Chem.*, 3:1402–1407, 1964.

[6] F. A. Cotton and J. T. Mague. *Inorg. Chem.*, 3:1094–1098, 1964.

[7] F. A. Cotton and S. J. Lippard. *J. Am. Chem. Soc.*, 86:4497–4498, 1964.

[8] F. A. Cotton and S. J. Lippard. *Inorg. Chem.*, 3:59, 1964.

[9] M. J. Bennett, F. A. Cotton, and B. M. Foxman. *Inorg. Chem.*, 7:1563–1569, 1968.

[10] F. A. Cotton, N. F. Curtis, C. B. Harris, B. F. G. Johnson, S. J. Lippard, J. T. Mague, W. R. Robinson, and J. S. Wood. *Science*, 145:1305–1307, 1964.

[11] F. A. Cotton, N. F. Curtis, and W. R. Robinson. *Inorg. Chem.*, 4:1696–1700, 1965.

[12] F. A. Cotton and B. M. Foxman. *Inorg. Chem.*, 7:2135–2140, 1968.

[13] J. D. Eakins, D. G. Humphreys, and C. E. Mellish. *J. Chem. Soc.*, 0:6013–6016, 1963.

[14] F. A. Cotton and W. K. Bratton. *J. Am. Chem. Soc.*, 68:921, 1965.

[15] D. Lawton and R. Mason. *J. Am. Chem. Soc.*, 68:921–922, 1965.

[16] F. A. Cotton, C. A. Murillo, and R. A. Walton. *Multiple Bonds between Metal Atoms*. Springer Science and Business Media, Inc.: New York, 3rd ed., 2005.

[17] F. A. Cotton, N. F. Curtis, C. B. Harris, B. F. G. Johnson, S. J. Lippard, J. T. Mague, W. R. Robinson, and J. S. Wood. *Science*, 145:1305–1307, 1964.

[18] F. L. Campbell, F. A. Cotton, and G. L. Powell. *Inorg. Chem.*, 23:4222–4226, 1984.

[19] F. A. Cotton, P. E. Fanwick, J. W. Fitch, H. D. Glicksrman, and R. A. Walton. *J. Am. Chem. Soc.*, 101:1752–1757, 1979.

[20] F. L. Campbell, F. A. Cotton, and G. L. Powell. *Inorg. Chem.*, 24:4384–4389, 1985.

[21] F. A. Cotton, J. G. Jr. Norman, B. R. Stults, and T. R. Webb. *J. Coord. Chem.*, 5:217–223, 1976.

[22] C. D. Garner, I. H. Hillier, M. J. Knight, A. A. MacDowell, I. B. Walton, and M. F. Guest. *J. Chem. Soc., Faraday Trans.*, 76:885, 1980.

[23] D. L. Lichtenberger and R. L. Johnston. *Metal-Metal Bonds and Clusters in Chemistry and Catalysis*. Jr. Fackler and P. John (Ed.); Plenum Press: New York, 1990.

[24] X. B. Wang and L. S. Wang. *J. Am. Chem. Soc.*, 122:2096–2100, 2000.

[25] M. J. Bennett, F. A. Cotton, and R. A. Walton. *Proc. R. Soc. London*, A303: 175–192, 1968.

[26] F. A. Cotton, E. A. Hillard, and C. A. Murillo. *Inorg. Chem.*, 41:1639–1644, 2002.

[27] T. J. Barder, F. A. Cotton, D. Lewis, W. Schwotzer, S. M. Tetrick, and R. A. Walton. *J. Am. Chem. Soc.*, 106:2882–1891, 1984.

[28] T. J. Barder, F. A. Cotton, K. R. Dunbar, G. L. Powell, W. Schwotzer, and R. A. Walton. *Inorg. Chem.*, 24:2550–2554, 1985.

[29] F. A. Cotton, N. S. Dalal, P. Huang, S. A. Ibragimov, C. A. Murillo, P. M. B.

Piccoli, C. M. Ramsey, A. J. Schultz, X. Wang, and Q. Zhao. *Inorg. Chem.*, 46: 1718–1726, 2007.

[30] G. M. Chiarella, F. A. Cotton, N. S. Dalal, C. A. Murillo, Z. Wang, and M. D. Young. *Inorg. Chem.*, 51:5257–5263, 2012.

[31] J. F. Berry, F. A. Cotton, P. Huang, and C. A. Murillo. *Dalton Trans.*, 0: 1218–1219, 2003.

[32] G. M. Chiarella, F. A. Cotton, and C. A. Murillo. *Chem. Commun.*, 47:8940–8942, 2011.

[33] F. A. Cotton, N. S. Dalal, E. A. Hillard, P. Huang, C. A. Murillo, and C. M. Ramsey. *Inorg. Chem.*, 42:1388–1390, 2003.

[34] F. A. Cotton, G. M. Chiarella, N. S. Dalal, C. A. Murillo, Z. Wang, and M. D. Young. *Inorg. Chem.*, 49:319–324, 2010.

[35] F. A. Cotton and E. Pedersen. *Inorg. Chem.*, 14:383–387, 1975.

[36] J. F. Berry, E. Bill, E. Bothe, F. A. Cotton, N. S. Dalal, S. A. Ibragimov, N. Kaur, C. Y. Liu, C. A. Murillo, S. Nellutla, J. M. North, and D. Villagran. *J. Am. Chem. Soc.*, 129:1393–1401, 2007 and references cited therein.

[37] F. A. Cotton, C. Lin, and C. A. Murillo. *Inorg. Chem.*, 39:4574–4578, 2000 and references cited therein.

[38] J. F. Berry, F. A. Cotton, P. Huang, C. A. Murillo, and X. Wang. *Dalton Trans.*, 0:3713–3715, 2005.

[39] W.-Z. Cheng, F. A. Cotton, N. S. Dalal, C. A. Murillo, C. M. Ramsey, T. Ren, and X. Wang. *J. Am. Chem. Soc.*, 127:12691–12696, 2005.

[40] F. A. Cotton, C. A. Murillo, and R. A. Walton. *Multiple Bonds between Metal Atoms*. Springer Science and Business Media, Inc.: New York, 3rd ed., 2005.

[41] W.-Z. Cheng, F. A. Cotton, N. S. Dalal, C. A. Murillo, C. M. Ramsey, T. Ren, and X. Wang. *J. Am. Chem. Soc.*, 127:12691–12696, 2005.

[42] W. Klotzbuecher and G. A. Ozin. *Inorg. Chem.*, 16:984–987, 1977.

[43] S. K. Gupta, R. M. Atkins, and K. A. Gingerich. *Inorg. Chem.*, 17:3211–3213, 1978.

[44] M. D. Morse. *Chem. Rev.*, 86:1049–1109, 1986.

[45] S. M. Casey, P. W. Villalta, A. A. Bengali, C. L. Cheng, J. P. Dick, P. T. Fenn, and D. G. Leopold. *J. Am. Chem. Soc.*, 113:6688–6689, 1991.

[46] M. H. Chisholm and A. M. Macintosh. *Chem. Rev.*, 105:2949–2976, 2005.

[47] A. Dedieu, T. A. Albright, and R. Hoffmann. *J. Am. Chem. Soc.*, 101:3141–3151, 1979.

[48] Y. C. Tsai, Y. M. Lin, J. S. K. Yu, and J. K. Hwang. *J. Am. Chem. Soc.*, 128: 13980–13981, 2006.

[49] F. Weinhold and C. R. Landis. *Chem. Educ. Res. Pract.*, 2:91–104, 2001.

[50] T. Nguyen, A. D. Sutton, M. Brynda, J. C. Fettinger, G. J. Long, and P. P. Power. *Science*, 310:844847, 2005.

[51] T. Nguyen, W. A. Merrill, C. Ni, H. Lei, J. C. Fettinger, B. D. Ellis, G. J. Long, M. Brynda, and P. P. Power. *Angew. Chem., Int. Ed.*, 47:9115–9117, 2008.

[52] R. Wolf, C. Ni, T. Nguyen, M. Brynda, G. J. Long, A. D. Sutton, R. C. Fischer, J. C. Fettinger, M. Hellman, L. Pu, and P. P. Power. *Inorg. Chem.*, 46: 1127711290, 2007.

[53] K. A. Kreisel, G. P. A. Yap, O. Dmitrenko, C. R. Landis, and K. H. Theopold. *J. Am. Chem. Soc.*, 129:14162–14163, 2007.

[54] Y. C. Tsai, C. W. Hsu, J. S. K. Yu, G. H. Lee, Y. Wang, and T. S. Kuo. *Angew. Chem., Int. Ed.*, 47:7250–7253, 2008.

[55] C. W. Hsu, J. S. K. Yu, C. H. Yen, G. H. Lee, Y. Wang, and Y. C. Tsai. *Angew. Chem., Int. Ed.*, 47:9933–9936, 2008.

[56] A. Noor, F. R. Wagner, and R. Kempe. *Angew. Chem., Int. Ed.*, 47:7246–7249, 2008.

[57] A. Noor, G. Glatz, R. Müllerr, M. Kaupp, S. Demeshko, and R. Kempe. *Nat. Chem.*, 1:322–325, 2009.

[58] Y. C. Tsai, H. Z. Chen, C. C. Chang, J. S. K. Yu, G. H. Lee, Y. Wang, and T. S. Kuo. *J. Am. Chem. Soc.*, 131:12534–12535, 2009.

[59] A. Noor, G. Glatz, R. Müller, M. Kaupp, S. Demeshko, R. Kempe, and Z. Anorg. *Allg. Chem.*, 635:1149–1152, 2009.

[60] S. C. Liu, W. L. Ke, J. S. K. Yu, T. S. Kuo, and Y. C. Tsai. *Angew. Chem., Int. Ed.*, 51:6394–6397, 2012.

[61] Y. L. Huang, D. Y. Lu, H. C. Yu, J. S. K. Yu, C. W. Hsu, T. S. Kuo, G. H. Lee, Y. Wang, and Y. C. Tsai. *Angew. Chem., Int. Ed.*, 51:7781–7785, 2012.

[62] L. J. Clouston, R. B. Siedschlag, P. A. Rudd, N. Planas, S. Hu, A. D. Miller, L. Gagliardi, and C. C. Lu. *J. Am. Chem. Soc.*, 135:13142–13148, 2013.

[63] Y. C. Tsai, C. W. Hsu, J. S. K. Yu, G. H. Lee, Y. Wang, and T. S. Kuo. *Angew. Chem., Int. Ed.*, 47:7250–7253, 2008.

[64] S. C. Liu, W. L. Ke, J. S. K. Yu, T. S. Kuo, and Y. C. Tsai. *Angew. Chem., Int. Ed.*, 51:6394–6397, 2012.

[65] T. J. Hurley and M. A. Robinson. *Inorg. Chem.*, 7:33–38, 1968.

[66] S. Aduldecha and B. Hathaway. *J. Chem. Soc., Dalton Trans.*, 0:993–998, 1991.

[67] G. J. Pyrka, M. El-Mekki, and A. A. Pinkerton. *J. Chem. Soc., Chem. Commun.*, 0:84, 1991.

[68] L. P. Wu, P. Field, T. Morrissey, C. Murphy, P. Nagle, B. Hathaway, C. Simmons, and P. Thornton. *J. Chem.Soc., Dalton Trans.*, 0:3835–3840, 1990.

[69] L. G. Zhu and S. M. Peng. *Wuji Huaxue Xuebao*, 18:117, 2002.

[70] C. Y. Yeh, C. C. Wang, C. H. Chen, and S. M. Peng. *Nano Redox Sites: Nano-Space Control and its Applications.* T. Hirao (Ed.), Springer: Berlin, 2006.

[71] J. F. Berry. *Structure and Bonding*, 136:1–28, 2010.

[72] S. A. Hua, M. C. Cheng, C. H. Chen, and S. M. Peng. *Eur. J. Inorg. Chem.*, 0:2510–2523, 2015.

[73] C. C. Wang, W. C. Lo, C. C. Chou, G. H. Lee, J. M. Chen, and S. M. Peng. *Inorg. Chem.*, 37:4059–4065, 1998.

[74] S. J. Shieh, C. C. Chou, G. H. Lee, C. C. Wang, and S. M. Peng. *Angew. Chem. Int. Ed. Engl.*, 36:56–59, 1997.

[75] H. C. Chang, J. T. Li, C. C. Wang, T. W. Lin, H. C. Lee, G. H. Lee, and S. M. Peng. *Eur. J. Inorg. Chem.*, 0:1243–1251, 1999.

[76] F. A. Cotton, L. M. Daniels, T. Lu, C. A. Murillo, and X. Wang. *J. Chem. Soc., Dalton Trans.*, 0:517–518, 1999.

[77] C. Y. Yeh, C. H. Chou, K. C. Pan, C. C. Wang, G. H. Lee, Y. O. Su, and S. M. Peng. *J. Chem. Soc., Dalton Trans.*, 0:2670, 2002.

[78] C. Yin, G. C. Huang, C. K. Kuo, M. D. Fu, H. C. Lu, J. H. Ke, K. N. Shih, Y. L. Huang, G. H. Lee, C. Y. Yeh, C. h. Chen, and S. M. Peng. *J. Am. Chem. Soc.*, 130:10090–10092, 2008.

[79] S. Y. Lai, T. W. Lin, Y. H. Chen, C. C. Wang, G. H. Lee, M. H. Yang, M. K. Leung, and S. M. Peng. *J. Am. Chem. Soc.*, 121:250–251, 1999.

[80] Y. H. Chen, C. C. Lee, C. C. Wang, G. H. Lee, S. Y. Lai, F. Y. Li, C. Y. Mou, and S. M. Peng. *Chem. Commun.*, 0:1667–1668, 1999.

[81] S. M. Peng, C. C. Wang, Y. L. Jang, Y. H. Chen, F. Y. Li, C. Y. Mou, and M. K. Leung. *J. Magn. Magn. Mater.*, 209:80–83, 2000.

[82] R. H. Ismayilov, W. Z. Wang, R. R. Wang, C. Y. Yeh, G. H. Lee, and S. M. Peng. *Chem. Commun.*, 0:1121–1123, 2007.

[83] R. Clerac, F. A. Cotton, K. R. Dunbar, C. A. Murillo, I. Pascual, and X. Wang. *Inorg. Chem.*, 38:2655–2657, 1999.

[84] M. M. Rohmer and M. Bénard. *J. Am. Chem. Soc.*, 120:9372–9373, 1998.

[85] D. A. Pantazis and J. E. McGrady. *J. Am. Chem. Soc.*, 128:4128–4135, 2006.

[86] P. Kiehl, M. M. Rohmer, and M. Bénard. *Inorg. Chem.*, 43:3151–3158, 2004.

[87] C. K. Kou, I. P. C. Liu, C. Y. Yeh, C. H. Chou, T. B. Tsao, G. H. Lee, and S. M. Peng. *Chem. Eur. J.*, 13:1442–1451, 2007.

[88] S. H. Lai, C. J. Hsiao, J. W. Ling, W. Z. Wang, S. M. Peng, and I. C. Chen. *Chem. Phys. Lett.*, 456:181–185, 2008.

[89] C. J. Hsiao, S. H. Lai, I. C. Chen, W. Z. Wang, and S. M. Peng. *J. Phys. Chem. A*, 112:13528–13534, 2008.

[90] N. Benbellat, M. M. Rohmer, and M. Bénard. *Chem. Commun.*, 0:2368–2369, 2001.

[91] M. M. Rohmer, I. P. C. Liu, J. C. Lin, M. J. Chiu, G. S. Lee, M. Bénard, X. López, and S. M. Peng. *Angew. Chem. Int. Ed.*, 46:3533–3536, 2007.

[92] I. P. C. Liu, G. H. Lee, S. M. Peng, M. Bénard, and M. M. Rohmer. *Inorg. Chem.*, 46:9602–9608, 2007.

[93] G. C. Huang, M. Bénard, M. M. Rohmer, L. A. Li, M. J. Chiu, C. Y. Yeh, G. H. Lee, and S. M. Peng. *Eur. J. Inorg. Chem.*, 0:1767–1777, 2008.

[94] I. P. C. Liu, C. H. Chen, C. F. Chen, G. H. Lee, and S. M. Peng. *Chem. Commun.*, 0:577, 2009.

[95] M. Nippe and J. F. Berry. *J. Am. Chem. Soc.*, 129:12684–12685, 2007.

[96] M. Nippe, E. Victor, and J. F. Berry. *Eur. J. Inorg. Chem.*, 0:5569–5572, 2008.

[97] M. Nippe, G. H. Timmer, and J. F. Berry. *Chem. Commun.*, 0:4357–4359, 2009.

[98] M. Nippe, J. Wang, E. Bill, H. Hope, N. S. Dalal, and J. F. Berry. *J. Am. Chem. Soc.*, 132:14261–14272, 2010.

[99] M. Nippe, E. Bill, and J. F. Berry. *Inorg. Chem.*, 50:7650–7661, 2011.

[100] M. C. Cheng, C. L. Mai, C. Y. Yeh, G. H. Lee, and S. M. Peng. *Chem. Commun.*, 49:7938–7940, 2013.

[101] P. O. Löwdin. *Phys. Rev.*, 97:1509–1520, 1955.

[102] D. K. W. Mok, R. Neumann, and N. C. Handy. *J. Phys. Chem.*, 100:6225–6230, 1996.

[103] J. W. Hollett and P. M. W. Gill. *J. Chem. Phys.*, 134:114111–114115, 2011.

[104] N. C. Handy and A. J. Cohen. *Mol. Phys.*, 99:403–412, 2001.

[105] W. Kohn and L. J. Sham. *Phys. Rev.*, 140:A1133–A1138, 1965.

[106] A. J. Cohen, P. Mori-Sachez, and W. Yang. *Science*, 321:792–794, 2008.

[107] J. N. Harvey. *Annu. Rep. Prog. Chem., Sect. C: Phys. Chem.*, 102:203–226, 2006.

[108] N. E. Schultz, Y. Zhao, and D. G. Truhlar. *J. Phys. Chem. A*, 109:11127–11143, 2005.

[109] C. Rong, S. Lian, D. Yin, B. Shen, A. Zhong, L. Bartolotti, and S. Liu. *J. Phys. Chem. A*, 125:174102–174107, 2006.

[110] C. Rong, S. Lian, D. Yin, A. Zhong, R. Zhang, and S. Liu. *Chem. Phys. Lett.*, 434:149–154, 2007.

[111] B. O. Roos, P. R. Taylor, and P. E. M. Siegbahn. *Chem. Phys.*, 48:157–173, 1980.

[112] K. Andersson, P. A. Malmqvist, B. O. Roos, A. J. Sadlej, and K. Wolinski. *J. Phys. Chem.*, 94:5483–5488, 1990.

[113] J. Olsen, B. O. Roos, P. Jϕrgensen, and H. J. A. Jensen. *J. Chem. Phys.*, 89: 2185–2192, 1988.

[114] D. Ma, G. Li Manni, and L. Gagliardi. *J. Chem. Phys.*, 135:044128–044139, 2011.

[115] B. O. Roos, A. C. Borin, and L. Gagliared. *Angew. Chem. Int. Edn.*, 46:1469–1472, 2007.

[116] M. Brynda, L. Gagliardi, and B. O.Roos. *Chem. Phys. Lett.*, 471:1–10, 2009.

[117] K. Saito, Y. Nakao, H. Sato, , and S. Sakaki. *J. Phys. Chem. A*, 110:9710–9717, 2006.

[118] J. P. Blaudeau, R. B. Ross, R. M. Pitzer, P. Mougenot, and M. Benard. *J. Phys. Chem.*, 98:71237127, 1994.

[119] F. Poineau, L. Gagliardi, P. M. Forster, A. P. Sattelberger, and K. K. R. Czerwinski. *Dalton Trans.*, 0:5954–5959, 2009.

[120] Y. Y. Ohnishi, T. Matsunaga, Y. Nakao, H. Sato, and S. Sakaki. *J. Am. Chem. Soc.*, 127:4021–4032, 2005.

[121] M. M. Goodgame and W. A. Goddard. *Am. Chem. Soc.*, 85:215–217, 1981.

[122] E. A. Boudreaux and E. Baxter. *Inter. J. Quan. Chem.*, 85:509–513, 2001.

[123] E. A. Boudreaux and E. Baxter. *Inter. J. Quan. Chem.*, 100:1170–1178, 2004.

[124] E. A. Boudreaux and E. Baxter. *Inter. J. Quan. Chem.*, 102:866–868, 2005.

[125] E. J. Thomas, S. J. Murray, C. J. O'Connor, and P. Politzer. *J. Mol. Struct. (THEOCHEM)*, 487:177, 1999.

[126] V. E. Bondybey and J. H. English. *Chem. Phys. Lett.*, 94:443–447, 1983.

[127] B. O. Roos. *Collect. Czech. Chem. Commun.*, 68:265–274, 2003.

[128] G. Frenking and R. Tonner. *Nature*, 446:276–277, 2007.

[129] G. L. Gutsev and C. W. Bauschlicher. *J. Phys. Chem. A*, 107:4755–4767, 2003.

[130] S. M. Casey and D. G. Leopold. *J. Phys. Chem.*, 97:816–830, 1993.

[131] C. W. Bauschlicher and H. Partridge. *Chem. Phys. Lett.*, 231:277–282, 1994.

[132] M. Brynda, L. Gagliardi, P. O. Widmark, P. P. Power, and B. O. Roos. *Angew. Chem. Int. Edn.*, 45:3804–3807, 2006.

[133] G. La Macchia, V. Veryazov, B. O. Roos, and L. Gagliardi. *Inorg. Chem.*, 47: 11455–11457, 2008.

[134] G. L. Manni, A. L. Dzubak, A. Mulla, D. W. Brogden, J. F. Berry, and L. Gagliardi. *Chem. Eur. J.*, 18:17371749, 2012.

[135] I. G. Powers and C. Uyeda. *ACS Catal.*, 7:936–958, 2017.

[136] C. M. Farley and C. Uyeda. *In Press*, 2019.

[137] J. F. Berry. *Inorg. Chem.*, 56:7577–7581, 2017.

[138] S. Rej, H. Tsurugi, and K. Mashima. *Coor. Chem. Rev.*, 355:223–239, 2018.

[139] C. M. Thomas. *Comments Inorg. Chem.*, 32:14–38, 2011.

[140] P. Buchwalter, J. Rose, and P. Braunstein. *Chem. Rev.*, 115:28–126, 2015.

[141] N. P. Mankad. *Non-Noble Metal Catalysis: Molecular Approaches and Reactions*. R. J. M. Klen Gebbink, and M. -E. Moret (Ed.), Wiley-VCH, 2019.

[142] E. Nakamura, N. Yoshikai, and M. Yamanaka. *J. Am. Chem. Soc.*, 124:7181–7192, 2002.

[143] P. L. Pauson and I. U. Khand. *Ann. N. Y. Acad. Sci.*, 295:2–14, 1977.

[144] P. Magnus and L. M. Principe. *Tetrahedron Lett.*, 26:4851–4854, 1985.

[145] R. Paulissen, H. Reimlinger, E. Hayez, A. Hubert, and P. Teyssie. *Tetrahedron Lett.*, 14:2233–2236, 1973.

[146] A. Demonceau, A. F. Noels, A. J. Hubert, and P. Teyssie. *J. Chem. Soc., Chem. Commun.*, 0:688–689, 1981.

[147] H. M. L. Davies and J. R. Manning. *Nature*, 451:417–424, 2008.

[148] A. Ford, H. Miel, A. Ring, C. N. Slattery, A. R. Maguire, and M. A. McKervey. *Chem. Rev.*, 115:9981–10080, 2015.

[149] J. F. Berry. *Dalton Trans.*, 41:700–713, 2012.

[150] K. P. Kornecki, J. F. Briones, V. Boyarskikh, F. Fullilove, J. Autschbach, K. E. Schrote, K. M. Lancaster, H. M. L. Davies, and J. F. Berry. *Science*, 342: 351–354, 2013.

[151] C. Werle, R. Goddard, P. Philipps, C. Fare, and A. Fürstner. *J. Am. Chem. Soc.*, 138:3797–3805, 2016.

[152] R. H. Summerville and R. Hoffman. *J. Am. Chem. Soc.*, 101:3821–3831, 1979.

[153] B. E. Bursten, F. A. Cotton, and A. Fang. *Inorg. Chem.*, 22:2127–2133, 1983.

[154] R. Stranger, T. Lovell, and J. E. McGrady. *Polyhedron*, 21:1969–1977, 2002.

[155] R. Stranger, S. A. Macgregor, T. Lovell, J. E. McGrady, and G. A. Heath. *J. Chem. Soc., Dalton Trans.*, 0:4485, 1996.

[156] R. Stranger and J. E. McGrady. *Abs. Am. Chem. Soc.*, 220:U492–U492, 2000.

[157] R. Stranger, J. E. McGrady, and T. Lovell. *Abs. Am. Chem. Soc.*, 37:6795–6806, 1998.

[158] R. Stranger and S. Petrie. *J. Chem. Soc., Dalton Trans.*, 0:3630–3639, 2002.

[159] R. Stranger, A. Turner, and D. D. Christopher. *Inorg. Chem.*, 40:4093–4100, 2001.

[160] J. E. McGrady, R. Stranger, and T. Lovell. *J. Phys. Chem. A*, 101:6265–6272, 1997.

[161] R. Saillant and R. Wentworth. *J. Am. Chem. Soc.*, 91:2174–2175, 1969.

[162] V. Kolesnichenko, D. Swenson, and L. Messerle. *Chem. Commun.*, 0:2137–2138, 1998.

[163] G. A. Heath, J. E. McGrady, R. G. Raptis, and A. C. Willis. *Inorg. Chem.*, 35: 6838–6843, 1996.

[164] E. Schrödinger. *Annalen der Physik*, 384:361–376, 1926.

[165] W. Koch and M. C. Holthausen. *A chemist's guide to density functional theory.* Wiley-VCH, Weinheim, 2nd, 2001.

[166] A. Szabo and N. S. Ostlund. *Modern quantum chemistry: introduction to advanced electronic structure theory.* Dover, Mineola, 1996.

[167] V. Fock. *Z. Phys.*, 61:126–148, 1930.

[168] V. Fock. *Z. Phys.*, 62:795–805, 1930.

[169] J. C. Slater. *Phys. Rev.*, 35:210–211, 1930.

[170] L. Pauling. *Chem. Rev.*, 5:173–213, 1928.

[171] J. E. Lennard-Jones. *Trans. Faraday Soc.*, 25:668–686, 1929.

[172] C. C. J. Roothaan. *Rev. Mod. Phys.*, 23:69–89, 1951.

[173] P. O. Löwdin. *Adv. Chem. Phys.*, 2:207, 1959.

[174] D. K. W. Mok, R. Neumann, and N. C. Handy. *J. Phys. Chem.*, 100:6225–6230, 1996.

[175] J. W. Hollett and P. M. W. Gill. *J. Chem. Phys.*, 134:114111–114115, 2011.

[176] N. C. Handy and A. J. Cohen. *Molecular Physics*, 99:403–412, 2001.

[177] I. N. Levine. *Quantum chemistry*. Pearson Education, 7th, 2014.

[178] P. Hohenberg and W. Kohn. *Phys. Rev.*, 136:B864–B871, 1964.

[179] S. J. Vosko, L. Wilk, and M. Nusair. *Can. J. Chem.*, 58:1200–1211, 1980.

[180] A. D. Becke. *Phys. Rev. A*, 38:3098–3100, 1988.

[181] J. P. Perdew. *Phys. Rev. B*, 33:8822–8824, 1986.

[182] J. P. Perdew and Y. Wang. *Phys. Rev. B*, 45:13244–13249, 1992.

[183] C. Lee, W. Yang, and R. G. Parr. *Phys. Rev. B*, 37:785–789, 1988.

[184] A. D. Becke. *J. Chem. Phys.*, 104:1040, 1996.

[185] A. D. Becke. *J. Chem. Phys.*, 98:5648–5652, 1993.

[186] P. J. Stevens, J. F. Devlin, C. F. Chabalowski, and M. J. Frisch. *J. Phys. Chem.*, 98:11623–11627, 1994.

[187] S. Grimme. *J. Comput. Chem.*, 25:1463–1473, 2004.

[188] W. J. Hehre, R. F. Stewart, and J. A. Pople. *J. Chem. Phys.*, 51:2657–2664, 1969.

[189] W. J. Hehre, R. Ditchfield, and J. A. Pople. *J. Chem. Phys.*, 56:2257–2261, 1972.

[190] F. Bloch. *Z. Phys.*, 52:555–600, 1928.

[191] R. Dronskowski. *Computational Chemistry of Solid State Materials*. WILEY-VCH Verlag GmbH & Co. KGaA, 2005.

[192] H. Hellmann. *J. Chem. Phys.*, 3:61–61, 1935.

[193] H. Hellmann. *Acta Physicochim. URSS*, 1:913, 1934.

[194] H. Hellmann. *ibid.*, 4:225, 1936.

[195] H. J. Kulik, N. Seelam, B. D. Mar, and T. J. Martinez. *J. Phys. Chem. A*, 120: 5939–5949, 2016.

[196] V. I. Anisimov, J. Zaanen, and O. K. Andersen. *Phys. Rev. B*, 44:943–954, 1991.

[197] A. I. Liechtenstein, V. I. Anisimov, and J. Zaanen. *Phys. Rev. B*, 52:R5467–R5470, 1995.

[198] V. I. Anisimov, F. Aryasetiawan, and A. I. Lichtenstein. *J. Phys.: Condens. Matter*, 9:767–808, 1997.

[199] A. Bino and F. A. Cotton. *J. Am. Chem. Soc.*, 102:608–611, 1980.

[200] J. C. Fettinger, J. C. Gordon, S. P. Mattamana, C. J. O'Connor, R. Poli, and G. Salem. *Inorg. Chem.*, 35:7404–7412, 1996.

[201] L. Chen and F. A. Cotton. *Polyhedron*, 17:3727–3734, 1998.

[202] M. Schroeder, S. Hartwig, K. W. Krämer, S. Decurtins, and H. Hillebrecht. *Inorg. Chem.*, 51:8385–8393, 2012.

[203] J. W. Hewage, G. Cavigliasso, and R. Stranger. *Inorg. Chem.*, 54:10632–10641, 2015.

[204] F. A. Cotton, M. Matusz, and R. C. Torralba. *Inorg. Chem.*, 28:1516–1520, 1989.

[205] F. A. Cotton and R. C. Torralba. *Inorg. Chem.*, 30:3293–3304, 1991.

[206] F. A. Cotton and R. C. Torralba. *Inorg. Chem.*, 30:4386–4391, 1991.

[207] R. Goerissen, U. Kölle, and T. P. Spaniol. *Polyhedron*, 11:2317–2320, 1992.

[208] J. Darriet. *Rev. Chim. Min.*, 18:2732, 1981.

[209] A. J. McCaffery, M. D. Rowe, and D. A. Rice. *J. Chem. Soc., Dalton Trans.*, 0:1605–1610, 1973.

[210] J. B. Billones, Eva Marie A. Ratilla, and G. A. Heath. *Inorg. Chem. Comm.*, 14:17881793, 2011.

[211] C. K. Jϕrgensen. *Acta Chem. Scand.*, 10:500–517, 1956.

[212] A. J. McCaffery, P. N. Schatz, and T. E. Lester. *J. Chem. Phys.*, 50:379–385, 1969.

[213] G. te Velde, F. M. Bickelhaupt, E. J. Baerends, C. Fonseca Guerra, S. J. A. van Gisbergen, J. G. Snijders, and T. Ziegler. *J. Comput. Chem.*, 22:931–967, 2001.

[214] C. Fonseca Guerra, J. G. Snijders, G. te Velde, and E. J. Baerends. *Theor. Chem. Acc.*, 99:391–403, 1998.

[215] Evert Jan Baerends, Tom Ziegler, A. J. Atkins, Jochen Autschbach, Donald Bashford, O. Baseggio, A. Bérces, F. Matthias Bickelhaupt, C. Bo, P. M. Boerritger, Luigi Cavallo, C. Daul, D. P. Chong, D. V. Chulhai, L. Deng, R. M. Dickson, J. M. Dieterich, D. E. Ellis, M. van Faassen, A. Ghysels, A. Giammona, Stan J. A. van Gisbergen, A. Goez, A. W. Götz, S. Gusarov, F. E. Harris, P. van den Hoek, Z. Hu, Christoph R. Jacob, H. Jacobsen, L. Jensen, L. Joubert, J. W. Kaminski, G. van Kessel, C. König, F. Kootstra, A. Kovalenko, Mykhaylo Krykunov, Erik van Lenthe, D. A. McCormack, A. Michalak, M. Mitoraj, S. M. Morton, Johannes Neugebauer, V. P. Nicu, Louis Noodleman, V. P. Osinga, S. Patchkovskii, Michele Pavanello, C. A. Peeples, Pierre Herman Theodoor Philipsen, D. Post, Cory C. Pye, H. Ramanantoanina, P. Ramos, W. Ravenek, J. I. Rodríguez, P. Ros, R. Rüger, P. R. T. Schipper, D. Schlüns, H. van Schoot, G. Schreckenbach, J. S. Seldenthuis, Mike Seth, Jaap G. Snijders, Miquel Solà, Stener M., M. Swart, D. Swerhone, G. te Velde, V. Tognetti, P. Vernooijs, L. Versluis, Lucas Visscher, O. Visser, Fan Wang, T. A. Wesolowski, E. M. van Wezenbeek, G. Wiesenekker, S. K. Wolff, T. K. Woo, and A. L. Yakovlev. ADF2017, SCM, Theoretical Chemistry, Vrije Universiteit, Amsterdam, The Netherlands, https://www.scm.com.

[216] A. D. Becke. *Phys. Rev. A*, 38:3098–3100, 1988.

[217] C. Lee, W. Yang, and R. G. Parr. *Phys. Rev. B*, 37:785–789, 1988.

[218] A. D. Becke. *J. Chem. Phys.*, 98:5648–5652, 1993.

[219] P. J. Stephens, F. J. Devlin, C. F. Chabalowski, and M. J. Frisch. *J. Phys. Chem.*, 98:11623–11627, 1994.

[220] S. Grimme, S. Ehrlich, and L. Goerigk. *J. Comput. Chem.*, 32:1456–1465, 2011.

[221] L. Versluis and T. Ziegler. *J. Chem. Phys.*, 88:322–328, 1988.

[222] S. J. A. van Gisbergen, J. G. Snijders, and E. J. Baerends. *Comput. Phys. Commun.*, 118:119 – 138, 1999.

[223] S. Hirata and M. Head-Gordon. *Chem. Phys. Lett.*, 314:291 – 299, 1999.

[224] Y. Zhao and D. G. Truhlar. *J. Chem. Phys.*, 125:194101–194118, 2006.

[225] Y. Zhao and D. G. Truhlar. *Theor. Chem. Acc.*, 120:215–241, 2008.

[226] E. van Lenthe, P. E. S. Wormer, and A. van der Avoird. *J. Chem. Phys.*, 107: 2488–2498, 1997.

[227] E. van Lenthe, A. van der Avoird, and P. E. S. Wormer. *J. Chem. Phys.*, 108: 4783–4796, 1998.

[228] F. Aquilante, J. Autschbach, R. K. Carlson, L. F. Chibotaru, M. G. Delcey, L. De Vico, I. Fdez. Galvn, N. Ferr, L. M. Frutos, L. Gagliardi, M. Garavelli, A. Giussani, C. E. Hoyer, G. Li Manni, H. Lischka, D. Ma, P. Å Malmqvist, T. Mller, A. Nenov, M. Olivucci, T. B. Pedersen, D. Peng, F. Plasser, B. Pritchard, M. Reiher, I. Rivalta, I. Schapiro, J. Segarra-Mart, M. Stenrup, D. G. Truhlar, L. Ungur, A. Valentini, S. Vancoillie, V. Veryazov, V. P. Vysotskiy, O. Weingart, F. Zapata, and R. Lindh. *J. Comput. Chem.*, 37:506–541, 2016.

[229] B. O. Roos, V. Veryazov, and P-O. Widmark. *Theor. Chem. Acc.*, 111:345–351, 2004.

[230] F. Aquilante, P. Å. Malmqvist, T. B. Pedersen, A. Ghosh, and B. O. Roos. *J. Chem. Theory Comput.*, 4:694–702, 2008.

[231] N. R. Perkins. *The Synthesis, Electrochemistry and Spectroscopy of Face-*

Sharing Polynuclear Complexes. PhD thesis, The Australian National University, 2002.

[232] V. Arcisauskaite, M. Spivak, and J. E. McGrady. *Inorg. Chim. Acta*, 424:293–299, 2015.

[233] G. A. Heath, K. A. Moock, D. W. A. Sharp, and L. J. Yellowlees. *J. Chem. Soc. Chem. Commun.*, 0:1503–1505, 1985.

[234] B. D. Yeomans, D. G. Humphrey, and G. A. Heath. *J. Chem. Soc. Dalton Trans.*, 0:4153–4166, 1997.

[235] F. Barriere and W. Geiger. *J. Am. Chem. Soc.*, 128:3980–3989, 2006.

[236] G. A. Heath and J. E. McGrady. *J. Chem. Soc. Dalton Trans.*, 0:3759–3767, 1994.

[237] M. H. L. Pryce. *Proc. Phys. Soc. A*, 63:25–29, 1950.

[238] J. S. Griffith. *The Theory of Transition Metal Ions*. Cambridge University Press, Cambridge, 1961.

[239] K. A. Schroeder. *J. Chem. Phys.*, 37:2553–2559, 1962.

[240] B. D. Yeomans, D. G. Humphrey, and G. A. Heath. *J. Chem. Soc., Dalton Trans.*, 0:4153–4166, 1997.

[241] B. J. Kennedy, G. A. Heath, and T. J. Khoo. *Inorganica Chimica Acta*, 190: 265–269, 1991.

[242] G. A. Heath and J. E. McGrady. *J. Chem. Soc., Dalton Trans.*, 0:3759–3767, 1994.

[243] G. Cavigliasso and R. Stranger. *Inorg. Chem.*, 44:5081–5091, 2005.

[244] B. D. Yeomans, D. G. Humphrey, and G. A. Heath. *J. Chem. Soc., Dalton Trans.*, 0:4153–4166, 1997.

[245] R. S. Armstrong, W. A. Horsfield, and K. W. Nugent. *Inorg. Chem.*, 29:4551–4556, 1990.

[246] N. S. Hush, J. K.Beattie, and V. M. Ellis. *Inorg. Chem.*, 23:3339–3342, 1984.

[247] U. Kölle, J. Kossakowski, N. Klaff, L. Wesemann, U. Englert, and G. E. Herberich. *Angew. Chem.*, 103:732–733, 1991.

[248] U. Kölle, J. Kossakowski, N. Klaff, L. Wesemann, U. Englert, and G. E. Herberich. *Angew. Chem. Int. Ed. Engl.*, 30:690–691, 1991.

[249] U. Koelle, H. Lueken, K. Handrick, H. Schilder, J. K. Burdett, and S. Balleza. *Inorg. Chem.*, 34:6273–6278, 1995.

[250] Y. Jean, A. Lledos, J. K. Burdett, and R. Hoffmann. *J. Am. Chem. Soc.*, 110: 4506–4516, 1988.

[251] W. D. Stohrer and R. Hoffmann. *J. Am. Chem. Soc.*, 94:1661–1668, 1972.

[252] J. Chatt, Ljubica Manojlovic-Muir, and K. W. Muir. *J. Chem. Soc. Chem. Commun.*, 0:655–656, 1971.

[253] J. Song and M. B. Hall. *Inorg. Chem.*, 30:4433–4437, 1991.

[254] K. Yoon, G. Parkin, and A. L. Rheingold. *J. Am. Chem. Soc.*, 113:1437–1438, 1991.

[255] K. Yoon, G. Parkin, and A. L. Rheingold. *J. Am. Chem. Soc.*, 114:2210–2218, 1992.

[256] J. E. McGrady. *Angew. Chem. Int. Ed.*, 39:3077–3079, 2000.

[257] G. Kresse and J. Furthmüller. *Phys. Rev. B*, 54:11169–11186, 1996.

[258] M. R. Churchill, S. A. Julis, and F. J. Rotella. *Inorg. Chem.*, 16:1137–1141, 1977.